Ore-Forming Processes of the Daqiao Epizonal Orogenic Gold Deposit, West Qinling Orogen, China: Constraints from Textures, Trace Elements and Sulfur Isotopes of Pyrite and Marcasite, and Raman Spectroscopy of Carbonaceous Material

Ya-Fei Wu, [1,2,3] Jian-Wei Li, [1,3†] Katy Evans, [2] Alan E. Koenig, [4] Zhan-Ke Li, [3] Hugh O'Brien, [5] Yann Lahaye, [5] Kirsten Rempel, [2] Si-Yu Hu, [6] Zhong-Ping Zhang, [7] and Jun-Peng Yu [8]

[1] State Key Laboratory of Geological Processes and Mineral Resources, China University of Geosciences, Wuhan 430074, China

[2] Department of Applied Geology, Curtin University, GPO Box U1987, Perth, WA 6845, Australia

[3] School of Earth Resources, China University of Geosciences, Wuhan 430074, China

[4] United States Geological Survey, Denver Federal Center, MS973, Box 25046, Denver, CO 80225, USA

[5] Geological Survey of Finland, 02150 Espoo, Finland

[6] CSIRO Mineral Resources, Australian Resources Research Centre, 26 Dick Perry Avenue, Kensington, Perth, WA 6151, Australia

[7] Geological Survey of Gansu Province, Lanzhou, China

[8] Fourth Institute of Geological and Mineral Exploration of Gansu Provincial Bureau of Geology and Mineral Resources, Jiuquan, China

†Corresponding author:

E-mail: jwli@cug.edu.cn

Phone: +86 27 67883653

Fax: +86 27 67885096

Abstract

The Daqiao gold deposit is hosted in organic-rich Triassic pumpellyite-actinolite facies metamorphosed turbidites in the West Qinling Orogen, central China. Gold mineralization is characterized by high-grade hydraulic breccias (B and C ores) that overprint an earlier tectonic breccia (A ore). A complex paragenesis is defined by four sulfide stages: S1 diagenetic pre-ore pyrite (py), S2 hydrothermal early-ore disseminated pyrite and marcasite (mc), S3 main-ore pyrite and marcasite aggregates, and S4 late-ore coarse-grained marcasite with minor pyrite and stibnite. However, multiple generations of pyrite and marcasite may develop within one individual stage. Ore-related hydrothermal alteration is dominated by intensive silicification, sulfidation, sericitization, and generally distal minor carbonatization.

Laser ablation-inductively coupled plasma-mass spectrometry (LA-ICP-MS) trace element analyses show that the stage S1 py1 from the shale interlayers within turbidites contains low gold contents (mean of 0.05 ppm) and other trace elements (Mn, Co, Ni, Cu, Mo, Bi, and Pb) indicating an anoxic to euxinic sedimentary environment. Stage S2 contributed only minimally to the gold endowment with relatively low gold in various sulfides including py2 (mean of 0.09 ppm), py3 (0.84 ppm) to py4 (0.70 ppm), along with mc1 (0.02 ppm) and mc2 (0.14 ppm). Most of the gold was deposited in stage S3, which formed rapidly crystallized, irregular (e.g., framboids, colloform and cyclic zonation) cement-hosted py5a (mean of 27.35 ppm), py5b (9.71 ppm), and mc3 (5.94 ppm) during repeated hydraulic fracturing. Other trace elements (e.g., Ag, As, Sb, Hg, Tl, and W) are also significantly enriched in the main-ore stage pyrite and marcasite. Little or no gold is detected in the S4 py6 and mc4.

Sulfur isotopes determined from in situ LA-MC-ICP-MS analyses of hydrothermal pyrite and marcasite from the Daqiao deposit vary significantly from -31.3 to +22.0‰ ($\delta^{34}S$ values), but fall mostly between -10 to +10‰, and provide important information on the source and evolution of sulfur and of the ore-forming fluids. The results show that S2 ore fluids (mean $\delta^{34}S_{sulfide}$ = -0.8 to +5.2‰) were most

likely derived from deep-seated Paleozoic carbonaceous sediments during regional metamorphism associated with orogenesis of the West Qinling Orogen. Main-ore S3 ore fluids (mean $\delta^{34}S_{sulfide}$ = -9.7 to -6.0‰) are relatively depleted in ^{34}S relative to those of S2, presumably due to fluid oxidation associated with hydraulic fracturing caused by the over pressurized fluids.

The textural, chemical, and isotopic data indicate two distinct gold-introducing episodes at Daqiao, forming sulfide disseminations during early-ore S2 and cement-hosted sulfide aggregates during main-ore S3. The S2 mineralization took place in a tectonic breccia beneath low-permeability shale seals that capped the flow of deep-seated metamorphic fluids, facilitating reaction with pre-existing carbonaceous material and the host turbidites to form sulfide disseminations and pervasive silicification. Raman spectroscopic analysis suggests that carbonaceous material in the ores is poorly crystallized, with low maturity, giving estimated temperatures of 283–355 °C that are much higher than that of the ore fluids (100–240 °C). This temperature difference indicates an in-situ sedimentary origin modified by the regional pumpellyite-actinolite facies metamorphism for the carbonaceous material in the host rocks, rather than a hydrothermal origin. In S3, continuous flux of hydrothermal fluids caused fluid overpressure and consequently hydraulic fracturing of the competent silicified rocks. Subsequent rapid fluid-pressure fluctuations led to phase separation and thus massive oxidation of ore fluids, which triggered fast precipitation of gold and other trace elements within the fine-grained irregular sulfides. Results presented here, in combination with geological evidences, suggest that the Daqiao gold deposit can be best classified as the shallow-crustal epizonal orogenic type, genetically associated with orogenic deformation and regional metamorphism of the West Qinling Orogen.

Introduction

The West Qinling Orogen (WQO) is located on the eastern margin of the Asian continent and formed during the continental collision between the North China Craton

(NCC) and the South China Block (SCB) (Mattauer et al., 1985), the latter being produced by amalgamation of the Yangtze Craton and the Cathaysia Block along the Jiangnan fold belt in the early Neoproterozoic (Zhao et al., 2011). Over the past decades, the WQO has become one of the most important and prospective gold provinces in China with a current gold endowment of over 2,000 t (Chen and Santosh, 2014; Liu et al., 2015). It contains more than 100 sediment-hosted gold deposits, including more than 10 world-class deposits (cf. Goldfarb et al., 2005) such as the Yangshan (>300 t Au), Baguamiao (>106 t Au; Liu et al., 2015), Zaozigou (142 t Au; Sui et al., 2017), and Daqiao (>105 t Au) gold deposits (Fig. 1A).

Gold mineralization in the WQO is mainly hosted in Early Paleozoic to Early Triassic sedimentary sequences and mostly formed during the Late Triassic to Middle Jurassic (Mao et al., 2002; Chen et al., 2004; Zeng et al., 2012), with a few deposits emplaced in the Early Cretaceous (Lu et al., 2006; Zeng et al., 2013). The regional Hezuo-Lintan-Liangdang Fault (HLLF) divides the mineralization into northern and southern belts (Fig. 1A), which display distinctive gold mineralization styles, alteration assemblages, and trace element patterns (e.g., Mao et al., 2002; Zhou et al., 2002). Gold deposits in the northern belt are mainly hosted by Devonian greenschist facies flysch rocks, and predominantly occur as quartz stockworks and veinlets along major ductile-brittle shear zones or their secondary structures (e.g., Baguamiao). They are considered to be orogenic gold deposits (Mao et al., 2002; Zhou et al., 2002; Chen et al., 2004; Goldfarb et al., 2014).

Gold deposits in the southern belt are mostly hosted by low-grade or unmetamorphosed Triassic turbidite sequences, with minor gold in the Early Cambrian and Devonian carbonaceous clastic rocks (Li and Peters, 1998). These deposits have been described and mined for decades, but there is no consensus on their genetic classification, sources of ore fluids and metals, or ore-forming processes (e.g. Zhang et al., 2001; Mao et al., 2002; Zhou et al., 2002; Chen et al., 2004; Chen and Santosh, 2014). In view of the disseminated, low-temperature alteration assemblages, the fine-grained nature of gold, general lack of visible gold, plus the Au-As-Hg-Sb-(Tl) elemental association, some researchers have proposed that they are analogues of Carlin-type gold deposits (namely Carlin-like; Kerrich et al., 2000; Zhang et al., 2001, 2009; Mao et al., 2002; Chen et al., 2004). However, other features, such as a lack of decarbonatization, a predominance of clastic hosts to gold mineralization, and the common presence of carbonic fluid inclusions are inconsistent with Carlin-like classifications; rather, they suggest similarities to orogenic gold deposits (Vielreicher et al., 2003; Goldfarb et al., 2014; Zhou et al., 2014; Yang et al., 2016; Yue et al., 2017).

Conventional bulk isotope analysis and fluid inclusion studies have also contributed to contrasting interpretations on the gold genesis of the southern belt. Some researchers have proposed that the ore-forming fluids are a mixture of a metamorphic or magmatic component with external meteoric water (Li et al., 2008; Yang, 2014; Zhou et al., 2014). However, other studies suggest that gold and other constituents in the fluids have multiple sources, ranging from the Triassic sedimentary sequences (Li et al., 2014; Yang, 2014), to the underlying Proterozoic basement rocks (Zhang et al., 2009), and to granitic dikes and related deep-seated magma chambers (Qi et al., 2003a, 2003b, 2006; Yang et al., 2016). The mechanisms by which the gold and ore fluids were extracted from the source rocks, are unclear and poorly understood. Given the complex textures of ore and gangue minerals in most gold deposits, the loosely constrained paragenesis of the minerals used for isotope analysis, and the evidence of long-lived fluid transport and extensive fluid-rock interaction, existing stable isotope data commonly provide ambiguous evidence for metal and fluid sources as well as ore genesis. The mechanism of gold mineralization is also controversial, with various models emphasizing fluid mixing (Zhou et al., 2014) or unmixing (Li et al., 2008; Yue et al., 2017) and fluid-rock interaction (Li et al., 2014; Yang, 2014). Carbonaceous material (CM) is common and abundant in the host rocks for gold mineralization and has close association with gold ores in some deposits (e.g., La'erma, Yangshan and Daqiao), but its role in gold deposition remains poorly understood (Li and Peters, 1998; Zhang et al., 2001; Qi et al., 2003a).

The Daqiao gold deposit is a newly-discovered, large-tonnage, and representative gold deposit in the southern belt (Fig. 1B). Gold mineralization at Daqiao is hosted by

Middle Triassic organic-rich slates and is characterized by very fine-grained ores, low-temperature alteration assemblages, predominance of invisible gold, and a geochemical association of Au-Ag-As-Sb-Tl (You and Zhang, 2009). Gold mineralization is closely associated with multistage silicification and brecciation. Several previous studies focused mostly on the geological features and fluid inclusions (You and Zhang, 2009; Liu et al., 2011; Xu et al., 2015), but there is no consensus on the genetic type of the deposit and genesis of the gold mineralization. The fluid inclusions trapped in coarse-grained quartz have final homogenization temperatures of 270–310 °C (Liu et al., 2011), significantly higher than the values deduced from the geothermal gradient at the estimated depth of gold deposition (100–240 °C at 1 km; Xu et al., 2015). This temperature contrast suggests that ore-forming fluids may have derived from a deep-seated, metamorphic or magmatic source. Unfortunately, this hypothesis has not yet been tested due to a lack of geochemical and isotopic data integrated with detailed textural characterization of the ore and gangue minerals.

In this paper, we present a detailed petrographic study of gold ores and alteration assemblages, with particular attention to the textural evolution of sulfide minerals. We then carry out compositional analysis of various sulfides using laser ablation inductively coupled plasma mass spectrometer (LA-ICP-MS) to reveal the occurrence, distribution, and evolution of gold and associated trace elements. Lastly, we conduct in situ sulfur isotope analysis of texturally complex sulfides to examine microscopic variations of sulfur isotopic compositions in the processes of gold mineralization. The results are used to provide insights into the source of sulfur and gold. When combined with Raman spectroscopic analysis of CM from gold ores, the textural, elemental, and isotopic data also allow us to explain the mechanisms of gold deposition and to propose a reasonable classification of ore deposit type.

Regional Geology

Tectonic setting

The roughly NWW-striking Triassic Qinling Orogen extends for 2,500 km across central China from the Dabie Mountains in the east to the Qilian and Kunlun Mountains in the west (Fig. 1A). It is separated from the North Qinling Terrain by the Paleozoic Shangdan suture zone to the north and from the Songpan-Ganze flysch basin and South China Block by the Triassic Mianlue suture zone to the south (Zhang et al., 2001; Chen et al., 2006; Dong et al., 2011, 2013). This orogenic belt records a complex, multistage orogenic history involving prolonged subduction and closure of the Shangdan and Mianlue oceans from Middle Paleozoic to Early Mesozoic (Meng and Zhang, 1999; Dong et al., 2011, 2013). The Paleozoic orogeny occurred roughly parallel to the Shangdan suture and has been interpreted as being related to Early Devonian northward subduction and closure of the Shangdan Ocean, and subsequent Middle Devonian to Early Triassic continental subduction beneath the North Qinling Terrain (Zhang et al., 2001; Dong et al., 2013). The Triassic Orogeny, which formed the Qinling Orogen, mainly resulted from northward subduction of the Mianlue Ocean and subsequent continental collision between the NCC and SCB (Zhang et al., 1995, 1996, 2001; Dong et al., 2011 and references therein). A scissor-like suturing from east to west is commonly accepted for the closure of the Mianlue Ocean and subsequent continental collision between the SCB and NCC, presumably due to the clockwise rotation of the SCB with respect to the NCC (Zhu et al., 1998; Gilder et al., 1999; Zhao et al., 1999; Chen et al., 2006).

The Qinling Orogen underwent post-orogenic intracontinental tectonism from the Middle Jurassic (Dong et al., 2011). During the Late Jurassic to Cretaceous, the orogen was tectonically overprinted by large-scale southward overthrusting along the Mianxian-Chengkou-Xiangguang Fault (MCXF), which has been suggested to be related to the southward intracontinental subduction of the NCC (Zhang et al., 2001; Dong et al., 2011, 2013). The Qinling Orogen has been broadly divided into the East and West Qinling Orogens (EQO and WQO) by the Baocheng railway (Zhang et al.,

1995) or by the Chengxian-Huixian-Fengxian Fault (CHFF), based on geochemical signatures of Triassic granitoid intrusions and basement rocks (Zeng et al., 2014; Fig. 1A).

Geology of the West Qinling Orogen

The WQO can be subdivided into northern and southern domains separated by the Hezuo-Lintan-Liangdang thrust fault (HLLF; Gansu Geological Survey, 2011) or Lixian-Shanyang fault (Fig. 1A; Mao et al., 2002). The northern domain is characterized by extensive exposures of Devonian flysch sequences that have been subjected to greenschist facies metamorphism (Mattauer et al., 1985; Mao et al., 2002). The southern domain is bounded by the Triassic Songpan-Ganzi basin to the southwest, and separated lengthwise by the Zhouqu-Chengxian-Huixian Fault (ZCHF; Fig. 1A). The northern section comprises an east-verging belt of low-grade or unmetamorphosed Triassic turbidites, as illustrated by well-preserved primary sedimentary structures and Bouma sequences (Meng et al., 2007). The southern section consists of a series of ESE-trending anticlines (e.g., Bailongjiang Anticline) involving Cambrian to Middle Triassic strata (Zeng et al. 2013). These strata have been strongly deformed during post-orogenic intracontinental tectonism (Zhou and Graham, 1996; Zeng et al. 2013), forming a number of regional south-verging arc-shaped, thin-skinned thrust nappe structures (Zhang et al., 2001).

In the WQO, Mesozoic granitoid intrusions are widespread, locally associated with minor dolerite, gabbro and diorite stocks or dikes and mafic microgranular enclaves in the granitoid intrusions (Zhang et al., 2009). Zircon U-Pb dating results have revealed that the intrusions are commonly younger in the east (200–220 Ma) than the west (240–250 Ma; Sun et al., 2002; Zeng et al., 2014; Dong and Santosh, 2016). This age pattern of magmatic rocks may record the westward, scissor-like closure of the Mianlue Ocean and subsequent continental collision (Zhu et al., 1998; Gilder et al., 1999).

Geology of the Daqiao Gold Deposit

The Daqiao gold deposit is structurally controlled by the

Zhouqu-Chengxioan-Huixian Fault (ZCHF; Gansu Geological Survey, 2011), and is hosted in the turbidite sequences of the Middle Triassic Huashiguan Formation that are in fault contact with Carboniferous limestone (Figs., 1B, 2A, 3). The turbidite sequences mainly consist of siltstone, siliceous, calcareous and pelitic slates, with lesser pyritic carbonaceous slates and thin to thick-bedded limestone (Fig. 2B).

Structurally, the Daqiao gold deposit is located in the northwestern flank of an inferred anticline (You and Zhang, 2009). The anticline consists of Carboniferous limestone in the core and Triassic clastic rocks in both limbs, with the northern limb mineralized in gold. There are a number of reverse faults in the deposit, which mostly strike northeast and, less commonly, nearly east-west or north-south (Fig. 2A). The Yaoshang-Shixia Fault (YSF), locally called F9, separates the Carboniferous limestones from the Triassic turbidites and is a secondary fault of the regional ZCHF (Fig. 2A). The YSF has been interpreted to be a conduit of the auriferous fluids that formed Daqiao and other gold deposits in the area (You and Zhang, 2009). Both the anticline and reverse faults are likely results of Mesozoic orogenic deformation (Dong et al., 2011; Dong and Santosh, 2016).

Magmatism at the Daqiao mine and surrounding areas is represented by a number of dikes of intermediate to silicic composition, which intrude the Carboniferous and Triassic sedimentary rocks (Figs. 1B, 2). In the Daqiao gold mine, the granodiorite dikes show close spatial relations to gold orebodies and strongly silicified zones (Figs. 2A, 3A). Individual dikes extend for several tens to a few hundred meters along northeast or northwest strike and are 2 to 10 m in thickness. The dikes are weakly deformed and have been subjected to variable degrees of silicification, sericitization, sulfidation, carbonatization, and occasionally weak gold mineralization. Recent LA-ICP-MS zircon U-Pb dating results indicate that the granodiorite dikes were emplaced between 215–212 Ma (Gansu Geological Survey, 2017).

The host rocks of most gold resources at Daqiao are siliciclastic breccias that are mainly localized between the Triassic slate and Carboniferous limestone units, as well as interlayered structures within the Triassic slates (Figs. 2B, 3, 4A). These breccias are locally termed tectonic breccias of the Huashiguan Formation (Gansu Geological

Survey, 2011). All the hydrothermally altered and mineralized tectonic breccias are developed along the NE-striking reverse faults (Fig. 2A), indicating that these breccias formed during the faulting and deformation. For instance, the F6-F8 faults, which strike NE and dip 55°–70° to SE, are the major structures in the deposit area, and host the largest gold ore body, I-1 (Fig. 2A). Other gold orebodies are cut by these faults indicating that the faults reactivated during and after gold mineralization (Gansu Geological Survey, 2011).

Mineralization and Alteration

Gold orebodies

The Daqiao gold deposit consists of more than 100 orebodies with a total proven reserve of 105 t Au in 2012 (Gansu Geological Survey, 2017). Continuous drilling in the last five years has revealed additional resources at depth and surrounding areas (Gansu Geological Survey, 2017). The deposit can be divided into the northern and southern zone separated by the Xihanshui River (Fig. 2A). Orebodies are largely controlled by a number of NE-trending reverse faults in the southern zone, but NW-striking faults are more important in the northern zone (Fig. 2A). Gold mineralization is hosted mainly in the highly competent and permeable Triassic silicified breccias and, less commonly, silicified slates (Figs. 2-4, 5C-H). Gold orebodies are mostly present at 50–120 m below the present surface, but the uppermost parts of some orebodies in the southern zone are exposed and intensively oxidized, forming supergene ores. The hypogene sulfide ores have an average grade of 3–4 g/t gold, but high grade ores up to 30 g/t are not uncommon in the extensively silicified fault gouge (Gansu Geological Survey, 2011). The supergene ores are generally 20–50 m thick and combined have 9 t gold at 7–9 g/t. The ores also contain 2–50 g/t Ag, locally with highest grade of 370 g/t. In most cases, Au and Ag display a positive correlation (You and Zhang, 2009). Production at Daqiao started in 2012, and ca. 5 t Au has been extracted from the supergene ores using the cyanide leaching with a recovery rate of gold at 70–80% (Gansu Geological Survey, 2011). Gold recovery from the hypogene ores remains in the test stage and production is expected to be launched in 2019. Based on milling and flotation of the past four years, ca. 70% of gold in the hypogene ores can be recovered.

The largest ore body, I-1, is about 2 km along strike, with an average thickness of 12 m and spans a maximum vertical extent of 525 m from 1127 to 1652 m above sea level (Fig. 3). Other important orebodies include I-3, I-4, II-7, II-19, and II-22 (Fig. 3), which are 60 to 300 m long, 2 to 30 m thick, and continuous for 40 to 355 m down dip (Gansu Geological Survey, 2011).

The orebodies are characterized by well-developed auriferous breccias. Using field relations, textures, and paragenetic relationships of ore minerals, three types of breccia ores have been identified: tectonic breccia A; hydraulic breccia B; and hydraulic breccia C (Figs. 4, 5). The best-mineralized areas are associated with hydraulic breccia B and C and host gold grades between 1 and 12 g/t. However, tectonic breccia A, with relatively low gold grades of <4 g/t, also hosts significant amounts of gold due to its large mass and volume. Breccia A roughly occurs along the contact zone of the Triassic and Carboniferous sedimentary rocks. These breccias consist of in-situ siltstone, slate and limestone clasts, which are cemented by fault gouge, hydrothermal microcrystalline quartz and very fine-grained sulfides (Fig. 4C). Breccia A was further brecciated and cemented by chalcedony and sulfides to form intensively silicified hydraulic breccia B (Figs. 4D, 5E-G). Breccia C resulted from repeated hydraulic fracturing of breccia B in proximity to the contact zone between the Triassic and Carboniferous strata, and the hydrothermal cements are dominated by calcite, sulfides, and minor chalcedony (Figs. 4B, D, 5D-G).

Ore mineralogy

Arsenian pyrite and marcasite are the predominant ore minerals of the hypogene ores, associated with minor to trace amounts of stibnite, chalcopyrite, sphalerite, galena, arsenopyrite, pyrrhotite, unidentified uranium oxides and PGE minerals. The gangue minerals consist of quartz, calcite, sericite, kaolinite, and CM, with accessory apatite, rutile and monazite. Gold mainly occurs as invisible gold in arsenian pyrite and marcasite. Free gold grains are abundant in the oxidized ores, ranging in size from 1 to 70 μm (You and Zhang, 2009). They occur as irregular, tabular or dendritic inclusions in limonite or as stringers filling fractures in quartz.

Sulfide minerals occur as disseminations or thin veinlets with a variety of cross cutting relationships and textures in the alteration zones. On the basis of the morphology, texture, and paragenesis, four stages of sulfides are recognized (Table 1). Layered or nodular pyrite aggregates attributed to the pre-ore stage (S1) occur in the black shale or carbonaceous layers within the Triassic turbidites (Fig. 5A, B). The early-ore stage (S2) mainly consists of fine-grained euhedral pyrite cubes, pyritohedrons, columnar marcasite and irregular sulfide aggregates with abundant inclusions of apatite, chalcopyrite, galena, CM, and silicates. The S2 sulfides are mainly hosted by breccia A (Figs. 4C, 6) and, less commonly, by minor quartz-pyrite veinlets typically parallel to the bedding of altered calcareous slate (Fig. 5C). The main-ore stage (S3) sulfides are dominated by fine-grained pyrite aggregates that occur in milky quartz in breccia B (Figs. 5E-G, 7A, B), and medium- to coarse-grained colloform pyrite or marcasite veinlets in breccia C (Figs. 5D, F, G, 7C). The late-ore stage (S4) is characterized by widespread coarse-grained carbonate and marcasite veinlets in the deformed pelitic slates close to the orebodies (Fig. 5H). Marcasite, characterized by a strong anisotropy with yellowish-brown to grayish-blue polarization colors, was distinguished from the surrounding pyrite under optical microscopy (Fig. 7D). Additional EBSD analysis has been conducted on sulfides to better show the presence of marcasite and its textural information (Fig. 7E). On the basis of detailed microscopic, SEM and EBSD observations, marcasite accounts for approximately 0%, 20%–35%, 15%–25% and 70%–85% of total sulfides in the pre-, early-, main- and late-ore stage, respectively.

The CM is widespread in the silicified black tectonic breccia ores at Daqiao. It is commonly present as sparse to dense disseminations of 10–200 μm across (Fig. 6). Some CM is enveloped by S2 irregular porous pyrite aggregates with irregular or curvilinear interfaces between them (Fig. 6A, B). Fine-grained CM also occur as intergrowths with aggregates of porous pyrite and euhedral marcasite (Fig. 6C, D). No

CM veinlets are observed in the hydrothermal cements of auriferous breccias B and C.

Hydrothermal alteration

Hydrothermal alteration at Daqiao mainly consists of silicification, sulfidation, sericitization, and carbonatization with no clear zonation. Silicification, the most pervasive alteration type, is multistage (Fig. 7A, B), and is controlled by the porosity and permeability of the immediate host rocks. It mainly occurs in the calcareous siltstone, siliceous slates and complex breccias that are characterized by high permeability. The early dispersive and infiltrative silicification formed narrow selvages (a few μm) of quartz in the granodiorite dikes, as well as quartz-sulfide veinlets (Fig. 5C) and more widespread microcrystalline quartz in the altered slate via replacement of preexisting wall-rock plagioclase and carbonate. Silicification is also broadly contemporaneous with formation of disseminated S2 sulfides in breccia A (Fig. 7F). The second stage of silicification mainly occurs as microcrystalline quartz with a milky to chalcedonic appearance, and precipitated coevally with irregular aggregates of fine-grained pyrite in the cements of breccia B (Figs. 5E, 7B). Late, relatively weak silicification consists of minor amounts of chalcedony intergrown with calcite and pyrite or marcasite aggregates, and is associated with the second hydraulic fracturing event recorded by breccia C (Fig. 7B, C).

Sulfidation is associated with multistage silicification as mentioned above, mainly as four stages (pre-, early-, main-, and late-ore) of pyrite and marcasite associated with minor stibnite and arsenopyrite in various breccias. There are sulfide veinlets (Fig. 5C, H) in the black silicified silty slate, fine-grained disseminated or irregular sulfide aggregates in the breccia A (Figs. 6, 7F), as well as in the cements of breccia B (Fig. 5E) and breccia C (Figs. 5F, G, 7B, C). Sericite is widespread as an alteration product of plagioclase and K-feldspar. It is commonly intergrown with disseminated sulfides, occurring both in the altered granodiorite dikes and breccia-type ores (Fig. 7F). Carbonate minerals developed most widely in the main and late-ore stage, mainly occurring as cements of breccia C (Figs. 5D-G, 7B, C) or veins of coarsely crystalline calcite associated with marcasite in the weakly silicified slates (Fig. 5H).

Samples and Analytical Techniques

LA-ICP-MS multi-element analysis and imaging of sulfides

A total of 54 samples of unweathered wall-rocks and gold ores of different hydrothermal stages were chosen for in-situ compositional and isotopic analyses. These samples were collected from open pits, boreholes (ZK4713, depth 1060m; ZK54004, 380m; ZK10803, 570m; ZK17202, 568m; ZK 18801, 650m; ZK58003, 363m), or underground tunnels. Polished thin sections and section blocks containing sufficient amounts of sulfide minerals and their host rocks were characterized by optical microscopy, electron backscatter diffraction (EBSD), and electron microprobe analysis (EMPA).

EBSD data were determined using a TESCAN MIRA field emission gun SEM equipped with an Oxford EBSD at Curtin University. The MIRA was operated at 20 kV and 15 nA. EBSD data were collected using an Oxford Nordlys system and optimized at 25 ms per frame, and data were acquired using Oxford Instruments AZtec software and post-processed with Channel 5.12 software.

The EMPA was performed using a JEOL JXA-8230 electron probe at the Center for Material Research and Analysis, Wuhan University of Technology, China. The operating conditions consisted of an acceleration voltage of 25 kV, a probe current of 20 nA, and a beam diameter of 1–5 μm. Major elements in pyrite and marcasite were analyzed by EMPA to be used for characterization and calibration information of the LA-ICP-MS analyses described below.

Trace element concentrations were determined using LA-ICP-MS. Samples showing zoning were mapped with this technique to define sulfide growth zones. The analytical instrumentation employed in this study was a Photon Machines Analyte G2 LA system (193 nm, 4 ns excimer) attached to a PerkinElmer DRC-e ICP-MS, housed at the U.S. Geological Survey, Denver Federal Center, USA. Spot analyses were used for individual analysis of various chemical zones known from EMPA data. Line scans were used for trace element maps. Spot ablation was carried out using a 30 micrometer spot size at 5 J/cm^2 and using 7 Hz, with a 35 s baseline and 40–50 s of ablation. Line scans were carried out using a 22 micron square spot with 12 Hz and a scan speed of 4 micrometers/s. Ablated materials were transported via a He carrier gas to a modified glass mixing bulb where the He plus the sample aerosol were mixed coaxially with Ar prior to the ICP torch. Concentration and detection limit calculations were conducted using the protocol of Longerich et al. (1996). Signals of both pyrite and marcasite were calibrated using USGS MASS-1 sulfide reference material and iron (^{57}Fe) was used as the internal standard (Wilson et al., 2002; Franchini et al., 2015). The reference material (MASS-1) was analyzed 5–10 times at the beginning of the analytical session and monitored throughout the session for drift. Signals were screened visually for heterogeneities such as micro-inclusions or zoning. The results are summarized in Table 2.

Concentrations for each time slice (75–250 seconds) of the line scans (300–1000 μm) used for the maps were calculated using a similar procedure to the spots. Concentration at each time slice (0.8 s) was stacked to form an x-y-concentration grid and displayed as false color images using a kriging algorithim. Methods for mapping in pyrite are similar to methods previously reported for fossil bones and phosphate materials (Koenig et al., 2009; Emsbo et al., 2015).

LA-MC-ICP-MS sulfur isotope analysis

Polished thin sections and section blocks analyzed for LA-ICP-MS trace element spot analysis were re-polished and used for in-situ sulfur isotope analysis. In situ S isotope analyses of pyrite and marcasite were performed using a Nu Plasma HR multicollector ICP-MS together with a Photon Machine Analyte G2 laser system, housed at the Geological Survey of Finland (GSF), Espoo, Finland. Samples were ablated in He gas (gas flows = 0.4 and 0.1 l/min) within a HelEx ablation cell (Müller et al., 2009). During the ablation the data were collected in static mode (^{32}S, ^{34}S).

Pyrite and marcasite were both ablated at a spot size of 30 micrometers, using a fluence of 0.83 J/cm^2 and 5 Hz. The total S signal obtained for pyrite was typically 1.0–1.2 V. Under these conditions, after a 20 s baseline, 50–60 s of ablation is needed to obtain an internal precision of $^{34}S/^{32}S \leq \pm 0.000005$ (1 SE). Three pyrite standards were used for external standard bracketing (PPP-1) (Gilbert et al., 2014) and quality control (Pyrite1 and Pyrite2 from GSF) of analyses (Wong et al., 2017). The measurement of the in-house Pyrite2 standard during the course of this study yielded the value of $\delta^{34}S_{CDT}$ (‰) of -0.2 ± 0.5 (1σ, n = 70), which within error is consistent with the reported value of -0.4 ± 0.5 (1σ) measured by gas mass spectrometry (Wong et al., 2017). These pyrite standards were appropriate for calibration of marcasite and even arsenopyrite sulfur isotope analyses (Prendergast et al., 2005), and there was no additional matrix fractionation correction applied for the marcasite herein.

Analyses of pyrite and marcasite zonation patterns were performed using line raster at 1 micrometer per second and the same laser parameters as above. Analyses were integrated every 2.5 s in order to get an internal precision, on average, of $^{34}S/^{32}S \leq \pm 0.00003$ (1 SE). The PPP-1 pyrite standard was run before and after each line for isotope fractionation correction. The results are given in Table 3.

Raman spectroscopic analysis of carbonaceous materials

Two intensively silicified disseminated ores samples collected underground were used for the CM study. Polished thin sections were examined under reflected and transmitted light to identify the shape, size, and distribution of the CM and its textural relationship with sulfides. Quantitative Raman spectra analysis was conducted on the CM by a Horiba® LabRAM HR Evolution and a Synapse Visible detector at the Key Laboratory of Mineral Resources, Institute of Geology and Geophysics, CAS in Beijing. The 532 nm incident radiation was produced by a 100 mW Laser Quantum Torus consisting of a continuous wave single frequency diode laser. The beam was perpendicular to the thin section, focusing to a width of about 1 μm with a 0.90 numeric aperture (NA) objective during the analyses. Filters decreased the laser power to 0.3 mW on the sample surface. Data were collected in the range of 100 to 4000 cm^{-1}.

Peak positions, widths, relative intensities and areas of the CM were obtained by fitting the spectra using the *MagicPlot* software (Magicplot Systems LLC, Saint

Petersburg, Russia). A mixed Gaussian-Lorentzian curve-fitting method following Hu et al. (2015) was applied to deconvolute the Raman spectra and obtain parameters including the position of peaks, intensity, half width at half maximum height (HWHM) and integrated area. In brief, several splines are created and set at appropriate fit intervals to remove the background. The Gaussian or Lorentzian curves were initially inserted into the spectra manually, and then *MagicPlot* was used to refine the fit. During the fitting process, the parameters of fit function were varied iteratively to minimize the residual sum of squares. The peak positions in the first-order region between 900 and 2000 cm^{-1} included D, G, D1, D2, and D3. Three peaks (S1, S2, and S3) were fit in the second-order region between 2300 and 3500 cm^{-1} (Beyssac et al., 2002; Sadezky et al., 2005; Sforna et al., 2014). Ratios characterizing the Raman spectra, R1, R2, R3, and R4 were calculated by the formulas following Hu et al. (2015). The results are given in Table 4.

Paragenesis and nature of sulfides

The overprinting, overgrowth and brecciation relationships at Daqiao described above record a sequence of fluid-flow events. The various generations of sulfides are interpreted to have grown during the sedimentary and hydrothermal history, and can be divided into four stages (S1–4): syngenetic or diagenetic pre-ore stage S1; hydrothermal early-ore stage S2 associated with breccia A; main-ore stage S3 associated with breccias B and C; and late-ore stage S4 (Table 1). Cyclic mineral zonation textures indicate that there may have been switching between S2 and S3 conditions over the ore fluid evolution, that is, between conditions of tectonic and hydraulic brecciation. Within the interpreted paragenesis, sulfides from different styles of mineralization have been grouped into six types: pyrite 1 (py1) to pyrite 6 (py6); and marcasite 1 (mc1) to marcasite 4 (mc4), based on morphology, internal texture, and zoning.

Stage 1 (S1)

The S1, syngenetic or diagenetic py1 in sedimentary rocks occurs as deformed layers that were originally aligned parallel to bedding (Fig. 5A) or as nodular aggregates associated with the development of quartz pressure shadows (Fig. 5B). Py1 in both locations occurs as polyframboids about 5 to 20 μm in diameter (Fig. 8A) and recrystallized sooty anhedra up to 1 mm across (Fig. 8B-D), intergrown with minor amounts of galena, PGE minerals, and silicates in the interstices of these grains. Py1 is preferentially hosted in pyritic carbonaceous black shale interlayers in the Triassic turbidites.

Stage 2 (S2)

The early-ore S2 consists of abundant fine-grained hydrothermal sulfides including py2 to py4, mc1, mc2 and minor base metal sulfides. The S2 sulfides mainly occur as disseminations in the silicified breccia A (Fig. 4C) or in thin quartz veins or veinlets broadly concordant with foliation in the altered slate (Fig. 5C).

Py2 is euhedral to subhedral, between 100 and 600 μm in diameter. It locally surrounds and overgrows anhedral porous cores of sooty diagenetic py1 with inclusions of galena and silicate minerals (Fig. 8B-D). In many cases, py2 euhedra are overgrown or enveloped by later hydrothermal euhedral mc1 and/or py3 along the grain margins (Figs. 8B, D, 9A).

Py3 commonly overgrows cores of py2 as thin rims (10–100 μm thickness) and is further overgrown by porous py4 (Fig. 9). Py3 is characterized by narrow internal cyclic elemental zones with a high average atomic mass (Fig. 9A). Py3 aggregates were in some cases partially dissolved, and reprecipitated to form porous py4, which preserves irregular relics of py3 (Fig. 9B, C, E, F).

Disseminated py4 was the latest pyrite type precipitated in breccia A before hydraulic brecciation and formation of breccias B and C occurred. Py4 features characteristic porous aggregates with common fine-grained, unoriented inclusions such as apatite, chalcopyrite, galena, and silicates (Fig. 9A-C). Locally, porous py4 is intergrown with minor hematite (Fig. 9D). Py4 commonly surrounds relics of inclusion-free py3, and is overgrown by mc2 and mc3 (Fig. 9E, F).

Mc1 commonly occurs as euhedral or anhedral porous aggregates that overgrow py2 euhedra, which themselves envelop sooty py1 cores. The porous mc1 rims and crystals are up to 100–200 μm across, exhibit strong anisotropy and a tabular morphology, and are typically homogeneous in texture without any compositional zonation in the BSE images (Fig. 8B, D).

Irregular or euhedral mc2 constitutes the most abundant form of marcasite in the disseminated breccia A ores. Strongly anisotropic mc2 grains with yellowish-brown to grayish-blue polarization colors are coarse (0.2–2 mm), usually adjacent to or overgrowing porous py4 aggregates, and intergrown with mc3 and minor amounts of arsenopyrite (Figs. 7D, 9E, F, 10). Minor hydrothermal native platinum is also found as intergrowths with the mc2 (Fig. 10C).

Stage 3 (S3)

The main-ore S3 stage is characterized by cement-related sulfide generations, py5a, py5b, mc3, and minor arsenopyrite, all hosted mainly in breccias B and C. These sulfides are closely associated with traces of two-stage hydraulic fracturing in the strongly silicified turbidites. Fine-grained py5a is intimately related to the early hydraulic fracturing, mainly occurring in the milky-white microcrystalline quartz-pyrite cements of breccia B (Fig. 5E). Py5b and mc3 commonly occur in the later calcite-chalcedony-sulfide veins that intrude or cement breccia B (Fig. 5F, G). In addition, py5a, py5b and mc3 can all be found as fine-grained hydrothermal disseminations overprinting early stages of sulfides in the black silicified siliciclastic tectonic breccia A.

Py5a grains are irregularly disseminated, discrete, porous, arsenic-zoned microcrystals (10–50 μm; Fig. 11A). They also exhibit polyframboid textures comprising spherical to ovoid aggregates of pyrite microcrystals (1–3 μm), found commonly as overgrowths on euhedral py3 and mc2 crystals and porous py4 aggregates (Fig. 11B). Py5a in these breccia B cements is therefore inferred to have formed during the hydrothermal stage, although its framboidal texture is analogous to that displayed by the laminated or nodular diagenetic py1.

S1 and S2 sulfides are crosscut by colloform py5b veins (Fig. 11C). Colloform py5b, typically 50–200 μm in diameter, occurs as rounded to subrounded globules characterized by concentric rhythmic cryptocrystalline bands (Figs. 7C, 11D). Fine-grained unidentified U-Sb-Fe-Pb-Si oxides determined by EMPA are commonly intergrown with colloform pyrite, and occur as anhedral grains of 5 to 20 μm diameter in the cement of breccia C.

Mc3 is bright in the SEM images, and can be easily distinguished from other marcasite generations (Fig. 10). It commonly occurs as irregular cyclic zones with a cloudy texture (5–50 μm) in mc2, replacing clear coarse-grained mc2 along potential internal cleavages or at interstices of mc2 grains (Fig. 10B), or as regular zoning (~10 μm) on the rims of mc2 (Fig. 10A, C, D). In the latter case, zones of mc3 are surrounded in turn by thin mc2 overgrowths (5–100 μm). Mc3 also co-exists with minor extremely fine-grained arsenopyrite in the outermost rim of the coarse-grained mc2 aggregates (Fig. 10C, D). Porous py4 relics are overgrown by homogenous mc2 that incorporates mc3 zonation, and by arsenopyrite grains (Figs. 9E, F, 10D).

Arsenopyrite is not common at Daqiao, but minor amounts of arsenopyrite were observed as veinlets within mc2 and mc3 aggregates adjacent to porous py4, or as extremely fine-grained granular or acicular grains (1–10 μm) spatially associated with mc3 zones in hydrothermal mc2 (Fig. 10C, D).

Stage 4 (S4)

In late-ore S4 calcite veins in weakly silicified pelitic slates, marcasite is commonly more abundant than pyrite (Fig. 5H). Mc4 occurs as coarse-grained (1–2 mm) euhedral aggregates, which are relatively homogeneous with no inclusions and overgrow mc2 and mc3 (Fig. 11E). There is also minor hydrothermal pyrrhotite in the calcite veins, which is not related to the auriferous sulfide paragenesis presented herein. Disseminated py6 is commonly inclusion-free and euhedral (50–300 μm) without any hydrothermal replacement. In some cases, py6 grains co-exist with minor amounts of fine-grained barite grains (5–40 μm; Fig. 11F). Paragenetic sequence of

Daqiao gold mineralization is summarized in Figure 12.

Trace Element Associations and Mapping

Trace element compositions of various sulfides determined by LA-ICP-MS from the ores and proximal sedimentary host rocks are given in Appendix Table A1 and summarized in Table 2. The data include 22 analyses on py1, 30 on py2, 26 on py3, 17 on py4, 14 on py5a, 13 on py5b, 5 on py6, 27 on mc1, 30 on mc2, 21 on mc3, and 12 on mc4. The reported mean concentrations for trace elements were calculated assuming that concentrations are zero for spot analyses below detection limit (b.d.l.). Trace element concentrations below detection limits are shown as half of the detection limits values of the LA-ICP-MS instrument on the diagrams (Figs. 14-16).

Composition of pyrite in pre-ore S1

The fine aggregates of nodular or framboidal diagenetic py1 in black shales interleaved with turbidites at Daqiao are commonly enriched in a range of chalcophile elements, the most abundant of which are Mn, Co, Ni, Cu, As, Sb, Mo, Bi, and Pb (Figs. 13-16). Only three of twenty-two spot analyses reveal detectable gold. Gold content in diagenetic py1 varies from b.d.l to 0.41 ppm with a mean of 0.05 ppm and standard deviation (s.d.) of 0.13 (n = 22), while arsenic varies from b.d.l to 1,819 ppm (mean = 566 ppm, s.d. = 438, n = 22). The only trace element pair that shows a significant correlation in py1 is Co and Ni (correlation coefficient $r_{\mathrm{Co, Ni}} = 0.75$), with Co/Ni = 0.57. The large range of values for Cu, Zn and Pb, especially Pb (Fig. 16A) in py1 is likely due to the abundant microinclusions of chalcopyrite, sphalerite and galena (Fig. 8C, D). Trace element mapping results show that some diagenetic py1 aggregates have a core relatively enriched in Pb, Sb and minor Cu compared to the enveloping non-porous py2 and mc1 aggregates (Fig. 17).

Composition of pyrite and marcasite in early-ore S2

Euhedral py2 is depleted in most of elements compared to nodular diagenetic py1 (Figs. 13-16, 18A). The Au content varies from b.d.l to 1.10 ppm with a mean of 0.09

ppm (s.d. = 0.30, n = 30), whereas As mostly varies from 46 to 1,347 with a mean of 439 ppm As (s.d. = 365, n = 30). LA-ICP-MS mapping results show no clear growth zoning and As is the only trace element enriched in py2 (Fig. 17), as most other analyzed elements are depleted (Fig. 18A).

Euhedral py3 is enriched in selected trace elements compared to py1 and py2 (Figs. 13-16, 18A). About 80 percent of the py3 analyzed has a relatively high gold content, with values between 0.19 to 4.64 ppm and a mean of 0.84 ppm (s.d. = 1.20, n = 26). The arsenic concentration in py3 is much higher than that in py1 and py2, with a large range from b.d.l to 87,444 ppm (mean = 7,294 ppm, s.d. = 17,082, n = 26), and positively correlated with gold concentrations ($r_{\mathrm{Au, As}}$ = 0.55; Fig. 14A). There is little variation in the Au and As counts with progression of the LA-ICP-MS analysis (Fig. 19A).

In contrast to the earlier generations of pyrite, porous anhedral py4 is enriched in trace elements V, Cu, Zn, Ag, Sb, Hg, Tl, Pb, Bi, Sn, W, but not in Au, As, Co, or Ni (Figs. 13-16, 18A). The gold content of py4 varies from b.d.l. to 2.85 ppm with one exception of 5.67 ppm (mean = 0.70 ppm, s.d. = 1.44, n = 17). Only 41 percent of the py4 analyses contain Au above the detection limit, compared with 73 percent of the py3 analyses (Table A1). The arsenic content varies from b.d.l to 8,031 ppm (mean = 790 ppm, s.d. = 1,921, n = 17), showing a positive correlation with Au ($r_{\mathrm{Au, As}}$ = 0.65; Fig. 14A). Notably, py4 shows significantly higher Cu and Zn contents (means of 90 ppm and 147 ppm, respectively; Fig. 18A), consistent with the numerous microinclusions of chalcopyrite and sphalerite intergrown with py4 aggregates (Fig. 9D). Porous py4 shows some chemical similarities with the clean euhedral py3 (Fig. 18A), such as discrete but overlapping ratios of Au/Sb, Au/Tl, Au/Pb, and Co/Ni (Figs. 15, 16).

Three of the twenty-seven spot analyses of mc1 show low gold contents ranging from b.d.l. to 0.24 ppm with a mean of 0.02 ppm (s.d. = 0.07, n = 27; Fig. 14A). Arsenic contents are also low and vary from b.d.l. to 223 ppm with a mean of 26 ppm (s.d. = 49, n = 27). Trace element mapping shows that the mc1 aggregates are slightly enriched in Sb, Cu, Tl, Pb, Hg and Au except for As, compared to py2 euhedra and py1 inclusions therein (Fig. 17).

The inclusion-free mc2 is poor in trace elements compared to py1, but is enriched in Bi, Ag, Sb, Au, Hg, Tl, Cu, Zn, and Sn relative to mc1 (Fig. 18B). The Au content of mc2 varies from b.d.l. to 1.33 ppm with a mean of 0.14 ppm (s.d. = 0.28, n = 30), whereas As varies from b.d.l. to 200 ppm with a mean of 29 ppm As (s.d. = 45, n = 30), with no obvious correlation between Au and As ($r_{\mathrm{Au,\,As}}$ = 0.22; Fig. 14A). Except for minor trace elements such as As, Ag, Sb, and Cu, mapping reveals no clear element enrichment or growth zoning in mc2 (Fig. 20).

Composition of pyrite and marcasite in main-ore S3

Py5, consisting of the concretionary, framboidal, As-zoned, microcrystalline py5a, and colloform py5b, is commonly the most enriched in gold and arsenic of all the pyrite types (Figs. 13, 14A, 18A; Table 2). The majority of spot analyses for py5a show gold and arsenic ranging from 0.35 to 142.95 ppm (mean 27.35 ppm, s.d. = 46.69, n = 14) and 1,108 to 15,399 ppm (mean 6,131 ppm, s.d. = 4,844, n = 14), respectively. Similarly, most py5b analyses show a gold content between 0.20 and 62.26 ppm (mean = 9.71 ppm, s.d. = 16.85, n = 13) and arsenic varies from 2,903 to 38,584 ppm (mean 13,569 ppm, s.d. = 9,347, n = 13). In addition to the high gold and arsenic, py5a and py5b contain elevated concentrations of other trace metals (Fig. 18A), including Sb (mean = 1,852 ppm vs. 1,133 ppm), Hg (982 ppm vs. 1,087 ppm), and Tl (866 ppm vs. 1,641 ppm). However, py5b shows much lower concentrations of Zn, Ag, and Pb than py5a (mean = b.d.l. vs. 53 ppm for Zn, 0.5 ppm vs. 93.75 ppm for Ag, and 0.17 ppm vs. 27.68 ppm for Pb). Although enriched in Au and other trace elements, py5 and especially py5b, is commonly depleted in elements characteristic of the diagenetic py1, in particular, Co, Ni, Mo, Pb, and Bi (Fig. 18A). Both py5a and py5b are generally characterized by a high Au/Ag ratio (Fig. 14B) and a consistent Hg/Tl ratio ($r_{\mathrm{Hg,\,Tl}}$ = 0.72; Fig. 16B), and show markedly similar chemical features (Figs. 13-16, 18A). Spot analyses and elemental mapping conducted on the rims and the cores of colloform py5b show that the cracked cores are significantly enriched in Au and most other analyzed elements except Pb relative to the bulk rims (Fig. 21).

Analysis indicates that most of the narrow cyclical zones of mc3 have gold contents of 0.2 to 43.12 ppm (mean = 5.94 ppm, s.d. = 12.30, n = 21; Figs. 13, 14A, 18A), making it the most auriferous marcasite at Daqiao. Moreover, mc3 also has elevated concentrations of other trace elements including As (mean 1,112 ppm), Ag (22.2 ppm), Sb (724 ppm), W (14.94 ppm), Hg (195 ppm), Tl (242 ppm), and Pb (64.21 ppm), but is poor in Co, Ni, Mo, Pb, and Bi as observed in py5a and py5b (Fig. 18). There is an obvious positive correlation between Au-As ($r_{Au, As}$ = 0.86), and weak or no correlation between Au-Sb, Au-Tl, and Au-W (Figs. 14, 15). Similar to the LA-ICP-MS counts output by laser ablation for pyrite, the time invariant trace of the spot analysis and the positive correlation between As and Au indicate that Au and As are most probably contained as solid solution or as nanoparticles in mc3 rather than as inclusions of free gold (Fig. 19B). The difference of trace element concentrations between mc2 and mc3 is clearly displayed in the LA-ICP-MS trace element maps of a coarse-grained mc2 overgrown by mc3 zoning (Fig. 20). The narrow zoned mc3 overgrowth is relatively enriched in As, Au, Sb, Cu, Tl, Hg, and minor Pb compared to the inner mc2, which contains only minor amounts of Sb, Cu, and Ag.

Composition of pyrite and marcasite in late-ore S4

Both the coarse-grained py6 and mc4 have low As, Au, and Sb concentrations compared to earlier varieties (Figs. 13-16, 18). One in five analyses of the py6 shows a detectable gold content of 0.23 ppm with other analyses below detection limits, and the arsenic varies from 17 to 884 ppm with a mean of 242 ppm (s.d. = 325, n = 5). No gold was detected by LA-ICP-MS in any of the euhedral mc4 aggregates, and the As content ranges from b.d.l. to 96 ppm with a mean of 31 ppm (s.d. = 33, n = 12). Spot analyses indicate that marcasite of all types commonly contain less invisible gold and other trace elements than co-existing pyrite.

Sulfur isotope compositions of sulfides

The sulfur isotope compositions measured by in situ laser ablation MC-ICP-MS are presented in Table 3 and graphically illustrated in Figures 22–24. The results reveal a notable variation in S isotopes from py1 to py6 and mc1 to mc4.

$\delta^{34}S$ of pyrite

The δ^{34}S values of the five analyses of py1, considered to have formed during sedimentation or diagenesis, show a fairly wide range of -30.9 to +6.7‰ with a mean δ^{34}S of -5.1‰ (s.d. = 13.8, n = 5; Figs. 22, 23A). Microscopic grain-scale variations in sulfur isotope compositions are noticeable in some py1 grains. One of these grains has δ^{34}S values of +2.5 to +7.5‰ in the core, with an abrupt decrease to -31‰ on the margin (Fig. 24A, C). The signal (V) for ^{32}S also decreases remarkably from 1.6 to 0.9 on the contact area between the core and rim due to the porous internal texture (Fig. 24C). The line analysis results are consistent with δ^{34}S values obtained from spot analyses, suggesting that these analyses are not affected by artifacts relating to the porosity.

Twenty-two spot analyses on disseminated euhedral py2 grains yield δ^{34}S values of -6.2 to +22.0‰ with a mean of +4.2‰. Py3 is also enriched in ^{34}S compared to py1 and py2, with δ^{34}S values ranging from +0.4 to +8.7‰ (mean = +5.2‰, s.d. = 2.4, n = 17). In more detail, 77% of the data falls between +4.0 and +8.7‰. Eleven spot analyses on porous py4 show a relatively restricted range and somewhat lower values of δ^{34}S, from +1.2 to +6.3‰ with a mean of +3.4‰ (s.d. = 1.3, n = 11; Figs. 22, 23A).

The δ^{34}S values of cement-related py5a framboids and microcrystal aggregates are distinctively low compared to the earlier pyrite hydrothermal generations, with a range of -13.9 to +1.4‰ (mean = -7.3‰, s.d. = 5.3, n = 6). Similarly, colloform py5b has a relatively uniform range of sulfur isotope compositions, ranging in δ^{34}S from -9.9 to -0.7‰ (mean = -6.0‰, s.d. = 2.8, n = 12; Figs. 22, 23A). Spot analyses both on the rims and the cores of py5b show that the rounded cracked cores are enriched in ^{34}S compared to the rims (Fig. 11D). Conversely, the rims are significantly enriched in Au and As relative to the cores. The late-ore stage py6 has extremely negative δ^{34}S values, ranging from -27.8 to -8.3‰ (mean = -19.5‰, s.d. = 6.8, n = 5).

$\delta^{34}S$ of marcasite

The mc1 aggregates range in δ^{34}S from -7.7 to +4.9‰ (mean = -0.8‰, s.d. = 3.3, n = 29) with 76% of the data falling between -1.9 and +4.9‰ (Figs. 22, 23B). Seventeen spot analyses on mc2 show a variation in $\delta^{34}S$ values from -1.2 to +11.4‰ with a mean of +5.0‰ (s.d. = 3.9, n = 17). Mc3 has $\delta^{34}S$ values ranging from -21.1 to -1.2‰ with a mean of -9.7‰ (s.d. = 6.2, n = 6).

The chemical zonation seen in marcasite is mirrored by contrasts in sulfur isotope compositions. As the laser burns through high As mc3 zones hosted by low As mc2, the $\delta^{34}S$ values show a decrease to as low as -20‰ in contrast to the $\delta^{34}S$ values varying from 0 to +15‰ obtained from the inner coarse mc2 euhedron (Fig. 24B, D). The signal in ^{32}S remains at the same level throughout both the mc2 and mc3. Extremely negative $\delta^{34}S$ in a narrow range of -31.3 to -22.6‰ (mean = -26.3‰, s.d. = 3.8, n = 5) are found in mc4, consistent with values obtained for the coeval py6 (-27.8 to -8.3‰) in the late-ore hydrothermal stage (mean = -19.5‰, s.d. = 6.8, n = 5; Figs. 22, 23B).

Raman spectra of carbonaceous material

Raman spectra were measured on disseminated CM in samples DQ222 (non-carbonate carbon = 0.46 wt %, 2.18 g/t Au) and DQ224 (non-carbonate carbon = 1.48 wt %, 4.78 g/t Au). Both samples are examples of the typical intensively-silicified breccia A, which contain mainly disseminated sulfides from the early S2 stage without clear overprinting by subsequent hydraulic fracturing. CM in both samples has almost identical features based on the morphology, size, texture (Fig. 6), and Raman spectra observations.

CM in these two samples is characterized by high intensity and relatively wide D and G peaks (Fig. 25), with 30.3–42.9 cm^{-1} HWHM of the D band and 20.8–32.5 cm^{-1} HWHM of the G band. The position of the D band is at 1344.8~1351.9 cm^{-1} while the G band is at 1595.9~1609.2 cm^{-1}. Other bands are D1 (~1203 cm^{-1}) and D2 (~1578 cm^{-1}) in the first-order region and S1 (~2690 cm^{-1}), S2 (~2940 cm^{-1}) and S3 (~3203 cm^{-1}) in the second-order region (Fig. 25). The R1 ratio of the intensity of the D and G peaks (I_D/I_G) is relatively high (1.68–2.24). R2, the ratio of the width of the

D peak to that of the G peak (W_D/W_G) clusters at values of 1.00–1.79. R3, the ratio of the total area of D peaks to the total D and G peak areas, is the same in the two samples (0.65–0.72). R4, the ratio of the S1 peak to the total S peak area, is consistently low at 0.42–0.62.

Temperature is the key factor in the graphitization process of CM (Beyssac et al., 2002). An applicable geothermometer for CM, based on the linear correlation between its Raman spectra parameters of the relative intensity (R1), areas (R3) of the D and G peaks, and the peak metamorphic temperature (100 to 700 °C) has been developed (Beyssac et al., 2002; Rahl et al., 2005). It has been applied to estimate the temperature recorded by CM using Eq. (1) in sediment-hosted gold deposits (Hu et al., 2015; Eq. 1):

$$T\ (°C) = 737.3+320.9R1-1067R3-80.638R1^2. \qquad (1)$$

The Raman-derived temperatures (T_R) obtained from the above equation range from 283 to 355 °C with a weighted mean value of 320 ± 4 °C (n = 26).

Discussion

Gold introducing episodes

Breccia textures, ore mineralogy and mineral paragenesis consistently provide evidence for repeated brecciation and mineralization events at Daqiao gold deposit (Figs. 4-7), in which two distinct types of gold introduction are proposed. The earliest mineralization is marked by introduction of invisible gold in sulfide disseminations mainly found in breccia A that formed during the early-ore stage S2, whereas later mineralization is characterized by invisible gold enrichment in the irregular cement-hosted sulfide aggregates that formed in breccias B and C during the main-ore stage S3 (Fig. 14A; cf. Reich et al., 2005). While there is an overall transition from S2 to S3 recorded by overprinting textures, the zoned marcasite with repeated cycles of mc2-mc3-mc2 indicates oscillation between conditions responsible for the formation of S2 and S3 textures (Fig. 10).

It is notable that py1 is enriched in certain trace elements, such as Co, Ni, Mo, Pb, and Bi, relative to all of the hydrothermal sulfide generations (py2 to py6 and mc1 to mc4) at Daqiao (Fig. 18). Some element concentrations (e.g., Mn, Co, Ni, Mo, Pb, and Bi) may be artificially elevated because of the porosity of py1, which contains approximately 10 vol % matrix commonly found in sedimentary rocks (e.g. Mn carbonate) or CM, which can concentrate metals during sedimentation and diagenesis of organic-rich sediments in euxinic environments (Rimmer, 2004; Large et al., 2007, 2009, 2014; Gregory et al., 2016). Enrichment of Sb in py1 is thought to be derived from the high supply during sedimentary process (Large et al., 2014). The element suite in py1 is similar to that of diagenetic pyrite at Bendigo, Australia, reported by Large et al. (2009) and Thomas et al. (2011), and at Yilgarn, Australia by Steadman et al. (2015) and Gregory et al. (2016).

The tectonic breccia-related mineralization produced relatively low gold concentrations locked in the structure of arsenian pyrite (py2, py3, py4) and marcasite disseminations (mc1, mc2) in breccia A (Figs. 13, 18). The mean gold concentrations in py2 to py4 are 0.09 ppm, 0.84 ppm and 0.70 ppm, respectively and 0.02 ppm and 0.14 ppm for mc1 and mc2. Low concentrations of Au, As and other metals are also documented by the LA-ICP-MS mapping of these sulfides (Figs. 17, 20), suggesting that the early-stage hydrothermal fluid carried limited gold and arsenic.

Subsequent to this early gold introduction episode, the majority of the high As, cyclically-zoned py3 was extensively modified or dissolved along fractures and/or grain boundaries, the relics of which were overgrown and enveloped by porous py4 (Fig. 9). Py4 has a close chemical affinity to py3, though with elevated Ag, Sb, Hg, Tl, Cu, Zn and Pb relative to the latter (Fig. 18A). Enrichments in those trace elements are likely caused by inclusions of chalcopyrite and other silicates (Fig. 9B, D). Py3 is slightly more enriched in Au than py4 (Fig. 23A). 73% of the spots on py3 have detectable Au averaging 0.84 ppm, whereas only 41% spots on py4 show detectable Au with a mean of 0.70 ppm. Similarly, py3 contains significantly higher As than py4 (mean of 7,294 ppm in py3 vs. mean of 790 ppm in py4). We therefore suggest that py4 may have formed during continuous hydrothermal overprinting and dissolution of py3 triggered by fluctuations in ore fluid chemistry. This dissolution-reprecipitation process likely led to the liberation and remobilization of gold and arsenic from the structure of py3 that was then added to the gold and arsenic budget of the infiltrating fluid (e.g., Cook et al., 2009; Sung et al., 2009).

The majority of gold and associated trace elements (Ag, As, Sb, Hg, Tl, W, and U) were introduced during the main-ore stage, suggesting that the hydrothermal fluid carried high metal budgets during this stage. These trace elements are now found mostly within the anhedral cement-hosted py5a, py5b and mc3 in the breccias B and C (Figs. 11, 13, 18, 20, 21). The last sulfide inferred to form during this main-ore stage is py5b, which displays a weak Au-As correlation and is depleted in most elements except for Bi, As, and Tl relative to py5a and mc3 (Fig. 18). The marked similarity in mineralogical (Figs. 10, 11A-D) and chemical features (Figs. 13, 18) of py5a, py5b and mc3 suggest that they precipitated successively or almost simultaneously from an evolving ore fluid. This notion is further supported by textural similarities between the hydraulic breccias B and C (Figs. 4, 5). After hydraulic brecciation, the less economically significant late-ore sulfides, including coeval py6 and mc4, characterized by a low-concentration trace element signature, was likely to have formed from a metal-poor hydrothermal fluid. Trace element affinities combined with similar mineral associations between the early- (S2) and main-ore (S3) stages (Fig. 18) suggest that gold and other metals may be derived from a single ore fluid source, while the variation of some trace element distributions in sulfides may reflect the chemical and physical evolution of ore fluid and/or that sulfides were overprinted by the subsequently evolving ore fluid.

The source of gold

Gold and arsenic in Phanerozoic sediment-hosted gold deposits are commonly thought to be derived from underlying fertile Precambrian metamorphic rocks (Groves et al., 1998; Phillips and Powell, 2010; Tomkins, 2010, 2013a, 2013b). Greenschist-facies or higher grade metamorphism of turbidites has been shown to effectively release Au, S, and As from diagenetic pyrite, a key process in the formation of some orogenic gold deposits, such as those in Southern Alps of New

Zealand (Pitcairn et al., 2006) and the Victorian goldfields in Australia (Wilson et al., 2013). It has also been suggested that gold in these deposits is largely derived from precursor syngenetic to diagenetic auriferous pyrites in the host rocks (Large et al., 2007, 2009, 2011). Accordingly, the concentration and association of gold and trace elements from syngenetic to diagenetic pyrites, both in the Triassic host rocks and the underlying Paleozoic metasedimentary rocks, provide information on the role that these pyrites played in gold mineralization at Daqiao.

At Daqiao, some of the synsedimentary to diagenetic py1 from the black shale interlayers within the Triassic turbidites contains detectable gold (mean 0.05 ppm Au; three of the twenty-two spot analyses) and other trace elements (e.g., Co, Ni, Sb, Mo, Pb, and Bi), with Co/Ni ratios averaging 0.57 (Fig. 16D). These geochemical features are comparable with typical diagenetic pyrite from locations where deposition in euxinic environments has been inferred (Price, 1972; Large et al., 2009, 2014; Thomas et al., 2011; Gregory et al., 2016). LA-ICP-MS trace element results show that the hydrothermal sulfides contain elevated Au, Ag, As, Sb, Hg, Tl, and W, and display a dissimilar trace element pattern to the diagenetic py1 (Figs. 13, 18). This difference does not eliminate the Triassic diagenetic pyrites as an Au source, since trace elements can be decoupled during pyrite recrystallization (e.g., Large et al., 2011).

However, it is commonly considered that gold and other trace elements (Ag, As, Sb, Hg, Mo, and W) in diagenetic pyrite are expelled during the pyrite-pyrrhotite transition, which is driven by increasing temperature between 450°C and 600°C (Pitcairn et al., 2006; Large et al., 2009; Tomkins, 2010), or by reduction (Carpenter, 1974; Ferry, 1981; Thomas et al., 2011). As shown by the Raman analyses of the CM from Daqiao, the regional metamorphic temperature is estimated at between 283°C to 355 °C during pumpellyite–actinolite facies metamorphism (250–350 °C), values much lower than the temperatures required for the breakdown of pyrite to form pyrrhotite. Minor hydrothermal pyrrhotite is observed in the S4 coarse-grained marcasite-calcite veinlets, but other than this, the pyrite to pyrrhotite conversion facilitated by reaction with CM, or by other means, is not observed in the host rocks of the Daqiao gold deposits. Under lower grade metamorphism (<400 °C) metals may be locally remobilized on the short scale without changing average concentrations on the hand sample scale between subgreenschist facies rocks and protoliths (Pitcairn et al., 2006). Thus, unless Triassic sediments lie at greater depths within the sedimentary sequence at Daqiao, then their viability as an Au source is fairly low.

Taken together, the lack of matching trace element pattern and pyrite-pyrrhotite conversion suggest that synsedimentary and diagenetic py1 in the immediate surrounding black shales did not contribute gold and other metals to the formation of the Daqiao gold deposit. However, S1 pyrite cannot be excluded as a source of Au if present at deeper levels that were exposed to higher temperatures.

The other possible sedimentary source of Au at Daqiao is the underlying Paleozoic sedimentary rocks. Previous trace element analyses of pyrite-rich carbonaceous black shales in underlying Paleozoic sequences in the WQO reveals elevated Au (130 ppb), As (1,500 ppm), Ag (1,035 ppm), U (19 ppm), V (1,138 ppm), Mo (52 ppm), Pb (136 ppm), and Zn (239 ppm; Tan et al., 1996; Zhang et al., 2009). Devonian carbonaceous phyllites and schists in the WQO, as noted in many sediment-hosted orogenic gold deposits (e.g., Yangshan, Jinlongshan, and Qiuling), are characterized by well-developed laminated diagenetic pyrite framboids that contain 0.1–1.7 ppm Au and 0.2–1.6 wt% As (Zhang et al., 2000; Qi et al., 2003a). Release of these trace elements has been proposed to form orebodies such as those of the La'erma and Pingding gold deposits in the WQO (Fig. 1A; Tan, 1992; Zhang, 1993). The Silurian and Cambrian siliceous rocks and carbonaceous shales that underlie Daqiao are enriched in a variety of trace elements, in particular, Au, As, PGE and U (Tan, 1992; Liu and Zheng., 1993). Interestingly, these elements are unusually high in gold ores of the Daqiao deposit (e.g., up to 384 ppm U). In addition, except for the PGE intergrowths with diagenetic py1 (Fig. 8A, C), gold ores at Daqiao contain hydrothermal PGE and U-rich minerals that are closely associated with the mc2 and py5b, respectively (Figs. 10C, 11D). We therefore suggest that gold, sulfur, arsenic, and other metals in the Daqiao gold deposit were mostly likely sourced from the underlying Paleozoic pyritic shales by breakdown of pyrite to pyrrhotite at a depth of around 12 to 15 km during the greenschist to amphibolite transition (e.g., Pitcairn et al., 2006; Large et al., 2009; Phillips and Powell, 2010; Tomkins, 2010, 2013a, 2013b).

Sources and evolution of ore fluids

Gold is transported predominantly by sulfur ligands in reduced aqueous-carbonic solutions (Phillips et al., 1986; Ohmoto and Goldhaber, 1997; Groves et al., 1998; Ridley and Diamond, 2000; Barker et al., 2009; Hodkiewicz et al., 2009), and sulfur isotope compositions of sulfide minerals can therefore, provide information on the source, transport, and precipitation of gold and genesis of metasediment-hosted gold deposits. The mineral assemblage at Daqiao consists of pyrite and marcasite, with minor stibnite and chalcopyrite, which form at relatively low temperature, low fO_2, and pH-acidic to neutral conditions (e.g., Murowchick and Barnes, 1986). Under these conditions, fractionation between aqueous sulfur and sulfides is minimal, so the measured $\delta^{34}S$ in sulfides is approximately equal to or slightly higher than the bulk sulfur isotope compositions ($\Sigma\delta^{34}S$) of sulfide-precipitating ore fluids ($\Delta^{34}S_{pyrite\text{-}fluid} = 0\sim+1.5‰$; Kajiwara and Krouse, 1971; Ohmoto, 1972; Ohmoto and Rye, 1979).

The $\delta^{34}S$ values of pyrite and marcasite from the Daqiao gold deposit show a broad spread from -31.3 to +22.0‰, but mostly cluster between -10 to +10‰ (Figs. 22, 23). A plausible explanation for the isotopically low $\delta^{34}S$ values of py1 (-30.9 to +6.7‰) is that it formed by reduced sulfur generated by bacterial reduction (BSR) of Triassic marine sulfate with $\delta^{34}S$ of 15–25‰ (Holser, 1997). BSR commonly produces sulfur isotope fractionation between SO_4^{2-} and H_2S of 4 to 46 per mil (mean 21 per mil; Canfield and Teske, 1996; Habicht et al., 1998). The lowest $\delta^{34}S$ value observed for py1 (-30.9‰) suggests BSR may have occurred alongside a process associated with sulfur disproportionation of intermediate sulfur species (e.g., S^0, $S_2O_3^{2-}$ or SO_3^{2-}; fractionation of 7 to 11 per mil; Canfield and Thamdrup, 1994; Habicht et al., 1998; Cheshire and Bish, 2012; Chen et al., 2015).

This large $\delta^{34}S$ range of stage S2 pyrite and marcasite (-7.7 to +22.0‰) is comparable to diagenetic pyrite in the underlying Paleozoic sedimentary sequences of the WQO Devonian phyllite and metagreywacke [-29.0 to +17.5‰, mean = -0.9‰, s.d. = 17.6, n = 12; Qi et al., 2003b; Luo et al., 2004; Yang et al., 2006; Li et al., 2012]; Cambrian black shale [-10.0 to +46.9‰, mean = +13.1‰, s.d. = 11.6, n = 15; Liu et al., 2000]. The broad range of the $\delta^{34}S$ of S2 sulfides suggests that S was sourced from the metasedimentary rocks (Goldfarb et al., 1991; Chang et al., 2008). During regional metamorphism, sulfur and fluids could have been effectively generated by reactions such as breakdown and desulfidation of pyrite in the underlying Paleozoic metasedimentary sequences (Powell et al., 1991; Large et al., 2009; Phillips and Powell, 2010; Tomkins, 2010). Support for this proposal is also provided by the similar signatures of carbon, oxygen and lead isotopes of the Paleozoic sequences and ore-related gangue minerals in other gold deposits in the WQO and surrounding areas (Zhang et al., 2000).

The obvious negative correlation between gold grades and $\delta^{34}S$ values in the main-ore stage 3 pyrite and marcasite in the intensively silicified breccias at Daqiao (Fig. 23) suggests that gold incorporation into sulfides was linked to either the influx of a fluid with a distinct sulfur isotopic composition, or that the ore-forming process caused fractionation of sulfur isotopes (Palin and Xu, 2000; Barker et al., 2009). System disturbances such as a decrease in temperature, pressure, activity of reduced sulfur species, oxidation of the ore fluid, or a pH increase in the ore fluids could have resulted in the destabilization of bisulfide complexes and gold precipitation at Daqiao (McCuaig and Kerrich, 1998; Loucks and Mavrogenes, 1999). The temperature of the hydrothermal stage at Daqiao is thought to be within the range of 100–240 °C based on microthermometry of fluid inclusions in the ore-related quartz from breccia ores (Xu et al., 2015). This temperature condition is further supported by the prevailing occurrence of marcasite, which only forms at temperatures less than 240°C, and below pH 5 (Murowchick and Barnes, 1986). An important factor that may account for the obviously negative correlation between gold and $\delta^{34}S$ is fluid oxidation (Palin and Xu 2000; Hodkiewicz et al., 2009). Fractionation of heavy ^{34}S into the oxidized sulfur species would lead to the relatively ^{34}S depleted H_2S in the residual ore fluid, and the precipitation of sulfides characterized by more negative $\delta^{34}S$ values (Ohmoto and Rye, 1979).

The similar mineral association, lack of clear zonation and changes in trace element affinities between the early- and main-ore stages (Fig. 18) do not support the existence of multiple, chemically distinct, oxidized ore fluids and/or fluid mixing at Daqiao. Further, as there is no exposed intrusion of significant size that could produce sufficient oxidized fluids, ore fluids produced by Paleozoic sediments are likely to be initially reduced and, under certain conditions (e.g., fluid unmixing), became oxidized along some pathways or at depositional sites (Phillips et al., 1986; Golding et al., 1990; Evans et al., 2006).

The most auriferous and complex-textured py5a, py5b and mc3 (e.g., framboids, colloform and cyclic zonation) are cement-hosted in the breccias B and C that formed during the two-stage hydraulic fracturing. Such fracturing implies a rapid depressurization of the ore fluids (Murowchick and Barnes, 1987; Hodkiewicz et al., 2009). Experimental results suggest that framboidal pyrite of hydrothermal origin (e.g., py5a) is the result of the aggregation of uniformly-sized magnetic greigite microcrystals (Fe_3S_4; Wilkin and Barnes, 1997; Ohfuji and Rickard, 2005), at temperatures below 200°C near the oxic-anoxic interface, which separates waters containing dissolved oxygen and sulfide, respectively (Muramoto et al., 1991; Wilkin et al., 1996; Wilkin and Barnes, 1997). The intimate intergrowth of py4 with finely crystalline hematite (Fig. 9D), commonly precipitating from relatively oxidized fluids, provide evidence for increasing ferrous iron oxidation (Haynes et al., 1995). Possible mechanisms for oxidation and depressurization are discussed further below.

The sulfur isotope compositions of the py6 and mc4 in late-ore stage 4 feature strongly negative $\delta^{34}S$ values (-19.5 to -26.3‰), which could be attributed to the continuous fluid oxidation and/or input of sulfur generated by the BSR process from widely distributed Paleozoic black shales in the WQO. Rare fine-grained barite grains are present in stage 4, indicating that ore fluids must have generated a small quantity of isotopically heavier SO_4^{2-}. This process is similar to the proposed increasing fluid oxidation and resultant precipitation of barite and gypsum in the late-ore stibnite stage of Jinlongshan and Qiuling gold deposits in the SQO (Zhang et al., 2000). In addition, the low levels of metals in py6 and mc4 are consistent with precipitation from the late-stage, exhausted ore fluids, rather than from fresh, deeply-derived fluids enriched in gold and other metals (Fig. 18). At the high crustal levels recorded at Daqiao (1 km; Xu et al., 2015), it is possible that, during the late-ore stage, oxidized and cool meteoric water would have been increasingly involved in the precipitation of the last generation of sulfide veinlets (py6 and mc4; Cline and Hofstra, 2000; Zhang et al., 2000), leading to the further oxidation of ore fluids and consequently more negative $\delta^{34}S$ values (Palin and Xu, 2000).

Viability of granodiorite involvement in metasediment-hosted gold mineralization in metamorphic terranes remains ambiguous (Groves et al., 1998; Goldfarb and Groves, 2015). Granodiorite dikes at Daqiao have been subjected to variable degrees of hydrothermal alteration; the few occur that near the orebodies show weak gold mineralization. This observation implies that the dikes are probably pre-ore and would not be significant contributor to ore fluids. This evidence is supported by the broad range of the $\delta^{34}S$ values of the early-ore stage S2 sulfides, which is distinct from that of magmatic or mantle-derived sulfur (0 ± 5‰; Ohmoto and Rye, 1979; Seal, 2006), suggesting that magmatic sulfur is not a big contributor to the ore mineralization. The Co/Ni ratios (mean 0.36, n = 109) of all hydrothermal pyrite and marcasite further support the derivation of metals and fluids from sedimentary source rocks rather than magmatism (Large et al., 2009, 2014). Thus, we infer that the small size of granodiorite dike magmatism is probably not of first relevance to the Daqiao gold mineralization.

Significance of CM

There is a strong association between sediment-hosted orogenic or Carlin-type gold deposits and carbonaceous material (CM; Large et al., 2011; Thomas et al., 2011; Hu et al., 2015, 2016, 2017). In-situ sedimentary CM has been commonly suggested to be important in providing metals during subsequent metamorphism (Large et al., 2011; Hu et al., 2016), and/or as the reducing agents causing gold precipitation (Cox, 1995; Craw et al., 2010; Goldfarb et al., 2007; Zoheir et al., 2008). Alternatively, CM may also be deposited from hydrothermal fluids during gold mineralization with or without a genetic link to mineralization (Gu et al., 2012; Luque et al., 2009; Hu et al., 2017).

Most of the CM from gold ores observed in this study is disseminated and either closely related to or enveloped by irregular porous sulfide aggregates of S2 (Fig. 6). CM at Daqiao does not exhibit typical hydrothermal characteristics, such as CM veinlets paragenetically associated with sulfides or crosscutting the foliation. According to the Raman spectral results, the relatively wide D and G peaks combined with a high R1, R2 and R3, and a low R4 indicate these CM are not well crystallized and have low maturity (Fig. 25; Beyssac et al., 2002). The maximum equilibration temperature of CM at Daqiao from Raman spectra is estimated at 283–355 °C, which is similar to the pumpellyite–actinolite facies metamorphic temperature range (250–350 °C; Hu et al., 2015). This range is, however, much higher than the total homogenization temperature (100–240 °C) of fluid inclusions in the Daqiao gold deposit (Xu et al., 2015). Therefore, we suggest that the dispersed CM at Daqiao may have been present in the host sedimentary turbidites and have progressively transformed into more ordered CM during regional pumpellyite-actinolite facies metamorphism prior to ore fluid infiltration. This view is also consistent with the virtual absence of hydrocarbon species (e.g., C_2H_6, CH_4) in the fluid inclusions at Daqiao (Xu et al., 2015). The presence of these reduced carbon species would support the presence of CM as a migrated hydrocarbon product, as these species are commonly seen in ores from some hydrothermal gold deposits closely associated with paleo-oil reservoirs (Gu et al., 2012; Kříbek et al., 2015). We suggest that the sedimentary CM may have acted as a reductant to cause precipitation of gold from hydrothermal fluids carrying gold as bisulfide complexes, resulting in gold precipitation via a reaction like Eq. (2) (McKeag et al., 1989; Craw et al., 2007; Zoheir et al., 2008; Hu et al., 2015). This reaction is evidenced by the variable amounts of CO_2 are present in the early-ore stage quartz-sulfide veinlets (Gansu Geological Survey, 2017).

$$4Au(HS)_2^- + C + 4H^+ + 2H_2O = 4Au + CO_2 + 8H_2S \text{ (aq)}. \quad (2)$$

The role of CM as a reductant, particularly in the early ore stage, is further supported by the fact that the content of the non-carbonate carbon of the early-ore stage (S2) disseminated ores is relatively high (mean of 0.83 wt%, n = 6) with positive correlation with the varied gold grade ($r_{Au, CM}$ = 0.89; Fig. 26). In contrast, in the main ore stage (S3) breccia ores characterized by large-volume cements of carbonate-quartz-chalcedony-auriferous pyrite aggregates, the non-carbonate carbon content is relatively low (0.28 wt %, n = 5) and no correlation with gold grade exists ($r_{Au, CM}$ = 0; Fig. 24). We note that sulfidation of reactive iron-rich host rocks, especially for mafic to ultramafic rocks or banded iron formations, is another likely mechanism for the destabilization of hydrosulfide complexes and gold precipitation in close association with disseminated auriferous arsenic sulfides (Phillips and Groves, 1984; Kesler et al., 2003). However, the availability of excess non-sulfide Fe, which would be available mainly in iron-bearing carbonate, chlorite, or phengitic muscovite in sedimentary rocks, is limited in the widespread Middle to Upper Triassic turbidites in the WQO. The average content of Fe_2O_3 in these turbidites is 3.20 wt% (n = 204; He, 2008), much lower compared to that of sub-greenschist facies meta-basalts (mean Fe_2O_3 = 11.30 wt %, n = 11; Pitcairn et al., 2015). Sulfidation of an iron-rich protolith is therefore considered unlikely to have played a major role in Au deposition.

Significance of multistage hydraulic fracturing

The most auriferous sulfides with complex textures have the most negative $\delta^{34}S$ values, other than the negative values in the S4 sulfides, and are associated with occurrence of the microcrystalline quartz and chalcedony in the cements formed during the main-ore stage 3 at Daqiao (Figs. 5E-G, 7B, C). These ores are strongly associated with multistage hydraulic fracturing (see above; Figs. 4B, D, 5D-G). Cassidy (1992) and Witt (1995) suggested that hydraulic fracturing and intermittent release of overpressured fluids, concomitant phase separation and fluid immiscibility are the main mechanisms of gold deposition in orogenic gold deposits hosted in low-Fe rocks. Partitioning of H_2S into the vapor phase leaves, at least temporarily, the ore fluid relatively oxidized with higher SO_4/H_2S ratio and ^{34}S depleted H_2S in the residual ore fluid (Drummond and Ohmoto, 1985; Ohmoto and Rye, 1979). More importantly, a combination of the decrease in the total activity of sulfur ($a\Sigma S$) and ore fluid oxidation would result in a rapid decrease in gold solubility and thus rapid precipitation of auriferous pyrite and chalcedony (Sibson, 1986; Hodkiewicz et al., 2009).

Pyrite with framboidal morphology in low-temperature organic-rich sediments (e.g. py1 at Daqiao) is commonly interpreted as biogenic in origin (Love, 1971; Love et al., 1984; Donald and Southam, 1999; Butler and Rickard, 2000). However, pyrite framboids formed via inorganic synthesis have been experimentally documented (Wilkin and Barnes, 1997) and have been recorded in a variety of hydrothermal deposits such as massive sulfide deposits (Chen, 1978), epithermal vein-type deposits (Allen and Hahn, 1994), and metasediment-hosted gold deposits (Scott et al., 2009). Py5a polyframboids at Daqiao commonly occur as disseminations or overgrowths in the microcrystalline quartz-pyrite cements and silicified sandstone breccias. These textures support a hydrothermal origin, as does the colloform texture of py5b, both of which form by closely related processes (Berner, 1970). The large number of crystal nuclei responsible for these textures are attributed to relatively high nucleation and growth rates at high degrees of FeS_2 supersaturation (Roedder, 1968; Farrand, 1970). Thus, rapid crystallization of the main-ore stage py5a framboids, colloform py5b and narrow rings of mc3 associated with gold concentrations are proposed to have occurred during short-lived depressurization episodes associated with hydraulic fracturing (Phillips, 1972; Barker et al., 2009). Further, the cycling between mc2 and included mc3 rings (Fig. 10) indicates local, chemically heterogeneous, cycling of ore fluids during the complex processes of hydraulic fracturing.

Genetic model for the Daqiao gold deposit

Multiple gold-depositional processes were most likely significant in the formation of the Daqiao gold deposit (Fig. 27). In the early-ore stage S2, deep-seated metamorphic ore fluids discharged from regional thrust faults, such as the crustal

HLLF and ZCHF and the secondary YSF, were channeled beneath the low-permeability seals formed by Triassic black shales, pelitic slates and local limestone that cap the hydrothermal system, resulting in dispersed reaction of fluids with pre-existing sedimentary CM in the Triassic turbidites and formation of the disseminated gold-bearing arsenic sulfides (cf. Phillips et al., 1986; Evans et al., 2006). This suggestion is supported by the close spatial and temporal association between early stage silicification and S2 sulfidation at Daqiao (Fig. 3). The intensive tectonic brecciation between the Triassic slates and Carboniferous limestone also provided a ready means to channel fluids for gold deposition. Moreover, the early stage hydrothermal microcrystalline quartz could have preferentially replaced the preexisting wall-rock plagioclase and carbonate in the high-permeability and chemically active calcareous or siliceous siltstone (Chen et al., 2004) and cemented tectonic breccia A (Fig. 7F). This infiltrative silicification also resulted in significant competency contrasts between the silicified clastic rocks and low-permeability shale seals. During the main-ore stage S3, hydraulic fracturing in the competent silicified rocks and subsequent rapid fluid-pressure fluctuations caused phase separation, leading to ore fluid oxidation, and fast gold precipitation (Phillips et al., 1984; Cassidy, 1992; Witt, 1995), mainly in the form of cement-hosted fine-grained sulfides with high gold and arsenic contents. The cycling between mc2 and incorporated mc3 rings indicates periodic ore fluid fluctuations during the hydraulic fracturing processes.

Although the Daqiao gold mineralization shows some features analogous to the Carlin deposits in the Great Basin of western North America, such as the pervasive silicification, low temperature geochemical suite (Au-Ag-As-Sb-Hg-Tl-U), and invisible gold in arsenian sulfides (Cline et al., 2005), other diagnostic characteristics are lacking. These characteristics include the formation in a distal foreland setting; unmetamorphosed ferrous carbonate-rich host rocks; gold deposition associated with decarbonatization and sulfidation of ferroan carbonate rocks; formation at depths of >2 km from moderately acidic fluids; and temporal and spatial association with short-lived magmatism and associated precious ± base metal vein deposits (Hofstra and Cline, 2000; Cline et al., 2005). Instead, the deep-seated metamorphic sources of metals and fluids at Daqiao show common similarities with those of the orogenic gold deposits in the northern domain of the WQO, such as Ma'anqiao and Shuangwang deposits that formed between 1.4 to 3 kbar and 120 to 350 °C (Chen et al., 2004). Overall, gold deposits throughout the WQO share features with orogenic-type gold mineralization, including the association with the convergent plate margins; formation during the prolonged orogenic evolution and related multiple metamorphism and deformation; close proximity to major translithospheric structures; geometry controlled by second and third order splays off regional structures; relatively little apparent host-rock preference; an age that generally postdates the emplacement of granitoids; and a broad range in P-T conditions of ore formation (1 to 5 kbars and 220 to 450 °C; Groves et al., 1998; Bierlein and Crowe, 2000; Goldfarb and Groves, 2015). The difference in mineralization styles and alteration features between Daqiao and the northern mesothermal orogenic gold deposits of the WQO may be explained by different crustal levels of formation and the different characteristics of the host lithologies (Uemoto et al., 2002). The development of multistage hydraulic fracturing of ores combined with alteration characteristics formed by brittle deformation at Daqiao indicate that the hydrothermal alteration and gold mineralization took place at relatively high crustal levels (Ridley et al., 2000), which may be less than 1 km (Xu et al., 2015). Collectively, we conclude that the Daqiao gold deposit belongs to the shallow-crustal epizonal orogenic type formed in association with regional metamorphism and deformation after the Late Triassic collision between the NCC and SCB and subsequent West Qinling orogenesis rather than the Carlin-like type as previously suggested (Mao et al., 2002; Chen et al., 2004).

Conclusions

The Daqiao gold deposit is hosted in the Triassic pumpellyite–actinolite facies metamorphic turbidites in the WQO. Results of LA-ICP-MS trace element analysis, combined with the sulfur isotope data, favor a deep-seated metamorphic source for the ore fluids. The gold, sulfur and other components in the hydrothermal system were most likely originally sourced from the underlying Paleozoic pyritic carbonaceous shales that were subjected to upper greenschist and lower amphibolite facies metamorphism associated with the orogenesis of the WQO.

We demonstrate that there are two main types of gold deposition at Daqiao, with different mechanisms. Early stage mineralization took place in tectonic breccia A beneath low-permeability shale seals that cap the hydrothermal system, where metamorphic fluids reacted with the Triassic turbidites and sedimentary CM therein to form pervasive silicification and disseminated pyrite and marcasite with relatively low gold endowment. In the main-ore stage, continued flow of hydrothermal fluids caused fluid overpressuring and hydrofracturing in the competent silicified clastic rocks and resultant vein formation. The consequent rapid fluid-pressure fluctuations led to phase separation and oxidation of ore fluids, as well as fast precipitation of gold and other trace elements under supersaturated conditions.

Overall, the Daqiao gold deposit belongs to the shallow-crustal epizonal orogenic type and formed in association with regional metamorphism and deformation after the Late Triassic collision between the NCC and SCB and subsequent West Qinling orogenesis.

Acknowledgments

We thank Xiao-Ye Jin, Guang Wen, Zheng-Jie Qiu, Ji-Xiang Sui, and Shi-Da Lu for their help during the LA-ICP-MS analysis of trace elements, Raman analysis, and field investigation. Our thanks extend to the Daqiao Mining Ltd. and Geological Survey of Gansu Province for providing access to sampling and information about the deposit. Research work was financially supported by the National Natural Science Foundation of China (grant 41325007), the GPMR State Key Laboratory (grant MSFGPMR03), the Fundamental Research Funds for the Central Universities, China University of Geosciences in Wuhan (CUGCJ1711), the China Geological Survey (grant 1212011120570), and National Demonstration Center for Experimental Mineral

Exploration Education at China University of Geosciences (Wuhan). We wish to thank editors Larry Meinert and Alistair White, and reviewers Jeff Steadman and Rosaline C Figueiredo e Silva from *Economic Geology*, all of whom provided very detailed and valuable comments that have greatly helped in improving the final version of this manuscript. This is contribution 5 from the Center for Research in Economic Geology and Exploration Targeting (CREGET). Any use of trade, product, or firm names is for descriptive purposes only and does not imply endorsement by the U.S. Government.

REFERENCES

Allen, K.D., and Hahn, G.A., 1994, Geology of the Sunbeam and Grouse Creek gold-silver deposits, Yankee Fork mining district, Eocene Challis volcanic field, Idaho: A volcanic dome- and volcaniclastic-hosted epithermal system: Economic Geology, v. 89, p. 1964–1982.

Barker, S.L.L., Hickey, K.A., Cline, J.S., Dipple, G.M., Kilburn, M.R., Vaughan, J.R., and Longo, A.A., 2009, Uncloaking invisible gold: Use of NanoSIMS to evaluate gold, trace elements, and sulfur isotopes in pyrite from Carlin-type gold deposits: Economic Geology, v. 104, p. 897–904.

Berner, R.A., 1970, Sedimentary pyrite formation: American Journal of Science, v. 268, p. 1–23.

Beyssac, O., Goffé, B., Chopin, C., and Rouzaud, J.N., 2002, Raman spectra of carbonaceous material in metasediments: a new geothermometer: Journal of metamorphic Geology, v. 20, p. 859–871.

Bierlein, F.P., and Crowe, D.E., 2000, Phanerozoic orogenic lode gold deposits: Reviews in Economic Geology, v. 13, p. 103–139.

Butler, I.B., and Rickard, D., 2000, Framboidal pyrite formation via the oxidation of iron (II) monosulfide by hydrogen sulphide: Geochimica et Cosmochimica Acta, v. 64, p. 2665–2672.

Canfield, D.E., and Thamdrup, B., 1994, The production of ^{34}S-depleted sulfide during bacterial disproportionation of elemental sulfur: Science, v. 266, p. 1973–1975.

Canfield, D.E., and Teske, A., 1996, Late Proterozoic rise in atmospheric oxygen concentration inferred from phylogenetic and sulphur-isotope studies: Nature, v. 382, p. 127–32.

Carpenter, R.H., 1974, Pyrrhotite isograd in southeastern Tennessee and southwestern North Carolina: Geological Society of America Bulletin, v. 85, p. 451–456.

Cassidy, K.F., 1992, Archaean granitoid-hosted gold deposits in green schist to amphibolite facies terrains: a high P-T to low P-T depositional continuum equivalent to greenstone-hosted deposits: Unpublished Ph.D. thesis, Perth, Australia, University of Western Australia, 296p.

Chang, Z., Large, R.R., and Maslennikov, V., 2008, Sulfur isotopes in sediment-hosted orogenic gold deposits: Evidence for an early timing and a seawater sulfur source: Geology, v. 36, p. 971–974.

Chen, L., Li, X.H., Li, J.W., Hofstra, A.H., Liu, Y., and Koenig, A.E., 2015, Extreme variation of sulfur isotopic compositions in pyrite from the Qiuling sediment-hosted gold deposit, West Qinling orogen, central China: an in situ SIMS study with implications for the source of sulfur: Mineralium Deposita, v. 50, p. 643–656.

Chen, T.T., 1978, Colloform and framboidal pyrite from the Caribou deposit New Brunswick:

Canadian Mineral, v. 16, p. 9–15.

Chen, Y.J., Zhang, J., Zhang, F.X., Franco, P., and Li, C., 2004, Carlin and Carlin-like gold deposits in the Western Qinling Mountains and their metallogenic time, tectonic setting and model: Geological Review, v. 50, p. 134–152 (in Chinese with English abs.).

Chen, Y.J., and Santosh, M., 2014, Triassic tectonics and mineral systems in the Qinling Orogen, central China: Geological Journal, v. 49, p. 338–358.

Chen, Z.H., Lu, S.N., Li, H.K., Li, H.M., Xiang, Z.Q., Zhou, H.Y., and Song, B., 2006, Constraining the role of the Qinling orogen in the assembly and break-up of Rodinia: Tectonic implications for Neoproterozoic granite occurrences: Journal of Asian Earth Sciences, v. 28, p. 99–115.

Cheshire, M.C., and Bish, D.L., 2012, Mineralogical and sulphur isotopic evidence for the influence of sulphate-reducing and -disproportionating bacteria on pyrite and marcasite formation in the Georgia kaolins: Clay Minerals, v. 47, p. 559–572.

Cline, J.S., and Hofstra, A.A., 2000, Ore-fluid evolution at the Getchell Carlin-type gold deposit, Nevada, USA: European Journal of Mineralogy, v. 12, p. 195–212.

Cline, J.S., Hofstra, A.A., Muntean, J.L., Tosdal, R.M., and Hickey, K.A., 2005, Carlin-Type Gold Deposits in Nevada: Critical Geologic Characteristics and Viable Models: Economic Geology 100th Anniversary Volume, p. 451–484.

Cook, N.J., Ciobanu, C.L., and Mao, J.W., 2009, Textural control on gold distribution in As-free pyrite from the Dongping, Huangtuliang and Hougou gold deposits, North China Craton (Hebei Province, China): Chemical Geology, v. 264, p. 101–121.

Cox, S.F., 1995, Structural and geochemical controls on the development of turbiditc-hosted gold quartz vein deposits, Wattle Gully mine, central Victoria, Australia: Economic Geology, v. 90, p. 1722–1746.

Craw, D., MacKenzie, D.J., Pitcairn, I.K., Teagle, D.A.H., and Norris, R.J., 2007, Geochemical signatures of mesothermal Au-mineralized late-metamorphic deformation zones, Otago Schist, New Zealand: Geochemistry: Exploration, Environment, Analysis, v. 7, p. 225–232.

Craw, D., Upton, P., Yu, B.S., Horton, T., and Chen, Y.G., 2010, Young orogenic gold mineralisation in active collisional mountains, Taiwan: Mineralium Deposita, v. 45, p. 631–646.

Donald, R., and Southam, G., 1999, Low temperature anaerobic bacterial diagenesis of ferrous monosulfide to pyrite: Geochimica et Cosmochimica Acta, v. 63, p. 2019–2023.

Dong, Y.P., Zhang, G.W., Neubauer, F., Liu, X.M., Genser, J., and Hauzenberger, C., 2011, Tectonic evolution of the Qinling orogen, China: Review and synthesis: Journal of Asian Earth Sciences, v. 41, p. 213–237.

Dong, Y.P., Liu, X.M., Neubauer, F., Zhang, G.W., Tao, N., Zhang, Y.G., Zhang, X.N., and Li, W., 2013, Timing of Paleozoic amalgamation between the North China and South China Blocks: Evidence from detrital zircon U-Pb ages: Tectonophysics, v. 586, p. 173–191.

Dong, Y.P., and Santosh, M., 2016, Tectonic architecture and multiple orogeny of the Qinling orogenic belt, central China: Gondwana Research, v. 29, p. 1–40.

Drummond, S.E., and Ohmoto, H., 1985, Chemical evolution and mineral deposition in boiling hydrothermal systems: Economic Geology, v. 80, p. 126–147.

Emsbo, P., Mclaughlin, P.I., Breit, G.N., Bray, E.A.D., and Koenig, A.E., 2015, Rare earth elements in sedimentary phosphate deposits: Solution to the global REE crisis? Gondwana Research, v. 27, p. 776–785.

Evans, K.A., Phillips, G.N., and Powell, R., 2006, Rock-buffering of auriferous fluids in altered rocks associated with the Golden Mile-style mineralization, Kalgoorlie gold field, Western Australia: Economic Geology, v. 101, p. 805–817.

Farrand, M., 1970, Framboidal sulphides precipitated synthetically: Mineralium Deposita, v. 5, p. 237–247.

Ferry, J.M., 1981, Petrology of graphitic sulfide-rich schists from south-central Maine: An example of desulfidation during prograde regional metamorphism: American Mineralogist, v. 66, p. 908−930.

Franchini, M., McFarlane, C., Maydagán, L., Reich, M., Lentz, D.R., Meinert, L., and Bouhier, V., 2015, Trace metals in pyrite and marcasite from the Agua Rica porphyry-high sulfidation epithermal deposit, Catamarca, Argentina: Textural features and metal zoning at the porphyry to epithermal transition: Ore Geology Reviews, v. 66, p. 366−387.

Gansu Geological Survey, 2011, Verification report of reserve resource at Daqiao gold deposit, Xihe County, Gansu Province: Unpublished report, 136p (in Chinese).

Gansu Geological Survey, 2017, Geological and mineral resource survey of the Daqiao-Longfeng area, Xihe County, Gansu Province: Unpublished report, 80p (in Chinese).

Gilbert, S.E., Danyushevsky, L.V., Rodemann, T., Shimizu, N., Gurenko, A., Meffre, S., Thomas, H., Large, R.R., and Death, D., 2014, Optimisation of laser parameters for the analysis of sulphur isotopes in sulphide minerals by laser ablation ICP-MS: Journal of Analytical Atomic Spectrometry, v. 29, p. 1042–1051.

Gilder, S.A., Leloup, P.H., Courtillot, V., Chen, Y., Coe, R.S., Zhao, X.X., Xiao, W.J., Halim, N., Cogne, J.P., and Zhu, R.X., 1999, Tectonic evolution of the Tancheng-Lujiang (Tan-Lu) fault via Middle Triassic to Early Cenozoic paleomagnetic data: Journal of Geophysical Research: Solid Earth, v. 104, p. 15365–15390.

Goldfarb, R.J., Newberry, R.J., Pickthorn, W.J., and Gent, C.A., 1991, Oxygen, hydrogen, and sulfur isotope studies in the Juneau gold belt, southeastern Alaska; constraints on the origin of hydrothermal fluids: Economic geology, v. 86, p. 66–80.

Goldfarb, R.J., Baker, T., Dube, B., Groves, D.I., Hart, C.J.R., and Gosselin, P., 2005, Distribution, character, and genesis of gold deposits in metamorphic terranes: Economic Geology 100th Anniversary Volume, p. 407–450.

Goldfarb, R.J., Hart, C., Davis, G., and Groves, D., 2007, East Asian gold: Deciphering the anomaly of phanerozoic gold in precambrian cratons: Economic Geology, v. 102, p. 341–345.

Goldfarb, R.J., Taylor, R.D., Collins, G.S., Goryachev, N.A., and Orlandini, O.F., 2014, Phanerozoic continental growth and gold metallogeny of Asia: Gondwana Research, v. 25, p. 48–102.

Goldfarb, R.J., and Groves, D.I., 2015, Orogenic gold: common or evolving fluid and metal sources through time: Lithos, v. 233, p. 2–26.

Golding, S.D., Groves, D.I., McNaughton, N.J., Mikuck, E.J., and Sang, J.H., 1990, Source of ore fluid and ore components: sulphur isotope studies, in Ho, S.E., Groves, D.I., and Bennett, J.M., eds, Gold deposits of the Archaean Yilgarn Block, Western Australia: nature, genesis and exploration guides. Geology Department and Extension Services, University of Western Australia Publication 20, p. 259–262.

Gregory, D.D., Large, R.R., Bath, A.B., Steadman, J.A., Wu, S., Danyushevsky, L., and Ireland, T.R., 2016, Trace Element Content of Pyrite from the Kapai Slate, St. Ives Gold District, Western Australia: Economic Geology, v. 111, p. 1297–1320.

Groves, D.I., Goldfarb, R.J., Gebre-Mariam, M., Hagemann, S.G., and Robert, F., 1998, Orogenic gold deposits: A proposed classification in the context of their crustal distribution and relationship to other gold deposit types: Ore Geology Reviews, v. 13, p. 7–27.

Gu, X.X., Zhang, Y.M., Li, B.H., Dong, S.Y., Xue, C.J., and Fu, S.H., 2012, Hydrocarbon- and ore-bearing basinal fluids: a possible link between gold mineralization and hydrocarbon accumulation in the Youjiang basin, South China: Mineralium Deposita, v. 47, p. 663–682.

Habicht, K.S., Canfield, D.E., and Rethmeier, J., 1998, Sulfur isotope fractionation during bacterial reduction and disproportionation of thiosulfate and sulfite: Geochimica et Cosmochimica Acta, v. 62, p. 2585–2595.

Haynes, D.W., Cross, K.C., Bills, R.T., and Reed, M.H., 1995, Olympic Dam ore genesis; a fluid-mixing model: Economic Geology, v. 90, p. 281–307.

He, J.Z., 2008, Geochemical fields of metallic deposits in West Qinling: Unpublished Ph.D. thesis, Wuhan, China, China University of Geosciences (Wuhan), 210 p (in Chinese with English abs.).

Hodkiewicz, P.F., Groves, D.I., Davidson, G.J., Weinberg, R.F., and Hagemann, S.G., 2009, Influence of structural setting on sulphur isotopes in Archean orogenic gold deposits, Eastern Goldfields Province, Yilgarn, Western Australia: Mineralium Deposita, v. 44, p. 129–150.

Hofstra, A.H., and Cline, J.S., 2000, Characteristics and models for Carlin-type gold deposits: Reviews in Economic Geology, v.13, p. 163–220.

Holser, W.T., 1977, Catastrophic chemical events in the history of the ocean: Nature, v. 267, p. 403–408.

Hu, S.Y., Evans, K., Craw, D., Rempel, K., Bourdet, J., Dick, J., and Grice, K., 2015, Raman characterization of carbonaceous material in the Macraes orogenic gold deposit and metasedimentary host rocks, New Zealand: Ore Geology Reviews, v. 70, p. 80–95.

Hu, S.Y., Evans, K., Fisher, L., Rempel, K., Craw, D., Evans, N.J., Cumberland, S., Robert, A., and Grice, K., 2016, Associations between sulfides, carbonaceous material, gold and other trace elements in polyframboids: Implications for the source of orogenic gold deposits, Otago Schist, New Zealand: Geochimica et Cosmochimica Acta, v. 180, p. 197–213.

Hu, S.Y., Evans, K., Craw, D., Rempel, K., and Grice, K., 2017, Resolving the role of carbonaceous material in gold precipitation in metasediment-hosted orogenic gold deposits: Geology, v. 45, p. 167–170.

Kajiwara, Y., and Krouse, H.R., 1971, Sulfur isotope partitioning in metallic sulfide systems: Canadian Journal of Earth Sciences, v. 8, p. 1397–1408.

Kerrich, R., Goldfarb, R., Groves, D., Garwin, S., and Jia, Y.F., 2000, The characteristics, origins, and geodynamic settings of supergiant gold metallogenic provinces: Science in China Series D: Earth Sciences, v. 43, p. 1−68.

Kesler, S.E., Fortuna, J., Ye, Z.J., Alt, J.C., Core, D.P., Zohar, P., Borhauer, J., and Chryssoulis, S.L., 2003, Evaluation of the role of sulfidation in deposition of gold, Screamer section of the Betze-Post Carlin-type deposit, Nevada: Economic Geology, v. 98, p. 1137–1157.

Koenig, A.E., Rogers, R.R., and Trueman, C.N., 2009, Visualizing fossilization using laser ablation ICP-MS maps of trace elements in Late Cretaceous bones: Geology, v. 37, p. 511–514.

Kříbek, B., Sýkorová, I., Machovič, V., Knésl, I., Laufek, F., and Zachariáš, J., 2015, The origin and hydrothermal mobilization of carbonaceous matter associated with Paleoproterozoic orogenic-type gold deposits of West Africa: Precambrian Research, v. 270, p. 300–317.

Large, R.R., Maslennikon, V.V., Robert, F., Danyushevsky, L.V., and Chang, Z.S., 2007, Multistage sedimentary and metamorphic origin of pyrite and gold in the giant Sukhoi Log deposit, Lena gold province, Russia: Economic Geology, v. 102, p. 1233–1267.

Large, R.R., Danyushevsky, L., Hollit, C., Maslennikov, V., Meffre, S., Gilbert, S., Bull, S., Scott, R., Embsbo, P., Thomas, H., Singh, B., and Foster, J., 2009, Gold and trace element zonation in pyrite using a laser imaging technique: Implications for the timing of gold in orogenic and Carlinstyle sediment-hosted deposits: Economic Geology, v. 104, p. 635–668.

Large, R.R., Bull, S.W., and Maslennikov, V.V., 2011, A Carbonaceous Sedimentary Source-Rock Model for Carlin-Type and Orogenic Gold Deposits: Economic Geology, v. 106, p. 331–358.

Large, R.R., Halpin, J.A., Danyushevsky, L.V., Maslennikov, V.V., Bull, S.W., Long, J.A., Gregory, D.D., Lounejeva, E., Lyons, T.W., Sack, P.J., McGoldrick, P.J., and Calver, C.R., 2014, Trace element content of sedimentary pyrite as a new proxy for deep-time ocean–atmosphere evolution: Earth and Planetary Science Letters, v. 389, p. 209–220.

Li, J., Chen, Y.J., Mao, S.D., Qin, Y., Guo, J.H., and Nan, Z.L., 2008, The C-H-O isotope systematic of the Yangshan gold deposit, Gansu and its implication for the ore-fluid orogin: Acta Petrologica Sinca, v. 24, p. 817–826 (in Chinese with English abs.).

Li, N., Yang, L.Q., Zhang, C., Zhang, J., Lei, S.B., Wang, H.T., and Gao, X., 2012, Sulfur isotope characteristics of the Yangshan gold belt, West Qinling: constraints on ore-forming environment and material source: Acta Petrologica Sinica, v. 28, p. 1577–1587 (in Chinese with English abs.).

Li, N., Deng, J., Yang, L.Q., Goldfarb, R.J., Zhang, C., Marsh, E., Lei, S.B., Koeing, A.E., and Lowers, H., 2014, Paragenesis and geochemistry of ore minerals in the epizonal gold deposits of the Yangshan gold belt, West Qinling, China: Mineralium Deposita: v. 49, p. 427–449.

Li, Z.P., and Peters, S.G., 1998, Comparative geology and geochemistry of sedimentary rock-hosted (Carlin-type) gold deposits in the People's Republic of China and in Nevada, USA: US Geological Survey Open-File Report 98–466 (version 1.1 on CD-ROM or World Wide Web at URL http://geopubs.wr.usgs.gov/open-file/of98-466/).

Liu, J.J., and Zheng, M.H., 1993, La'erma Se-Cu-U-Ni-Mo-PGE-Au deposit of submarine exhalative genesis in La'erma: Journal of Precious Metallic Geology, v. 2, p. 100–103 (in Chinese with English abs.).

Liu, J.J., Zheng, M.H., Liu, J.M., and Zhou, D.A., 2000, Sulfur isotopic composition and geological significance of the Cambrian gold deposits in western Qinling, China: Journal of Changchun University of Science and Technology, v. 30, p. 150–156 (in Chinese with English abs.).

Liu, J.J., Dai, H.Z., Zhai, D.G., Wang, J.P., Wang, Y.H., Yang, L.B., Mao, G.J., Liu, X.H., Liao, Y.F., Yu, C., and Li, Q.Z., 2015, Geological and geochemical characteristics and formation mechanisms of the Zhaishang Carlin-like type gold deposit, western Qinling Mountains, China: Ore Geology Reviews, v. 64, p. 273–298.

Liu, Y.G., Lv, X.B., Zhang, Z.J., You, G.J., and Cao, X.F., 2011, Genesis of Daqiao gold deposit in Xihe County, Gansu Province: Mineral Deposits, v, 6, p. 1085–1099 (in Chinese with English abs.).

Longerich, H.P., Jackson, S.E., and Günther, D., 1996. Laser ablation inductively coupled plasma mass spectrometric transient signal data acqusition and analyte concentration calculation: Journal of Analytical Atomic Spectroscopy, v. 11, p. 899–904.

Loucks, R.R., and Mavrogenes, J.A., 1999, Gold solubility in supercritical hydrothermal brines measured in synthetic fluid inclusions: Science, v. 284, p. 2159–2163.

Love, L.G., 1971, Early diagenetic polyframboidal pyrite, primary and redeposited, from the Wenlockian Denbigh Grit Group, Conway, North Wales, UK: Journal of Sedimentary Research, v. 41, p. 1038–1044.

Love, L.G., Al-Kaisy, A.T., and Brockley, H., 1984, Mineral and organic material in matrices and coatings of framboidal pyrite from Pennsylvanian sediments: Journal of Sedimentary Petrology, v. 54, p. 869–876.

Lu, Y.M., Li, H.G., Chen, Y.G., and Zhang, G.L., 2006, ^{40}Ar/^{39}Ar dating of alteration minerals from Zhaishang gold deposit in Minxian County, Gansu Province, and its geological significance: Mineral Deposits, v. 25, p. 590–597 (in Chinese with English abs.).

Luo, X.M., Qi, J.Z., Yuan, S.S., and Li, Z.H., 2004, Geological and mincroelement geochemical study of Yangshan gold deposit, Gansu province: Geoscience, v. 18, p. 203–209 (in Chinese with English abs.).

Luque, F.J., Ortega, L., Barrenechea, J.F., Millward, D., Beyssac, O., and Huizenga, J., 2009, Deposition of highly crystalline graphite from moderate-temperature fluids: Geology, v. 37, p. 275–278.

Mao, J.W., Qiu, Y.M., Goldfarb, R.J., Zhang, Z.C., Garwin, S., and Fengshou, R., 2002, Geology, distribution, and classification of gold deposits in the western Qinling belt, central China: Mineralium Deposita, v. 37, p. 352–377.

Mattauer, M., Matte, P., Malavieille, J., Tapponnier, P., Maluski, H., Qin, X.Z., Lun, L.Y., and Qin, T. Y., 1985, Tectonics of Qinling Belt: Build-up and evolution of Eastern Asia: Nature, v. 317, p. 496–500.

McCuaig, T.C., and Kerrich, R., 1998, P—T—t—deformation—fluid characteristics of lode gold deposits: evidence from alteration systematics: Ore Geology Reviews, v. 12, p. 381–453.

Mckeag, S.A., Craw, D., and Norris, R.J., 1989, Origin and deposition of a graphitic schist-hosted metamorphogenic Au-W deposit, Macraes, East Otago, New Zealand: Mineralium Deposita, v. 24, p. 124–131.

Meng, Q.R., and Zhang, G.W., 1999, Timing of collision of the North and South China blocks: Controversy and reconciliation: Geology, v. 27, p. 123–126.

Meng, Q.R., Qu, H.J., and Hu, J.M., 2007, Deep-water sedimentary environment in the West Qinling and Songpan-Ganzi terrane: Science in China Series D: Earth Sciences, v. 37, p. 209–223 (in Chinese with English abs.).

Müller W., Shelley M., Miller P., and Broudec, S., 2009, Initial performance metrics of a new custom-designed ArF excimer LA-ICPMS system coupled to a two-volume laser-ablation cell: Journal of Analytical Atomic Spectrometry, v. 24, p. 209–214.

Muramoto, J.A., Honjo, S., Fry, B., Hay, B.J., Howarth, R.W., and Cisne, J.L., 1991, Sulfur, iron and organic carbon fluxes in the Black Sea: sulfur isotopic evidence for origin of sulfur fluxes: Deep-Sea Research, v. 38, p. S1151–S1187.

Murowchick, J.B., and Barnes, H.L., 1986, Marcasite precipitation from hydrothermal solutions: Geochimica et Cosmochimica Acta, v. 50, p. 2615–2629.

Murowchick, J.B., and Barnes, H.L., 1987, Effects of temperature and degree of supersaturation on pyrite morphology: American Mineralogist, v. 72, p. 1241–1250.

Ohfuji, H., and Rickard, D., 2005, Experimental syntheses of framboids—a review: Earth-Science Reviews, v. 71, p. 147–170.

Ohmoto, H., 1972, Systematics of sulfur and carbon isotopes in hydrothermal ore deposits: Economic Geology, v. 67, p. 551–578.

Ohmoto, H., Rye, R.O., 1979, Isotopes of sulfur and carbon, in Barnes, H.L., ed., Geochemistry of hydrothermal ore deposits: New York, Wiley, p. 509–567.

Ohmoto, H., and Goldhaber, M.B., 1997, Sulfur and carbon isotopes, in Barnes, H.L., ed., Geochemistry of hydrothermal ore deposits, 3rd ed.: New York, Wiley, p. 517–611.

Palin, J.M., and Xu, Y., 2000, Gilt by association? Origins of pyritic gold ores in the Victory mesothermal gold deposit, Western Australia: Economic Geology, v. 95, p. 1627–1634.

Phillips, G.N., Groves, D.I., and Martyn, J.E., 1984, An epigenetic origin for Archean banded iron-formation-hosted gold deposits: Economic Geology, v. 79, p. 162–171.

Phillips, G.N., Groves, D.I., Neall, F.B., Donnelly, T.H., and Lambert, I.B., 1986, Anomalous sulfur isotope compositions in the Golden Mile, Kalgoorlie: Economic Geology, v. 81, p. 2008–2015.

Phillips, G.N., and Powell, R., 2010, Formation of gold deposits: A metamorphic devolatilization model: Journal of Metamorphic Geology, v. 28, p. 689–718.

Phillips, W.J., 1972, Hydraulic fracturing and mineralization: Journal of the Geological Society, v. 128, p. 337–359.

Pitcairn, I.K., Teagle, D.A.H., Craw, D., Olivo, G.R., Kerrich, R., and Brewer, T.S., 2006, Sources of metals and fluids in orogenic gold deposits: Insights from the Otago and Alpine schists, New Zealand: Economic Geology, v. 101, p. 1525–1546.

Pitcairn, I.K., Craw, D., and Teagle, D.A., 2015, Metabasalts as sources of metals in orogenic gold deposits: Mineralium Deposita, v. 50, p. 373–390.

Powell, R., Will, T.M., and Phillips, G.N., 1991, Metamorphism in Archaean greenstone belts: calculated fluid compositions and implications for gold mineralization: Journal of Metamorphic Geology, v. 9, p. 141–50.

Prendergast, K., Clarke, G.W., Pearson, N.J., and Harris, K., 2005, Genesis of pyrite-Au-As-Zn-Bi-Te zones associated with Cu-Au skarns: evidence from the Big Gossan and Wanagon gold deposits, Ertsberg district, Papua, Indonesia: Economic Geology, v. 100, p. 1021–1050.

Price, B.J., 1972, Minor elements in pyrites from the Smithers map area, British Columbia and exploration applications of minor element studies: Unpublished M.Sc. thesis, British Columbia, Canada, The University of British Columbia, 270p.

Qi, J.Z., Yuan, S.S., Li, L., Sun, B., Guo, J.H., Li, Z.H., Fan, Y.X., Liu, W., and Gao, Q.B., 2003a, Geological features and ore-controlling factors of the Yangshan superlarge gold deposit, Gansu province, China: Geological Review, v. 49, p. 85–92 (in Chinese with English abs.).

Qi, J.Z., Yuan, S.S., Li, L., Fan, Y.X., Liu, W., Gao, Q.B., Sun, B., Guo, J.H., and Li, Z.H., 2003b, Geological and geochemical studies of Yangshan gold deposit, Gansu Province: Mineral Deposits, v. 49, p. 24–31 (in Chinese with English abs.).

Qi, J.Z., Yang, G.C., Li, L., Fan, Y.X., and Liu, W., 2006, Isotope geochemistry, chronology and genesis of the Yangshan gold deposit, Gansu. Geology in China v. 33, p. 1345–1353 (in Chinese with English abs.).

Rahl, J.M., Anderson, K.M., Brandon, M.T., and Fassoulas, C., 2005, Raman spectroscopic carbonaceous material thermometry of low-grade metamorphic rocks: calibration and application to tectonic exhumation in Crete, Greece: Earth and Planetary Science Letters, v. 240, p. 339–354.

Reich, M., Kesler, S.E., Utsunomiya, S., Palenik, C.S., Chryssoulis, S.L., and Ewing, R.C., 2005, Solubility of gold in arsenian pyrite: Geochimica et Cosmochimica Acta, v. 69, p. 2781–2796.

Ridley, J.R., and Diamond, L.W., 2000. Fluid chemistry of orogenic lode gold deposits and implications for genetic models. In: Hagemann, S.G., Brown, P.E. (Eds.), Gold in 2000: Reviews in Economic Geology, v. 13, p. 141–162.

Ridley, J.R., Groves, D.I., and Knight, J.T., 2000, Gold deposits in amphibolites and granulite facies terranes of the Archean Yilgarn craton, Western Australia: Evidence and implications for synmetamorphic mineralization: Reviews in Economic Geology, v. 11, p. 265–290.

Roedder, E., 1968, The non-colloidal origin of “colloform” textures in sphalerite ores: Economic Geology, v. 63, p. 451–471.

Rimmer, S.M., 2004, Geochemical paleoredox indicators in Devonian-Mississippian black shales, Central Appalachian basin, USA: Chemical Geology, v. 206, p. 372–391.

Sadezky, A., Muckenhuber, H., Grothe, H., Niessner, R., and Pöschl, U., 2005, Raman microspectroscopy of soot and related carbonaceous materials: Spectral analysis and structural information: Carbon, v. 43, p. 1731–1742.

Scott, R.J., Meffre, S., Woodhead, J., Gilbert, S.E., Berry, R.F., and Emsbo, P., 2009, Development of framboidal pyrite during diagenesis, low-grade regional metamorphism, and hydrothermal alteration: Economic Geology, v. 104, p. 1143–68.

Seal, R.R., 2006, Sulfur isotope geochemistry of sulfide minerals: Reviews in mineralogy and geochemistry, v. 61, p. 633–677.

Sforna, M.C., Zuilen, M.A.V., and Philippot, P., 2014, Structural characterization by Raman hyperspectral mapping of organic carbon in the 3.46 billion-year-old Apex chert, Western Australia: Geochimica et Cosmochimica Acta, v. 124, p. 18–33.

Sibson, R.H., 1986, Brecciation processes in fault zones: inferences from earthquake rupturing: Pure and Applied Geophysics, v. 124, p. 159–175.

Steadman, J.A., Large, R.R., Meffre, S., Olin, P.H., Danyushevsky, L.V., Gregory, D.D., Belousov, I., Lounejeva, E., Ireland, T.R., and Holden, P., 2015, Synsedimentary to early diagenetic gold in black shale-hosted pyrite nodules at the Golden Mile Deposit, Kalgoorlie, Western Australia: Economic Geology, v. 110, p. 1157–91.

Sui, J.X., Li, J.W., Wen, G., and Jin, X.Y., 2017, The Dewulu reduced Au-Cu skarn deposit in the Xiahe-Hezuo district, West Qinling orogen, China: Implications for an intrusion-related gold system: Ore Geology Reviews, v. 80, p. 1230–1244.

Sun, W.D., Li, S.G., Chen, Y.D., and Li, Y.J., 2002, Timing of synorogenic granitoids in the South Qinling, central China: Constraints on the evolution of the Qinling-Dabie orogenic belt: Journal of Geology, v. 110, p. 457–468.

Sung Y.H., Brugger J., Ciobanu C.L., Pring, A., Skinner, W., and Nugus, M., 2009, Invisible gold in arsenian pyrite and arsenopyrite from a multistage Archaean gold deposit: Sunrise Dam, Eastern Goldfields Province, Western Australia: Mineralium Deposita, v. 44, p. 765–791.

Tan, G. Y., 1992, Geological character of Pingding As-Au deposit and its metallogenic mechanism: Acta Geologica Gansu, v. 1, p. 48–54 (in Chinese with English abs.).

Tan, L.Q., 1996, Lead isotope geochemistry of the Anjiacha gold deposit, Gansu province: Mineral Deposits, v. 15, p. 144–155 (in Chinese with English abs.).

Thomas, H.V., Large, R.E., Bull, S.W., Maslennikov, V., Berry, R.F., Fraser, R., Froud, S., and Moye, R., 2011, Pyrite and Pyrrhotite Textures and Composition in Sediments, Laminated Quartz Veins, and Reefs at Bendigo Gold Mine, Australia: Insights for Ore Genesis: Economic Geology, v. 106, p. 1–31.

Tomkins, A.G., 2010, Windows of metamorphic sulfur liberation in the crust: Implications for gold deposit genesis: Geochimica et Cosmochimica Acta, v. 74, p. 3246–3259.

Tomkins, A.G., 2013a, On the source of orogenic gold: Geology, v. 41, p. 1255–1256.

Tomkins, A.G., 2013b, A biogeochemical influence on the secular distribution of orogenic gold: Economic Geology, v. 108, p. 193–197

Uemoto, T., Ridley, J., Mikucki, E., and Groves, D.I., 2002, Fluid Chemical Evolution as a Factor in Controlling the Distribution of Gold at the Archean Golden Crown Lode Gold Deposit, Murchison Province, Western Australia: Economic Geology, v. 97, p. 1227–1248.

Vielreicher R.M, Vielreicher N.M, Hagemann S.G, and Jones, G., 2003, Fault zone evolution and its controls on ore-grade distribution at the Jianchaling gold deposit, western Qinling region, central China: Mineralium Deposita, v. 38, p. 538–554.

Wilkin, R.T., Barnes, H.L., and Brantley, S.L., 1996, The size distribution of framboidal pyrite in modern sediments: an indicator of redox conditions: Geochimica et Cosmochimica Acta, v. 60, p. 3897–3912.

Wilkin, R.T., and Barnes, H.L., 1997, Formation processes of framboidal pyrite: Geochimica et Cosmochimica Acta, v. 61, p. 323–339.

Wilson, C.J.L., Schaubs, P., and Leader, L.D., 2013, Mineral precipitation in the quartz reefs of the Bendigo gold deposit, Victoria, Australia: Economic Geology and the Bulletin of the Society of Economic Geologists, v. 108, p. 259–278.

Wilson, S.A., Ridley, W.I. and Koenig, A.E., 2002, Development of sulfide calibration standards for the laser ablation inductively coupled plasma mass spectrometry technique: Journal of Analytical Atomic Spectroscopy, v. 17, p. 406–409.

Witt, W.K., 1995, Phase separation (boiling) as a mechanism for deposition of gold in low-iron host rocks, Yarri mining district, Eastern Goldfields Province, in, Nowak, I.R., ed., Geological Survey of Western Australia Annual Review 1995–96, p 149–155.

Wong, K.H., Zhou, M.F., Chen, W.T., O'Brien, H., Lahaye, Y., and Chan, S.L.J., 2017, Constraints of fluid inclusions and in-situ S-Pb isotopic compositions on the origin of the North Kostobe sediment-hosted gold deposit, eastern Kazakhstan: Ore Geology Reviews, v. 81, p. 256-269.

Xu, L., Wu, B.X., Wang, Y.L., Wang, Z.X., Wang, G., and Sun, Z.P., 2015, Fluid inclusion characteristics and geological significance at Daqiao gold deposit: Journal of Jinlin University (Earth Science Edition), v. 45, p. 568–569 (in Chinese with English abs.).

Yang, L.Y., 2014, Geochemistry of ore-forming processes in the Yangshan gold belt, West Qinling, central China: Unpublished Ph.D. thesis, Beijing, China, China University of Geosciences (Beijing), 101p (in Chinese with English abs.).

Yang, L.Q., Deng, J., Li, N., Zhang, C., Ji, X.Z., and Yu, J.Y., 2016, Isotopic characteristics of gold deposits in the Yangshan Gold Belt, West Qinling, central China: Implications for fluid and metal sources and ore genesis: Journal of Geochemical Exploration, v, 168, p. 103–118.

Yang, R.S., 2006, Geology, Geochemistry and Genesis of Yangshan Gold Deposit, Gansu Province: Unpublished Ph.D. thesis, Beijing, China, Peking University, 173p (in Chinese with English abs.).

You, G.J., and Zhang, Z.P., 2009, Geological characteristics of Daqiao gold deposit in Gansu province and its significance in prospecting for gold deposit: Gansu Geology, v. 18, p. 1–8 (in Chinese with English abs.).

Yue, S.W., Deng, X.H., Bagas, L., Lin, Z.W., Fang, J., Zhu, C.H., and Zhang, W., 2017, Fluid inclusion geochemistry and $^{40}Ar/^{39}Ar$ geochronology constraints on the genesis of the Jianchaling Au deposit, China: Ore Geology Reviews, v. 80, p. 676–690.

Zeng, Q.T., McCuaig, T.C., Hart, C.J.R., Jourdan, F., Muhling, J., and Bagas, L., 2012, Structural and geochronological studies on the Liba goldfield of the West Qinling Orogen, Central China: Mineralium Deposita, v. 47, p. 799–819.

Zeng, Q.T., Evans, N.J., McInnes, B.I., Batt, G.E., McCuaig, C.T., Bagas, L., and Tohver, E., 2013, Geological and thermochronological studies of the Dashui gold deposit, West Qinling Orogen, Central China: Mineralium Deposita, v. 48, p. 397–412.

Zeng, Q.T., Mccuaig, T.C., Tohver, E., Bagas, L., and Lu, Y.J., 2014, Episodic Triassic magmatism in the western South Qinling Orogen, central China, and its implications: Geological Journal, v. 49, p. 402–423.

Zhang, F.X., Chen, Y.J., Li, C., Zhang, J., Ma, J.Q., and Li, X., 2000, Features of geologic-geochemistry of Jinlongshan-Qiuling gold deposit and its genesis in Qinling belt: Dynamics on mineralizing process of Carlin type gold deposits of Qinling type: Science in China Series D: Earth Sciences, v. 30 (Suppl.), p. 73–81 (in Chinese with English abs.).

Zhang, F.X., Ji, J.L., Long, L.L., and Fan, C.H., 2001, Comparative features of Carlin-Para-Carlin type gold deposits in the South Qinling and gold deposits in other areas: Geological Review, v. 47, p. 492–499 (in Chinese with English abs.).

Zhang, F.X., Wang, L.S., and Hou, J.F., 2009, Black rock series, types of ore deposits and ore-forming systems in Qinling orogenic belt: Geology in China, v. 36, p. 694–704 (in Chinese with English abs.).

Zhang, G.W., Zhang, Z.Q., and Dong, Y.P., 1995, Nature of main tectono-lithostratigraphic units of the Qinling Orogen: implications for the tectonic evolution: Acta Petrologica Sinica, v. 11, p. 101–114 (in Chinese with English abs.).

Zhang, G.W., Meng, Q.G., Yu, Z.P., Sun, Y., Zhou, D.W., and Guo, A.L., 1996, Orogenesis and dynamics of the Qinling orogen: Science in China Series D: Earth Sciences (English Edition), v. 39, p. 225–234.

Zhang, G.W., Zhang, B.R., Yuan, X.C., and Xiao, Q.H., 2001, Qinling orogenic belt and continental dynamics: Beijing, Science Press, 855p (in Chinese).

Zhang, L., Yang, R.S., Mao, S.D., Lu, Y.H., Qin, Y., and Liu. H.J., 2009, Sr and Pb isotopic feature and ore-forming material source of the Yangshan gold deposit: Acta Petrologica Sinica: v. 25, p. 2811–2822 (in Chinese with English abs.).

Zhang, Z. A., 1993, Mineralization mechanism of La'erma gold deposit: Journal of Mineralogy and Petrology, v. 13, p. 60–67 (in Chinese with English abs.).

Zhang Q., Y, X.M., Yin, Y., Jin, W.J., Wang, Y.L., and Zhao, Y.Q., 2009, Issues on metallogenesis and prospecting of gold and copper deposits related to adakite and Himalayan type granite in west Qinling: Acta Petrologica Sinica, v. 12, p. 3103–3122 (in Chinese with English abs.).

Zhao, J.H., Zhou, M.F., Yan, D.P., Zheng, J.P., and Li, J.W., 2011, Reappraisal of the ages of Neoproterozoic strata in South China: no connection with the Grenvillian orogeny: Geology, v. 39, p. 299–302.

Zhao, X.X., Coe, R.S., Chang, K.H., Park, S.O., Omarzai, S.K., Zhu, R.X., Zhou, Y.X., Gilder, S., and Zheng, Z., 1999, Clockwise rotations recorded in Early Cretaceous rocks of South Korea: implications for tectonic affinity between the Korean Peninsula and North China: Geophysical Journal International, v. 139, p. 447–463.

Zhou, D., and Graham, S.A., 1996, Songpan-Ganzi complex of the west Qilian Shan as a Triassic remnant ocean basin, in, Yin A., Harrison M., ed., The tectonic evolution of Asia: Cambridge, Cambridge University Press, p. 281–299.

Zhou, T.H., Goldfarb, R.J., and Phillips, N.G., 2002, Tectonics and distribution of gold deposits in China – an overview: Mineralium Deposita, v. 37, p. 249–282.

Zhou, Z.J., Lin, Z.W., and Qin, Y., 2014, Geology, geochemistry and genesis of the Huachanggou gold

deposit, western Qinling orogen, central China: Geological Journal, v. 49, p. 424–441.
Zhu, R.X., Yang, Z.Y., Wu, H.N., Ma, X.H., Huang, B.C., Meng, Z.F., and Fang, D.J., 1998, Paleomagnetic constraints on the tectonic history of the major blocks of China during the Phanerozoic: Science in China Series D: Earth Sciences (English Edition), v. 41, p. 1–19.
Zoheir, B.A., El-Shazly, A.K., Helba, H., Khalil, K.I., and Bodnar, R.J., 2008, Origin and evolution of the Um Egat and Dungash orogenic gold deposits, Egyptian Eastern Desert: Evidence from fluid inclusions in quartz: Economic Geology, v. 103, p. 405–424.

Figure and table captions

Fig. 1. A. A simplified map showing tectonic division of the Qinling Orogen. Also shown are the major faults, gold deposits and the location of Daqiao (modified from Liu et al., 2015). The insert indicates the location of the west Qinling Orogen in China. B. Geology of the Daqiao gold deposit and surrounding areas.

Fig. 2. A. Geological map of the Daqiao gold deposit (modified from You and Zhang, 2009). B. Stratigraphic column of Middle to Upper Carboniferous to Middle Triassic strata of the study area (Gansu Geological Survey, 2011).

Fig. 3. Representative cross sections along exploration line 79 (A-A') and line 39 (B-B') showing the occurrence and morphology of the major orebodies at the Daqiao gold deposit (The reader is facing NE). The locations of the sections are indicated in Figure 2.

Fig. 4. Photographs showing occurrences and structures of orebodies at Daqiao. A. Conformable contact between the limestone of Middle and Upper Carboniferous Minhe Formation and breccia ores hosted in Middle Triassic Huashiguan Formation. B. Multistage breccias cemented by calcite-chalcedony-sulfides, constituting intensively silicified hydraulic breccia C. C. Typical tectonic breccia A consisting of angular fragments of siltstone, slate and limestone, which were overprinted by hydrothermal ore fluids. D. Two stages of hydraulic fracturing. Black silicified siltstone (breccia A) was surrounded by the hydrothermal quartz constituting breccia B, which were in turn cemented by the calcite-chalcedony-sulfides matrix forming breccia C. Abbreviations: Cal = Chalcedony, Cc = calcite, Mc = marcasite, Py =

pyrite.

Fig. 5. Photographs of hand specimens showing the mineralization and ore textures of the Daqiao gold deposit. A, B. Pre-ore S1 syngenetic or diagenetic pyrite in the sedimentary rocks occurring as strongly deformed layers originally aligned parallel to bedding or nodular aggregates associated with the development of quartz pressure shadows. C. Early-ore S2 quartz-sulfide veinlets averaging 1–3 cm in thickness in the altered calcareous slates. D. Breccia A cemented by quartz and sulfides and then crosscut by calcite-chalcedony-sulfides veinlets forming main-ore S3 high grade ore (12 g/t). E. Extremely fine-grained sulfides in the cements of the breccia C in S3. F, G. Typical textures of multistage hydraulic brecciation: microcrystalline quartz-sulfides cement black silicified breccia A forming breccia B and then filled with calcite-chalcedony-sulfides matrix (breccia C). H. The late-ore stage S4 coarse-grained marcasite-bearing calcite veins in the weakly altered pelitic slate. Abbreviations: Qz = quartz. See above for abbreviations of other minerals.

Fig. 6. Photomicrographs (A, C, reflected light) and SEM images (B, D) showing the close relationship between the sulfides and carbonaceous materials (CM) at Daiqao. A. CM disseminations intergrown with irregular pyrite. B. CM enveloped by irregular porous py4 aggregates with some relics of clear py3. C, D. Sooty aggregates of fine-grained pyrite and euhedral marcasite intimately related to CM of 10 to 200 μm diameter.

Fig. 7. Photographs (A), reflected-light (B-D), EBSD (E), and transmitted plan-polarized light photomicrographs (F) showing the ore-related hydrothermal alteration assemblages at Daqiao. A. Massive microcrystalline quartz in silicified ores overprinted by comb and drusy quartz. B. Silicified breccia B with disseminated sulfides is cemented by late calcite-chalcedony-pyrite-stibnite. C. Breccia B with fine-grained disseminated sulfides is cemented by later calcite-chalcedony-colloform pyrite matrix. D. Strongly anisotropic marcasite with yellowish-brown to grayish-blue polarization colors co-exists with isotropic pyrite. E. EBSD phase image showing the intergrowth between marcasite and pyrite in ore samples. F. Sericitic alteration closely

intergrown with sulfides in the ores. Abbreviations: Ser = sericite, Stb = stibnite. See above for abbreviations of other minerals.

Fig. 8. Reflected-light photomicrographs (A, B) and SEM images (A, C, D) showing textural features of py1, py2 and mc1. Also shown in (C) and (D) are representative spot analyses of sulfur isotope and trace element results of selected sulfide grains. A. Py1 framboids intergrown with PGE minerals in carbonaceous shale of the Middle Triassic Huashiguan Formation. B. Porous py1 is overgrown by py2, and later mc1 overgrows on the exterior of py2. C. Coarse-grained euhedral py2 overgrows the sooty porous py1 aggregate, which contains fine-grained native platinum. D. Porous Py1 with galena inclusions is enveloped by euhedral py2 and in turn overgrown by mc1. Abbreviations: Gn = galena, Pt = platinum, PGE = platinum group elements. See above for abbreviations of other minerals.

Fig. 9. SEM images (A-D) and reflected-light photomicrograph (E, F) illustrating the textures of py3 and py4, with sulfur isotope and trace element data of representative sulfide grains for those two generations of sulfides. A. High As-Au euhedral py3 overgrows a porous core of py2, and is enveloped by inclusion-rich py4. B, C. Relics of inclusion-free py3 are surrounded by porous py4 with apatite and silicate inclusions; note that py4 generally has lower As-Au than py3. D. Py4 intergrown with minor chalcopyrite and hematite in a calcite vein. E. F. Inclusion-free py3 crystal has been eroded and reprecipitated porous py4, which was surrounded by later mc2 and mc3 aggregates. Abbreviations: Ap = apatite, Ccp = chalcopyrite, Hem = hematite. See above for abbreviations of other minerals.

Fig. 10. Reflected-light photomicrographs (A) and SEM images (A-D) highlighting the texture, sulfur isotopes and trace element compositions of the zoned mc3 in the coarse-grained mc2. A. Strongly anisotropic marcasite grain showing irregular cyclic zoning rim of cloudy mc3, which has a lower $\delta^{34}S$ value but much higher As-Au than inner mc2. B. Close-up of mc3 veinlets crosscutting the mc2 euhedra. C. Narrow mc3 ring with minor extremely fine-grained arsenopyrite inside or in the outmost rim of the coarse-grained patchy mc2 aggregate. Close-up of the intergrowth of Pt with mc2

from the same sample. D. Porous py4 relic is overgrown by mc2 consisting of mc3 rims and associated arsenopyrite grains. Abbreviations: Apy = arsenopyrite. See above for abbreviations of the minerals.

Fig. 11. SEM images showing the textures, sulfur isotopes and trace element compositions of py5a, py5b, py6, and mc4. A. Zoned py5a microcrystals containing high As-Au in silicified breccia B, with a diagnostic negative $\delta^{34}S$ value. B. Clusters of framboidal py5a exhibiting by spherical to ovoid aggregates overgrow euhedral py3. C. Early generations of sulfides including py4, mc2, and mc3 are crosscut by a py5b vein. D. Colloform py5b intergrown with unnamed uranium oxides, showing high As-Au concentrations and a negative $\delta^{34}S$ value. E. Porous mc2 with narrow zone of mc3 is overgrown by inclusion-free mc4. F. Rare extremely fine-grained barites coexisting with py6 in the breccia ores. Abbreviations: Brt = barite. See above for abbreviations of other minerals.

Fig. 12. Paragenetic sequence of Daqiao gold mineralization interpreted from textures and sulfide geochemistry.

Fig. 13. Range and mean trace element contents for the different pyrite and marcasite generations hosted in sediments at Daqiao. A. Per-ore stage S1 py1. B. Early-ore stage S2 py2. C. Early-ore stage S2 py3 and py4. D. Early-ore stage S2 mc1 and mc2. E. Main-ore stage S3 py5a, py5b, and mc3. F. Late-ore stage S4 py6 and mc4.

Fig. 14. LA-ICP-MS spot analyses on pyrite and marcasite. A. Au-As: almost all the pyrite and marcasite types show a positive relationship of Au-As, except some py3 and py5 spots, which have relative high As but low Au. All the data spots are below the gold solubility line in pyrite (Reich et al., 2005). B. General trend of increasing Au and Ag from py1 to py5 and mc2 to mc3, all data having Au/Ag<1 except some mc3 and py3.

Fig. 15. LA-ICP-MS spot analyses on pyrite and marcasite. A. Au-Sb: Py5 and mc3 have significantly higher Au and Sb than other sulfide types. B. Au-Tl: Pyrite forms a broad field compared to marcasite spreading over a wide Au and Tl range but with a

relatively consistent Au/Tl ratio. C. Au-W: General trends of increasing Au and W for pyrite and marcasite types. D. Au-Pb: Diagenetic py1 has relative high Pb, and the Pb of hydrothermal pyrite and marcasite forms a broad field, showing no correlation with Au.

Fig. 16. LA-ICP-MS spot analyses on pyrite and marcasite. A. Bi-Pb: Compared to all the hydrothermal pyrite and marcasite, diagenetic py1 displays the highest Bi and Pb values. B. Tl-Hg: All types of sulfides show a broad field but with a highly consistent Tl/Hg ratio; note that py5a, py5b and mc3 have the highest Tl and Hg values. C. Zn-Cu: General positive correlation between Zn and Cu. D. Ni-Co: Most data plots well above the Co/Ni = 1 line with positive correlation except for a few py2 and py3 spots.

Fig. 17. Trace element LA-ICP-MS map of aggregates of py1, py2 and mc1 in ores from Daqiao (sample DQ200). Py1 aggregates have a core relatively enriched in Pb, Sb and minor Cu, while only As is enriched in py2, and mc1 aggregates are enriched in Sb, Cu, Tl, Pb, Hg and Au except for As. Scale and numbers on the right represent the concentrations of the trace elements.

Fig. 18. Variations of ratios of mean trace element concentrations of py_i (i = 2, 3, 4, 5a, 5b, 6) relative to py_1 (A) and mc_j (j = 1, 2, 3, 4) relative to py_1 at Daqiao, analyzed by laser ablation ICP-MS. Grey area represents the Au-Ag-As-Sb-Hg-Tl-W elemental association.

Fig. 19. Typical ICP-MS count output for pyrite (py3) and marcasite (mc3) analyses by laser ablation. Note the positive correlation between As, Ag, Sb, Hg, Tl, Pb and Au, and that no obvious mineral micro-inclusions are shown in either analysis.

Fig. 20. Trace element LA-ICP-MS map of coarse-grained mc2 with outer rim of zoned mc3 in ores from Daqiao (sample DQ208). Note the zoned mc3 has a $\delta^{34}S$ value of -11.7 with relatively high As and Au compared to mc2 with a $\delta^{34}S$ value of 9.65 and little Ag. The narrow zone of mc3 is enriched in elevated As, Au, Sb, Cu, Tl, Pb, and Hg, while the core of euhedral mc2 contains minor Sb, Cu and Ag. Scale and

numbers on the right represent the concentrations of the trace elements.

Fig. 21. Trace element LA-ICP-MS map of colloform py5b showing relatively uniform sulfur isotopes ($\delta^{34}S$: -2.52–-7.50) and variable trace element compositions (Au: 1.74–62.26 ppm, As: 9,469–17,938 ppm) in ores from Daqiao (sample DQ224). Colloform py5b, especially in the cracked cores, shows significantly elevated As, Au, Sb, Tl and Hg, but is deficient in Cu and Pb, while the rim of py5b has minor Cu and Pb enrichment. Scale and numbers on the right represent the concentrations of the trace elements.

Fig. 22. Histograms showing range of sulfur isotope values of various generations of pyrite (A) and marcasite (B) at Daqiao.

Fig. 23. Variations in sulfur isotope range and mean Au content of pyrite and marcasite from the Daqiao gold deposit. Number of samples for each type and the mean $\delta^{34}S$ values are indicated next to each boxplot.

Fig. 24. Lines ablated within pyrite and marcasite aggregates, showing significant variations in $\delta^{34}S$ between the core and rim. A. Rim of porous diagenetic py1 has an extremely low $\delta^{34}S$ value while the $\delta^{34}S$ value of the core is positive, and both have low trace elements compositions. B. Narrow zone f mc3 contains minor As and Ag and a negative $\delta^{34}S$ value compared to the coarse mc2, which has a positive $\delta^{34}S$ and is devoid of As. C. $\delta^{34}S$ values are consistent in the core of py1 and decrease in the rim; ^{32}S values are deficient in the matrix silicates. D. $\delta^{34}S$ values are highly variable, especially in the mc3 area, while the ^{32}S values remain consistent through mc2 to mc3.

Fig. 25. Raman spectra of disordered CM from samples DQ222 and DQ224 at Daqiao. The numbers in brackets are peak positions/average peak positions in cm^{-1}.

Fig. 26. Correlations between the content of the non-carbonate carbon and the gold grade of early-ore and main-ore stages at Daqiao. Note the strong relationship between gold grade and the non-carbonate carbon in the S2 disseminated ores.

Fig. 27. Diagrammatic genetic model and evolution of the multistage brecciation at Daqiao.

Table 1. Summary of common textures, timing, gold contents, and sulfur isotopes for sulfide types at the Daqiao gold deposit.

Table 2. Summarized LA-ICP-MS analyses of pyrite and marcasite hosted by sediments from within and outside the ore zone of the Daqiao gold deposit.

Table 3. LA-MC-ICP-MS in situ sulfur isotope composition of different sulfide types from the Daqiao gold deposit.

Table 4. Relevant parameters of Raman spectra and estimated temperatures of samples investigated at the Daqiao gold deposit.

APPENDIX 1

Table A1. LA-ICP-MS analyses of pyrite and marcasite hosted by sediments from within and outside the ore zone of the Daqiao gold deposit.

Fig. 1

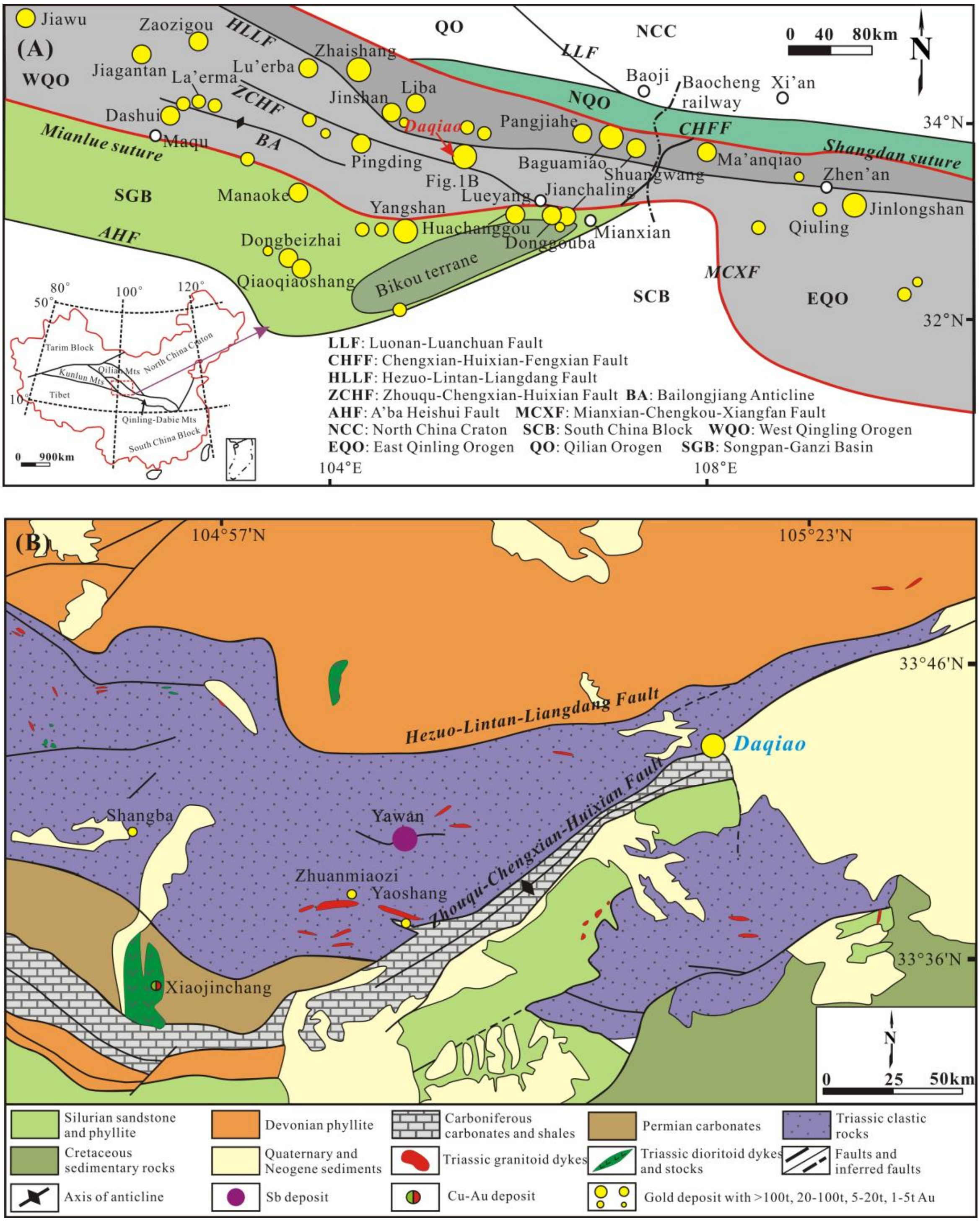

(A)
Jiawu
Zaozigou
HLLF
QO
NCC
0 40 80km
N
WQO
Jiagantan
La'erma
Lu'erba
Zhaishang
LLF
Baoji
Baocheng railway
Xi'an
ZCHF
Jinshan
Liba
NQO
34°N
Dashui
Maqu
BA
Daqiao
Pangjiahe
CHFF
Mianlue suture
Pingding
Baguamiao
Ma'anqiao
Shangdan suture
Fig.1B
Shuangwang
Zhen'an
SGB
Manaoke
Lueyang
Jianchaling
Yangshan
Jinlongshan
AHF
Huachanggou
Donggouba
Mianxian
Qiuling
Dongbeizhai
Qiaoqiaoshang
Bikou terrane
MCXF
SCB
EQO
32°N
80° 100° 120°
50°
Tarim Block
North China Craton
Qilian Mts
Kunlun Mts
Tibet
Qinling-Dabie Mts
South China Block
0 900km
LLF: Luonan-Luanchuan Fault
CHFF: Chengxian-Huixian-Fengxian Fault
HLLF: Hezuo-Lintan-Liangdang Fault
ZCHF: Zhouqu-Chengxian-Huixian Fault BA: Bailongjiang Anticline
AHF: A'ba Heishui Fault MCXF: Mianxian-Chengkou-Xiangfan Fault
NCC: North China Craton SCB: South China Block WQO: West Qingling Orogen
EQO: East Qinling Orogen QO: Qilian Orogen SGB: Songpan-Ganzi Basin
104°E
108°E
(B)
104°57'N
105°23'N
33°46'N
Hezuo-Lintan-Liangdang Fault
Daqiao
Zhouqu-Chengxian-Huixian Fault
Shangba
Yawan
Zhuanmiaozi
Yaoshang
33°36'N
Xiaojinchang
N
0 25 50km
Silurian sandstone and phyllite
Devonian phyllite
Carboniferous carbonates and shales
Permian carbonates
Triassic clastic rocks
Cretaceous sedimentary rocks
Quaternary and Neogene sediments
Triassic granitoid dykes
Triassic dioritoid dykes and stocks
Faults and inferred faults
Axis of anticline
Sb deposit
Cu-Au deposit
Gold deposit with >100t, 20-100t, 5-20t, 1-5t Au

Fig. 2

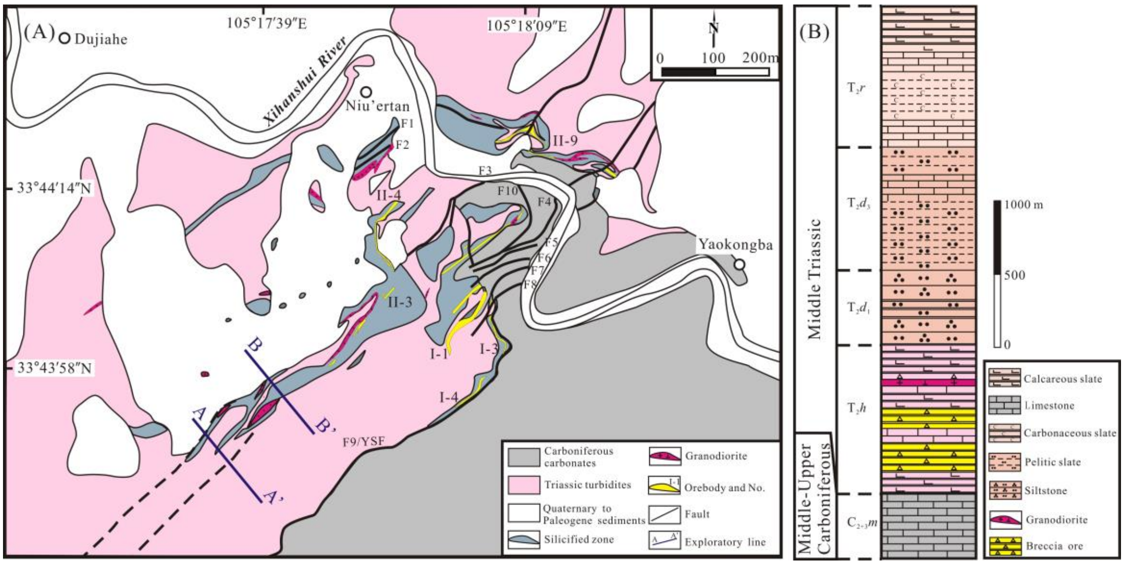
(A)
Dujiahe
105°17′39″E
105°18′09″E
N
0 100 200m
Xihanshui River
Niu'ertan
F1
F2
F3
F10
F4
F5
F6
F7
F8
II-9
II-4
II-3
I-1
I-3
I-4
33°44′14″N
33°43′58″N
Yaokongba
A
A'
B
B'
F9/YSF
Carboniferous carbonates
Triassic turbidites
Quaternary to Paleogene sediments
Silicified zone
Granodiorite
Orebody and No.
Fault
Exploratory line
(B)
Middle Triassic
Middle-Upper Carboniferous
T_2r
T_2d_3
T_2d_1
T_2h
$C_{2-3}m$
1000 m
500
0
Calcareous slate
Limestone
Carbonaceous slate
Pelitic slate
Siltstone
Granodiorite
Breccia ore

Fig. 3

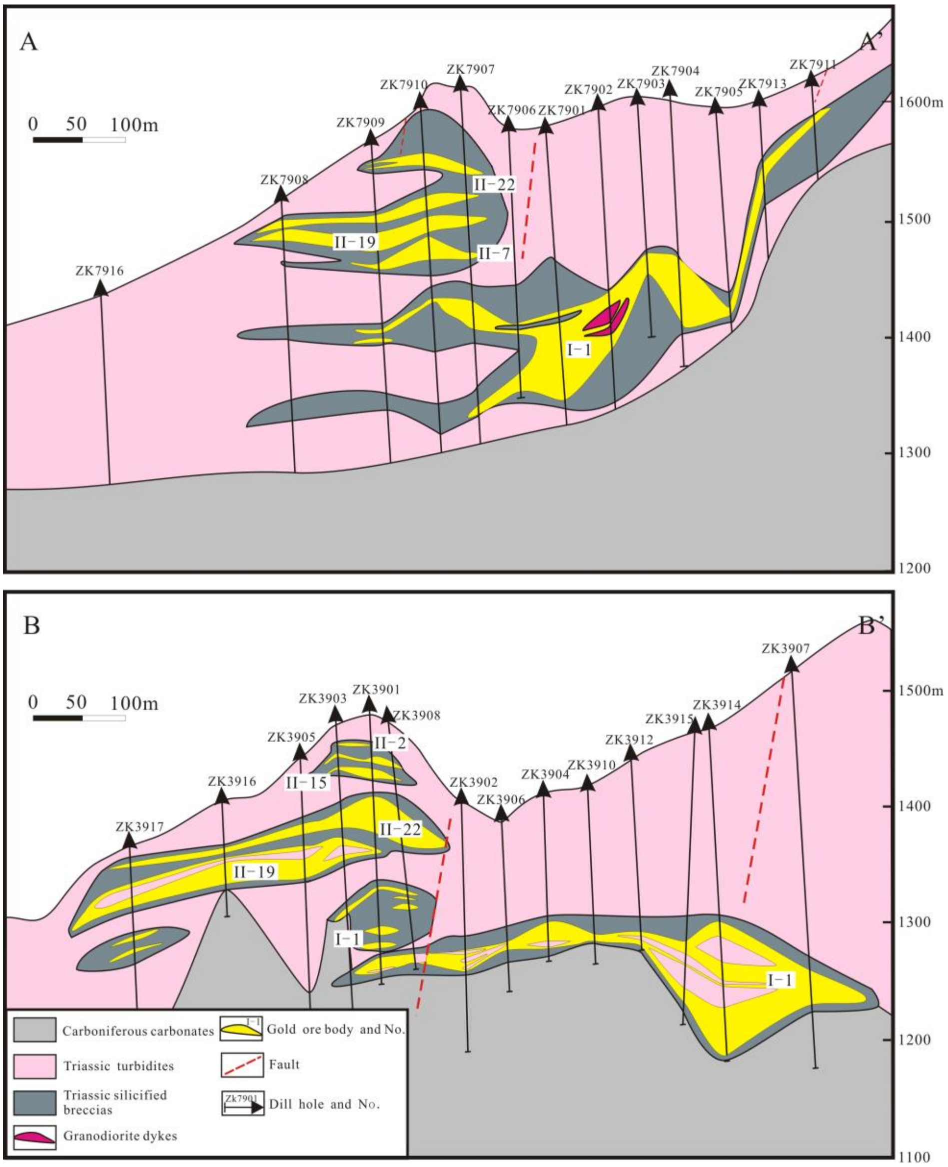

A
A'
0 50 100m
ZK7916
ZK7908
ZK7909
ZK7910
ZK7907
ZK7906
ZK7901
ZK7902
ZK7903
ZK7904
ZK7905
ZK7913
ZK7911
II-22
II-19
II-7
I-1
1600m
1500
1400
1300
1200
B
B'
0 50 100m
ZK3917
ZK3916
ZK3905
ZK3903
ZK3901
ZK3908
ZK3902
ZK3906
ZK3904
ZK3910
ZK3912
ZK3915
ZK3914
ZK3907
II-2
II-15
II-22
II-19
I-1
I-1
1500m
1400
1300
1200
1100
Carboniferous carbonates
Triassic turbidites
Triassic silicified breccias
Granodiorite dykes
Gold ore body and No.
Fault
Dill hole and No.

Fig. 4

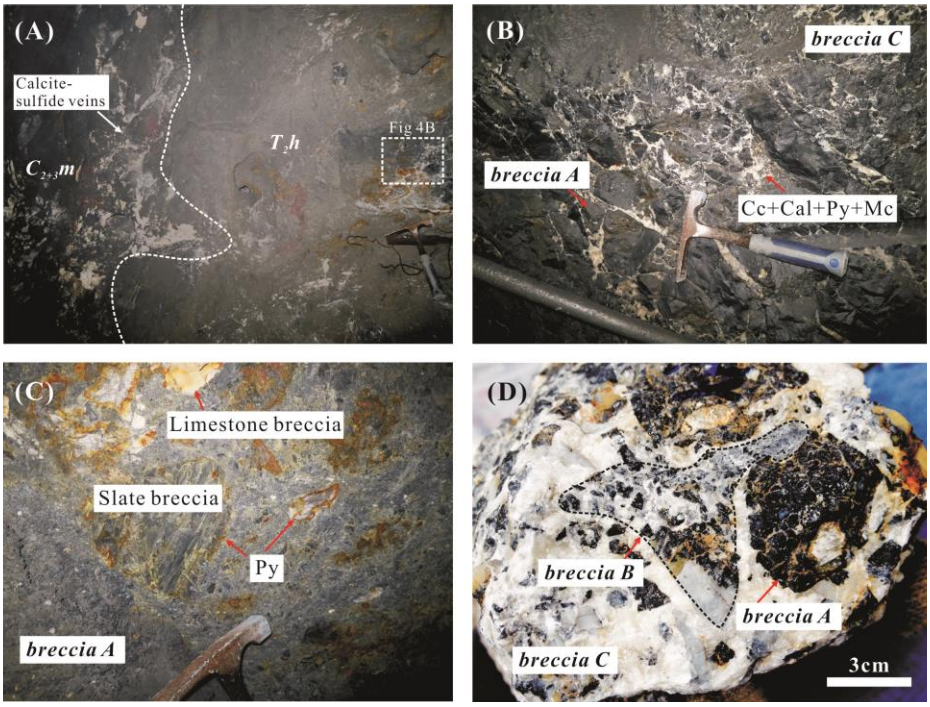
(A)
Calcite-sulfide veins
$C_{2+3}m$
T_2h
Fig 4B
(B)
breccia C
breccia A
Cc+Cal+Py+Mc
(C)
Limestone breccia
Slate breccia
Py
breccia A
(D)
breccia B
breccia A
breccia C
3cm

Fig. 5

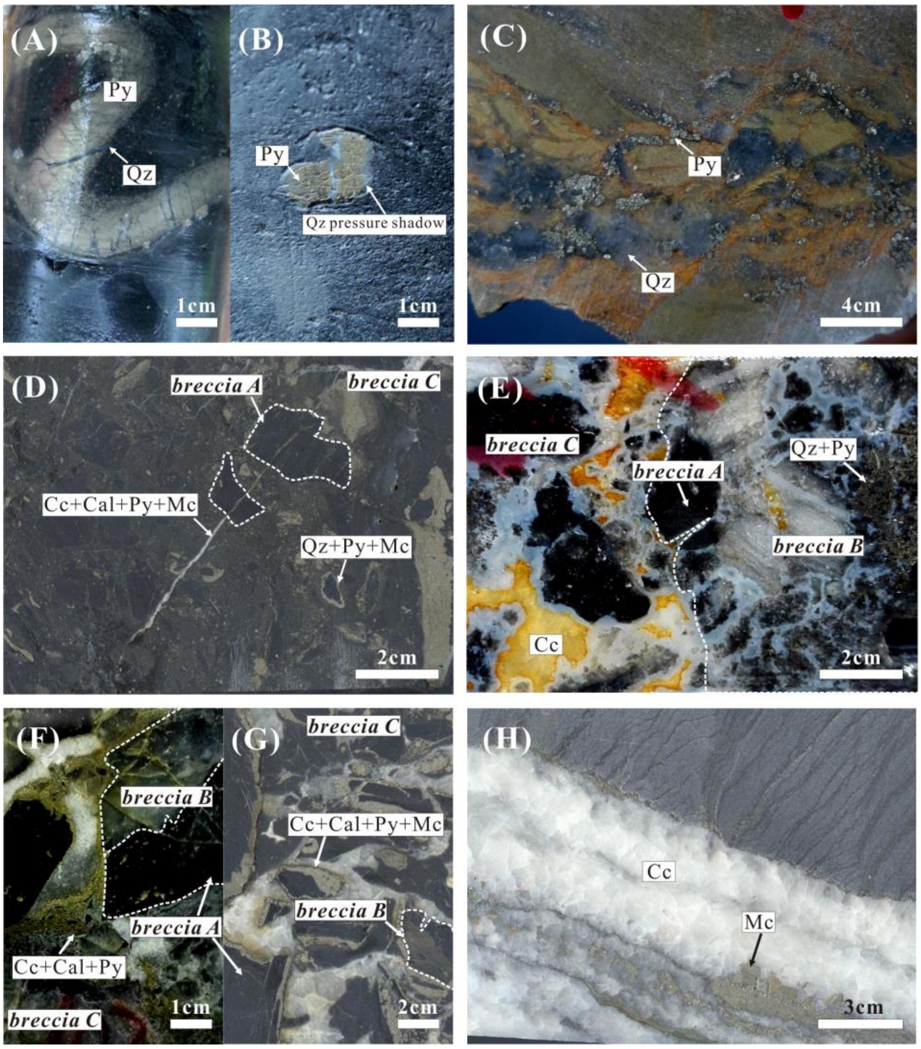

(A)
Py
Qz
1cm
(B)
Py
Qz pressure shadow
1cm
(C)
Py
Qz
4cm
(D)
breccia A
breccia C
Cc+Cal+Py+Mc
Qz+Py+Mc
2cm
(E)
breccia C
breccia A
Qz+Py
breccia B
Cc
2cm
(F)
breccia B
breccia A
Cc+Cal+Py
breccia C
1cm
(G)
breccia C
Cc+Cal+Py+Mc
breccia B
2cm
(H)
Cc
Mc
3cm

Fig. 6

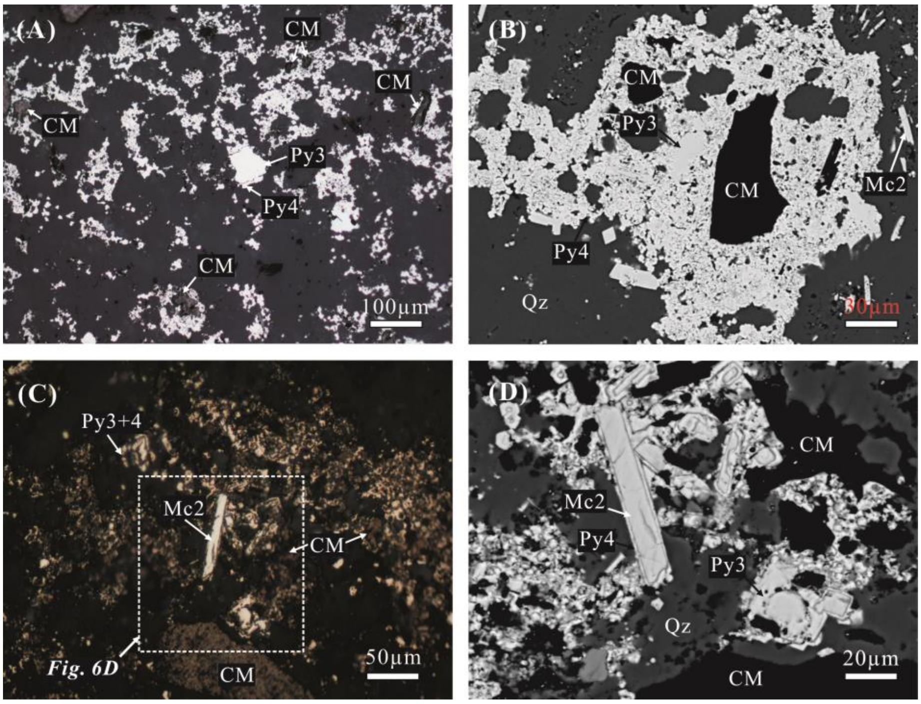

(A)
CM
CM
CM
Py3
Py4
CM
100µm
(B)
CM
Py3
CM
Mc2
Py4
Qz
(C)
Py3+4
Mc2
CM
Fig. 6D
CM
50µm
(D)
CM
Mc2
Py4
Py3
Qz
CM
20µm

Fig. 7

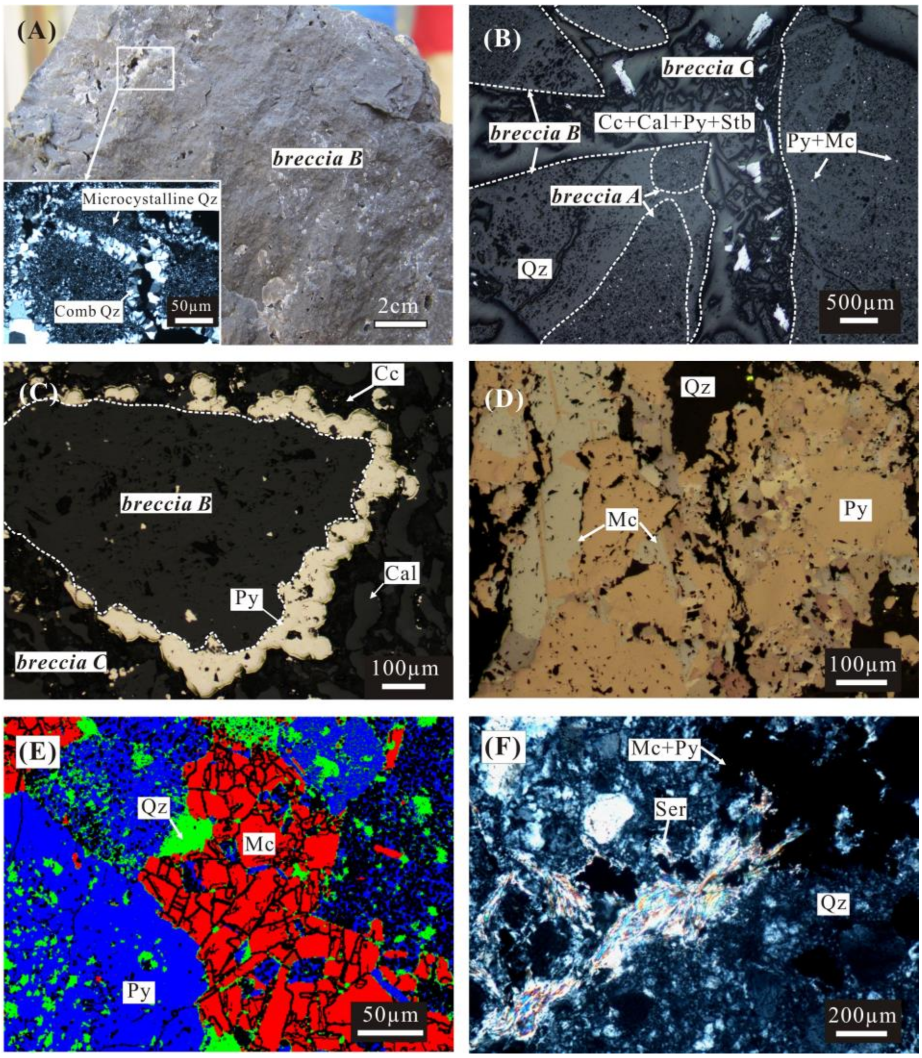
(A)
breccia B
Microcystalline Qz
Comb Qz
50μm
2cm
(B)
breccia C
Cc+Cal+Py+Stb
breccia B
Py+Mc
breccia A
Qz
500μm
(C)
Cc
breccia B
Cal
Py
breccia C
100μm
(D)
Qz
Mc
Py
100μm
(E)
Qz
Mc
Py
50μm
(F)
Mc+Py
Ser
Qz
200μm

Fig. 8

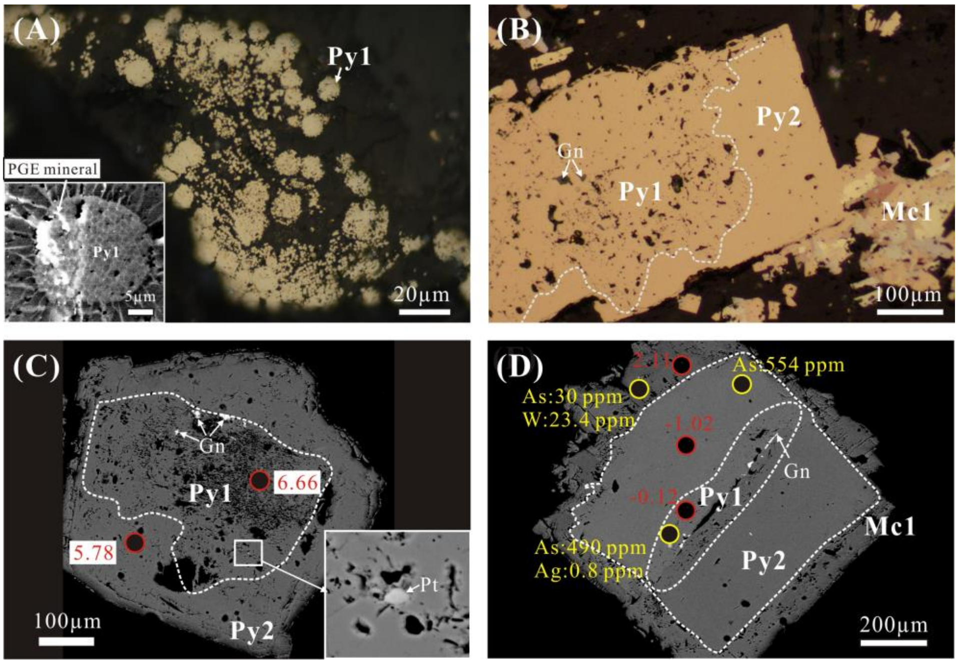
(A)
Py1
PGE mineral
Py1
5μm
20μm
(B)
Py2
Gn
Py1
Mc1
100μm
(C)
Gn
Py1
6.66
5.78
Pt
100μm
Py2
(D)
2.11
As:554 ppm
As:30 ppm
W:23.4 ppm
-1.02
Gn
-0.12
Py1
Mc1
As:490 ppm
Ag:0.8 ppm
Py2
200μm

Fig. 9

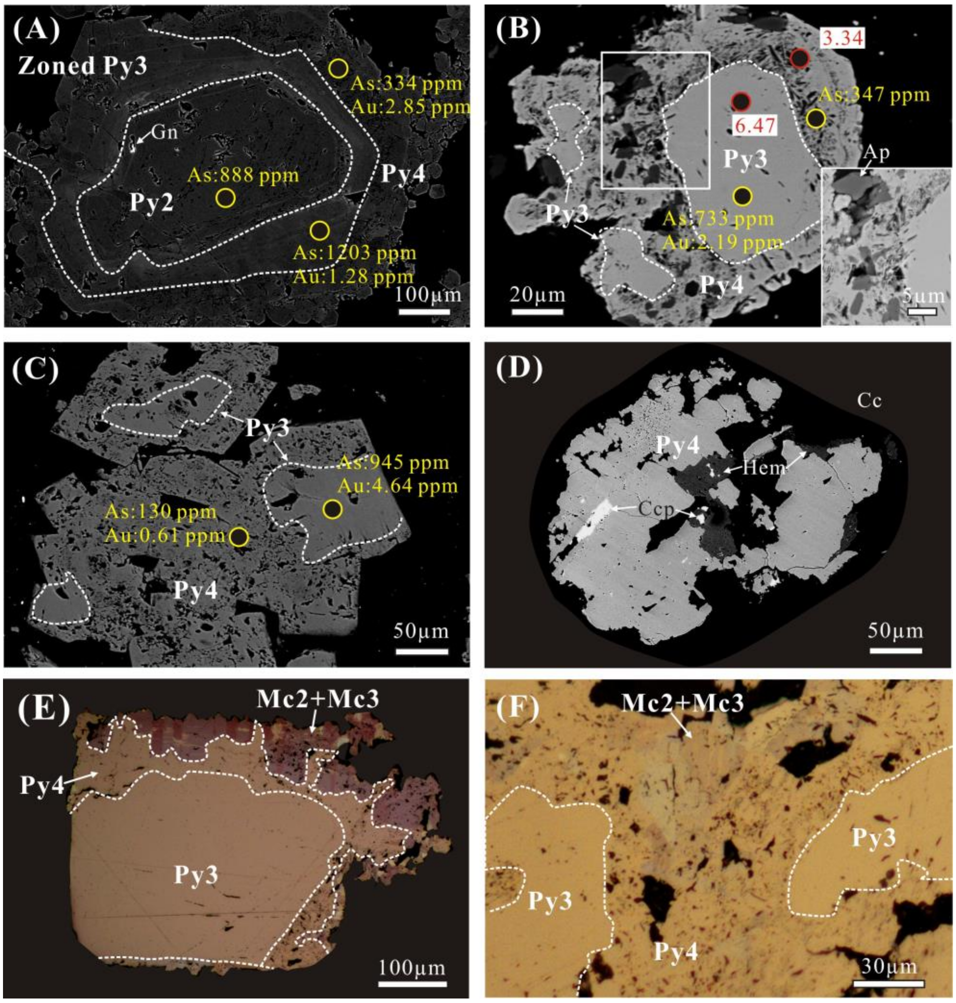

(A)
Zoned Py3
As:334 ppm
Au:2.85 ppm
Gn
As:888 ppm
Py4
Py2
As:1203 ppm
Au:1.28 ppm
100μm
(B)
3.34
6.47
As:347 ppm
Py3
Ap
Py3
As:733 ppm
Au:2.19 ppm
Py4
20μm
5μm
(C)
Py3
As:945 ppm
Au:4.64 ppm
As:130 ppm
Au:0.61 ppm
Py4
50μm
(D)
Cc
Py4
Hem
Ccp
50μm
(E)
Mc2+Mc3
Py4
Py3
100μm
(F)
Mc2+Mc3
Py3
Py3
Py4
30μm

Fig. 10

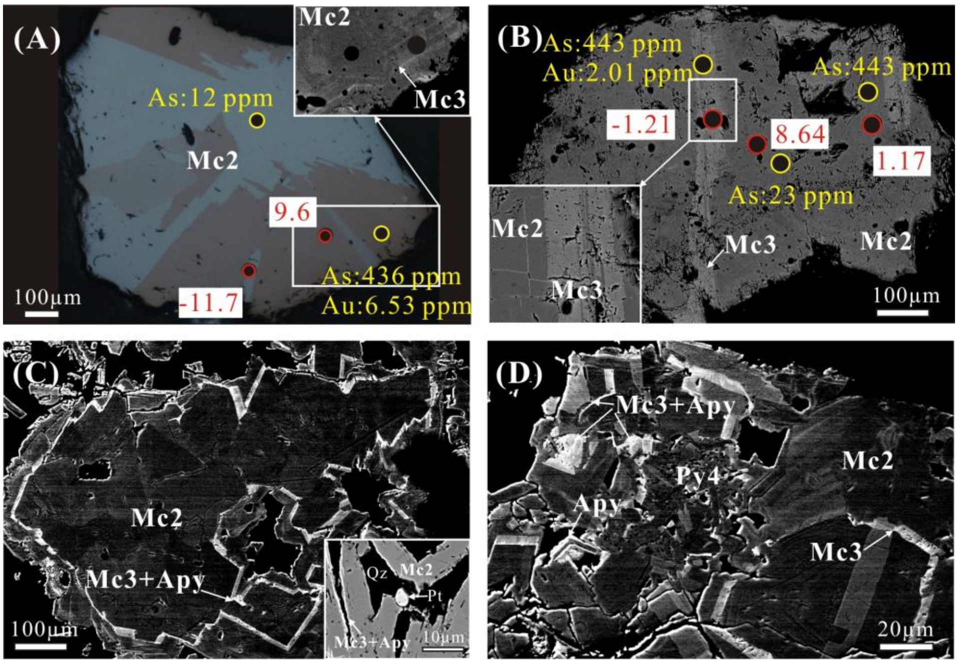
(A)
Mc2
Mc3
As:12 ppm
Mc2
9.6
As:436 ppm
Au:6.53 ppm
-11.7
100μm
(B)
As:443 ppm
Au:2.01 ppm
As:443 ppm
-1.21
8.64
1.17
As:23 ppm
Mc2
Mc3
Mc3
Mc2
100μm
(C)
Mc2
Mc3+Apy
Qz
Mc2
Pt
Mc3+Apy
10μm
100μm
(D)
Mc3+Apy
Py4
Apy
Mc2
Mc3
20μm

1855 **Fig. 11**

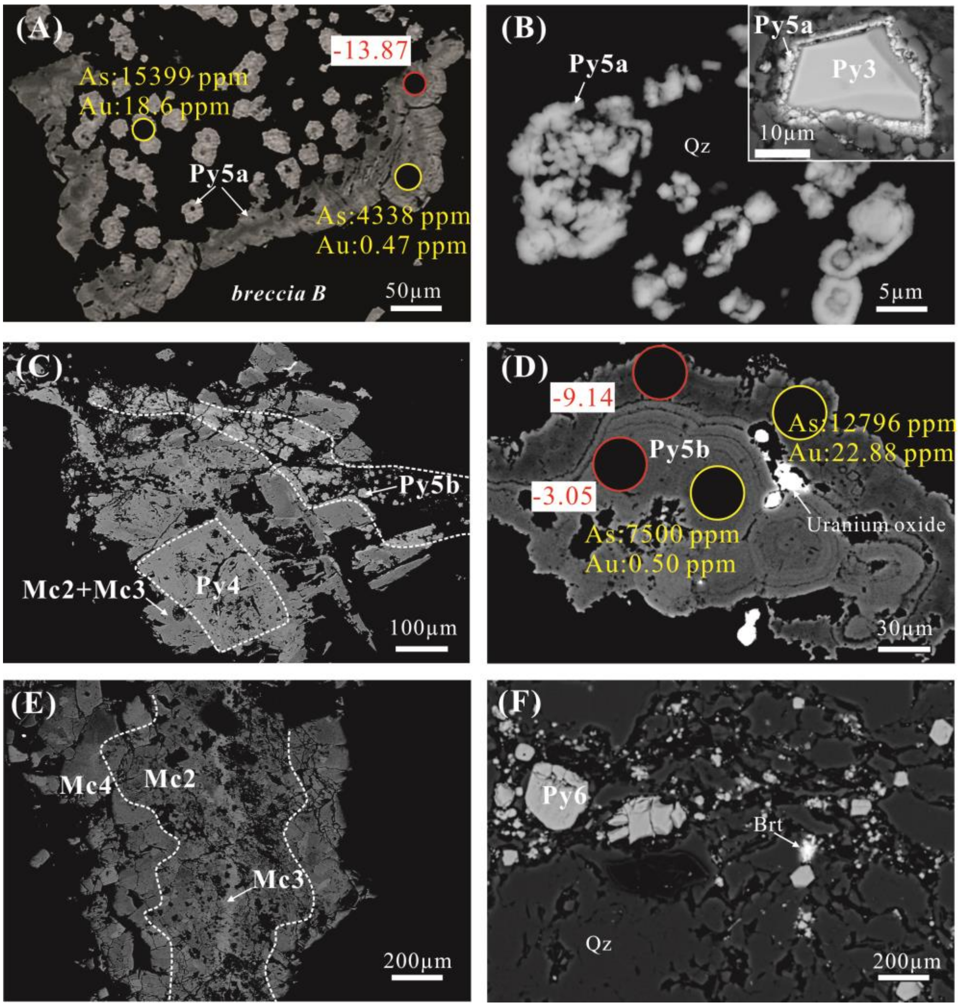

1856

1857

Fig. 12

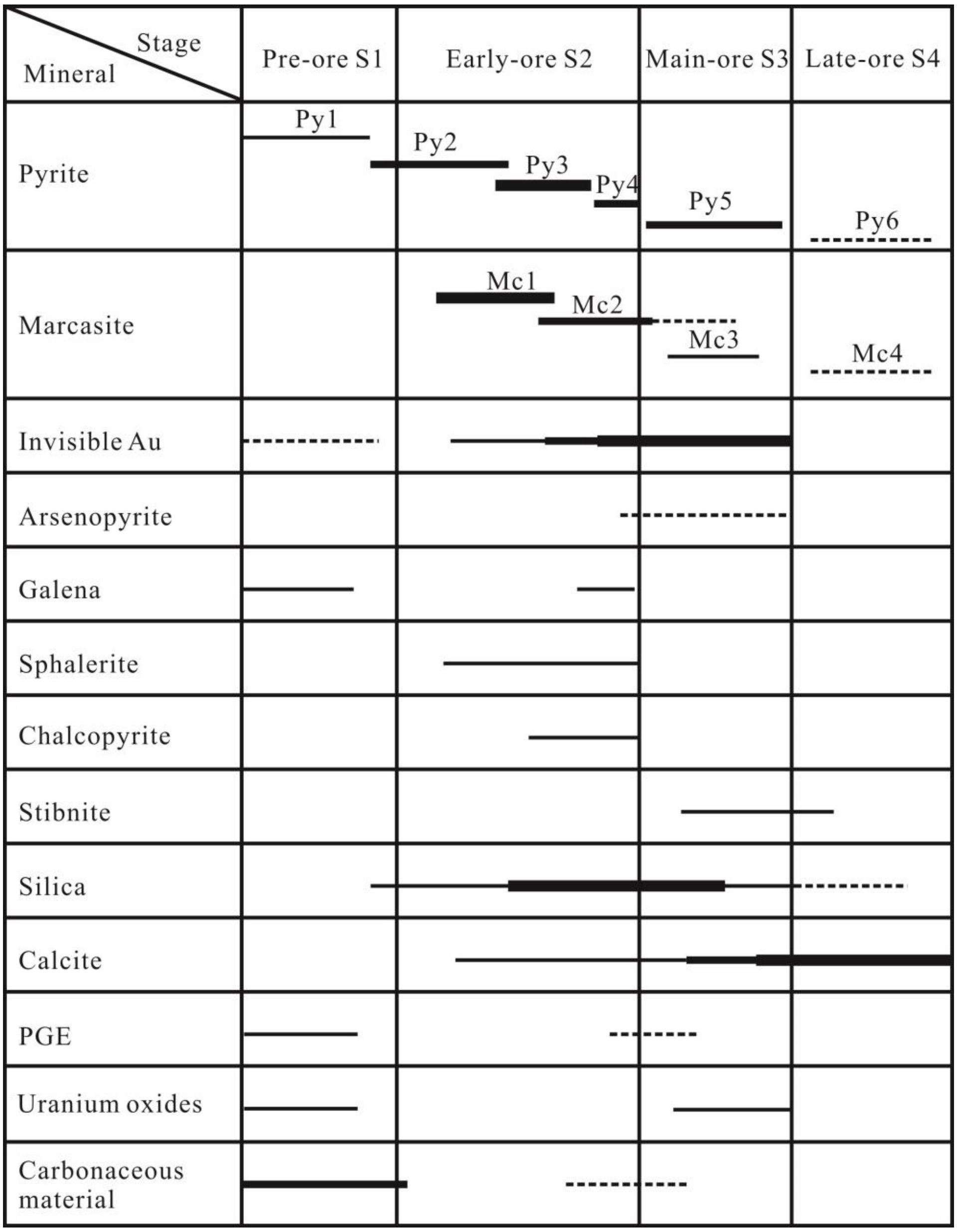

Stage
Mineral
Pre-ore S1
Early-ore S2
Main-ore S3
Late-ore S4
Pyrite
Py1
Py2
Py3
Py4
Py5
Py6
Marcasite
Mc1
Mc2
Mc3
Mc4
Invisible Au
Arsenopyrite
Galena
Sphalerite
Chalcopyrite
Stibnite
Silica
Calcite
PGE
Uranium oxides
Carbonaceous material

1861 **Fig. 13**

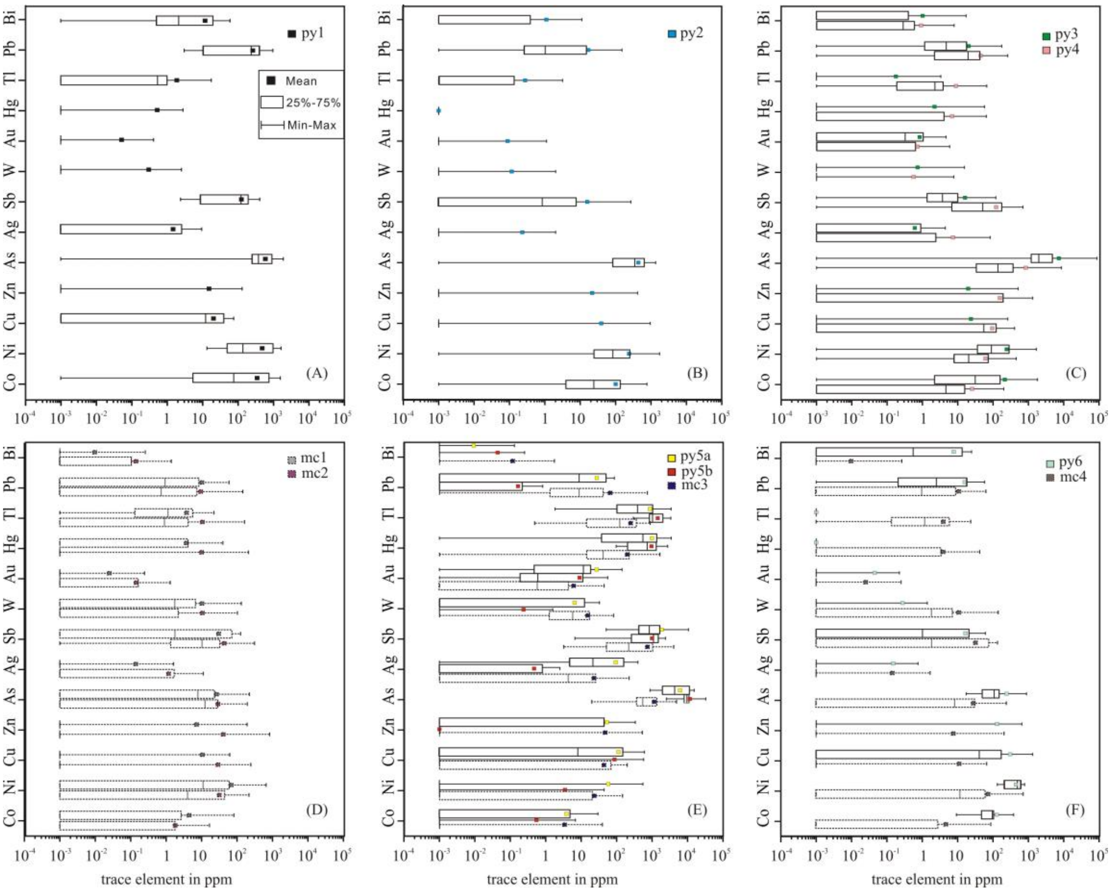

1862

1863

Fig. 14

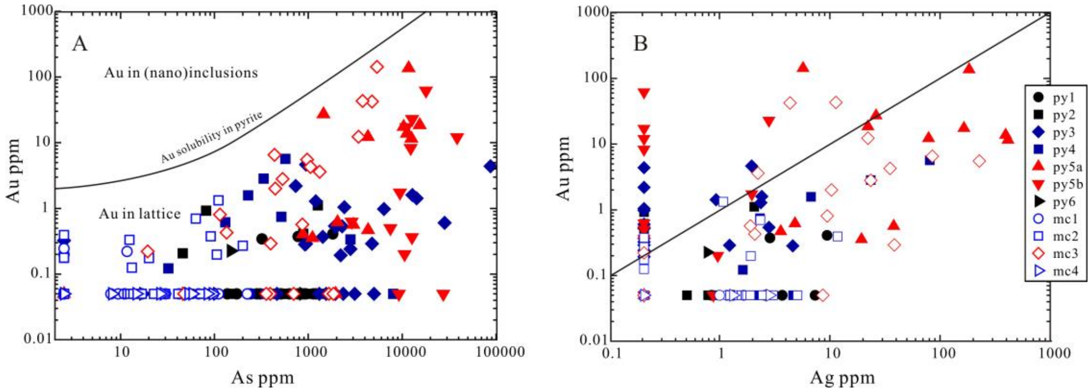

A
Au in (nano)inclusions
Au solubility in pyrite
Au in lattice
Au ppm
As ppm
B
Au ppm
Ag ppm
py1
py2
py3
py4
py5a
py5b
py6
mc1
mc2
mc3
mc4

Fig. 15

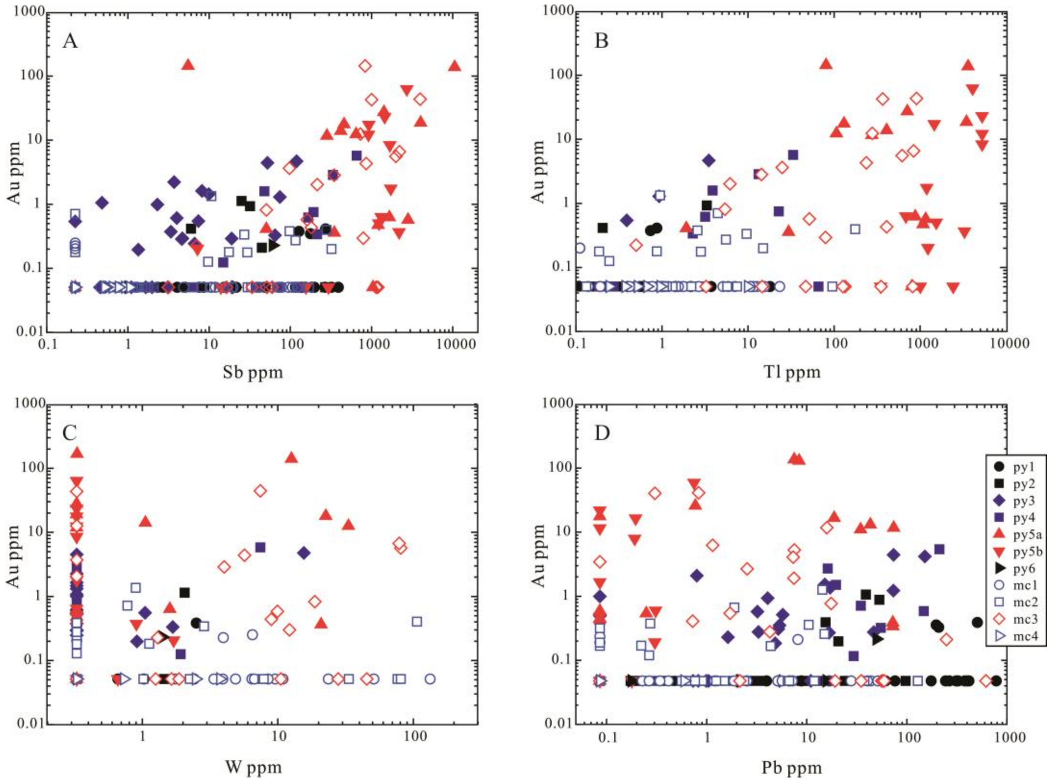

A
Au ppm
Sb ppm
B
Au ppm
Tl ppm
C
Au ppm
W ppm
D
Au ppm
Pb ppm
py1
py2
py3
py4
py5a
py5b
py6
mc1
mc2
mc3
mc4

Fig. 16

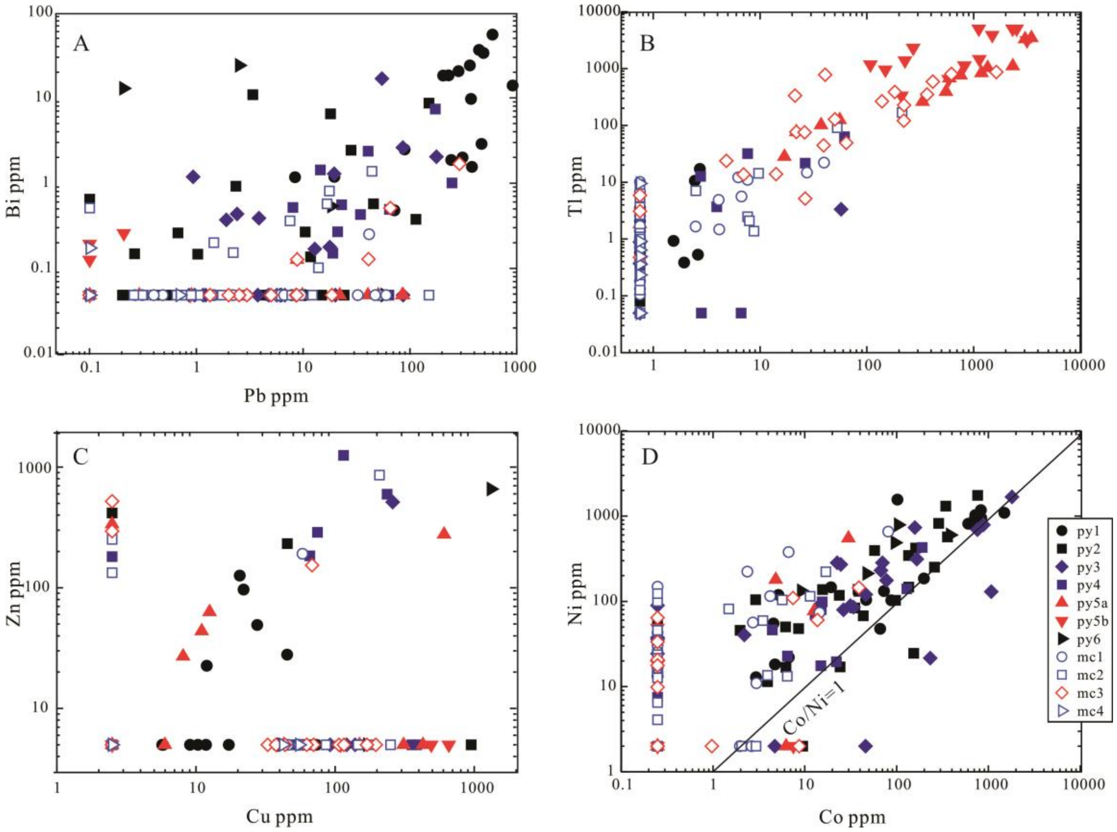
A
Bi ppm
Pb ppm
B
Tl ppm
C
Zn ppm
Cu ppm
D
Ni ppm
Co ppm
Co/Ni=1
py1
py2
py3
py4
py5a
py5b
py6
mc1
mc2
mc3
mc4

Fig. 17

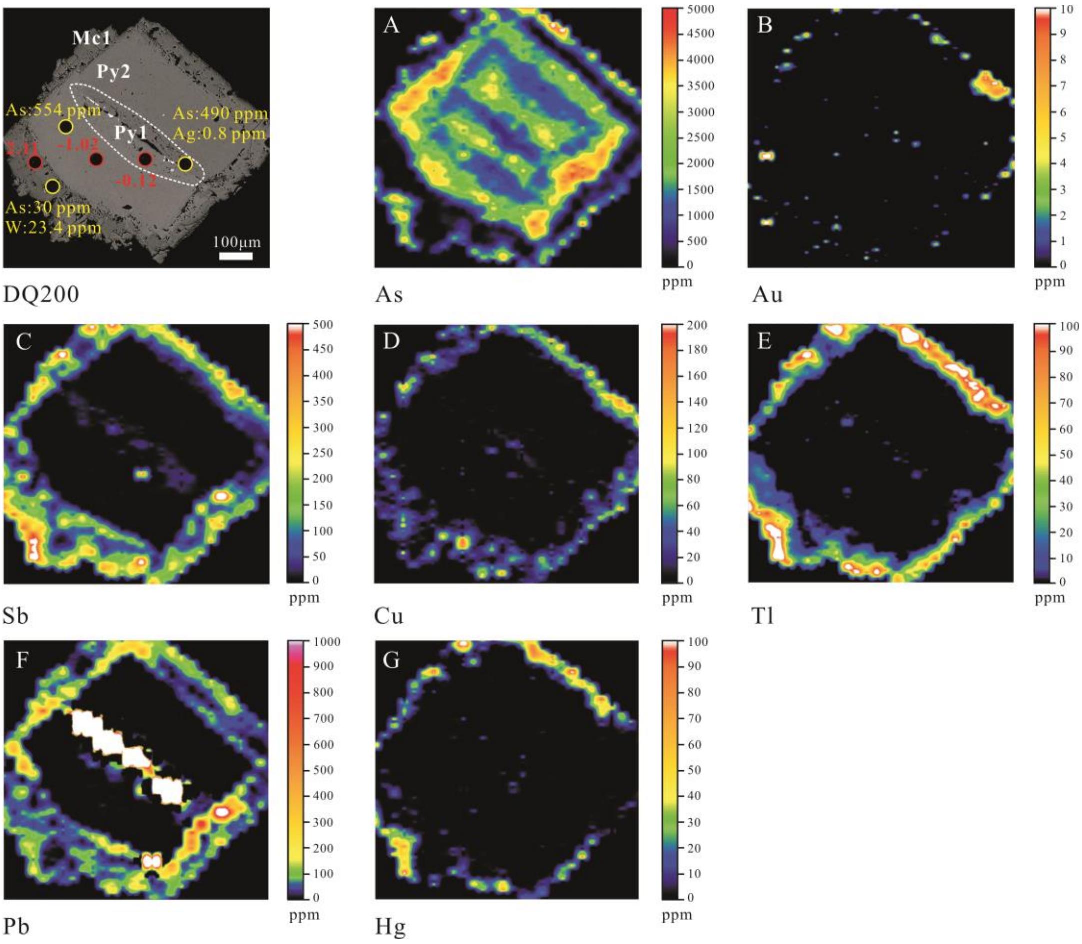

Mc1
Py2
Py1
As:554 ppm
As:490 ppm
Ag:0.8 ppm
As:30 ppm
W:23.4 ppm
100μm
DQ200
A
As
B
Au
C
Sb
D
Cu
E
Tl
F
Pb
G
Hg
ppm

Fig. 18

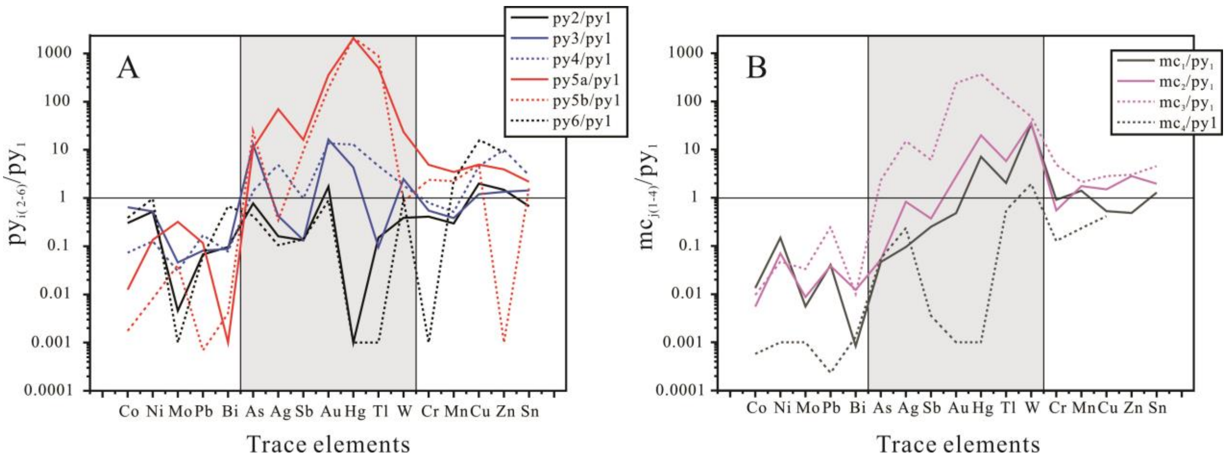

A
py2/py1
py3/py1
py4/py1
py5a/py1
py5b/py1
py6/py1
$py_{i(2-6)}/py_1$
B
mc_1/py_1
mc_2/py_1
mc_3/py_1
$mc_4/py1$
$mc_{j(1-4)}/py_1$
1000
100
10
1
0.1
0.01
0.001
0.0001
Co Ni Mo Pb Bi As Ag Sb Au Hg Tl W Cr Mn Cu Zn Sn
Trace elements

Fig. 19

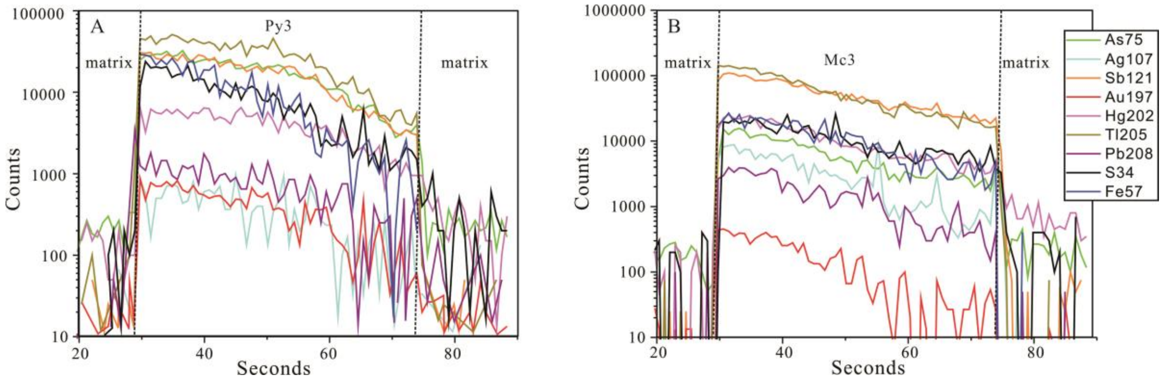
A
Py3
matrix
matrix
Counts
Seconds
B
Mc3
matrix
matrix
Counts
Seconds
As75
Ag107
Sb121
Au197
Hg202
Tl205
Pb208
S34
Fe57

Fig. 20

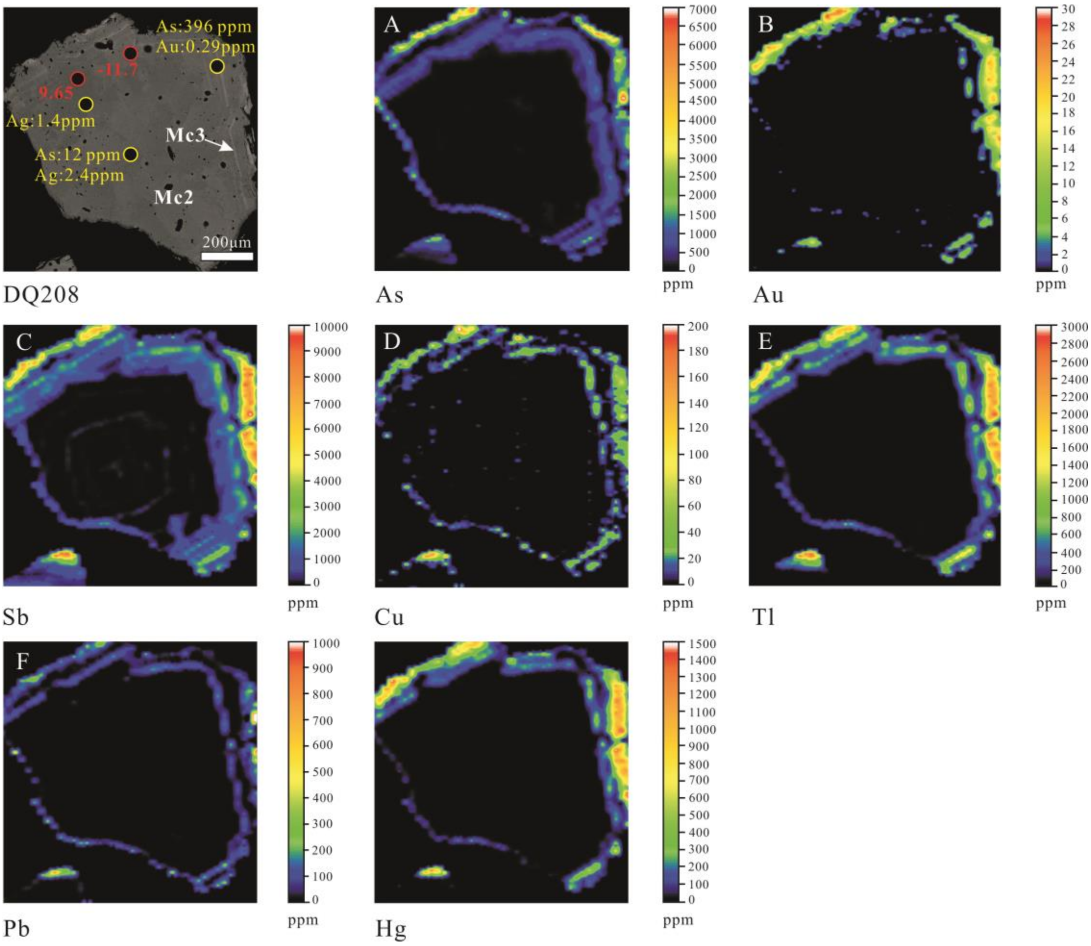
As:396 ppm
Au:0.29ppm
-11.7
9.65
Ag:1.4ppm
Mc3
As:12 ppm
Ag:2.4ppm
Mc2
200μm
DQ208
A
As
B
Au
C
Sb
D
Cu
E
Tl
F
Pb
Hg
ppm

Fig. 21

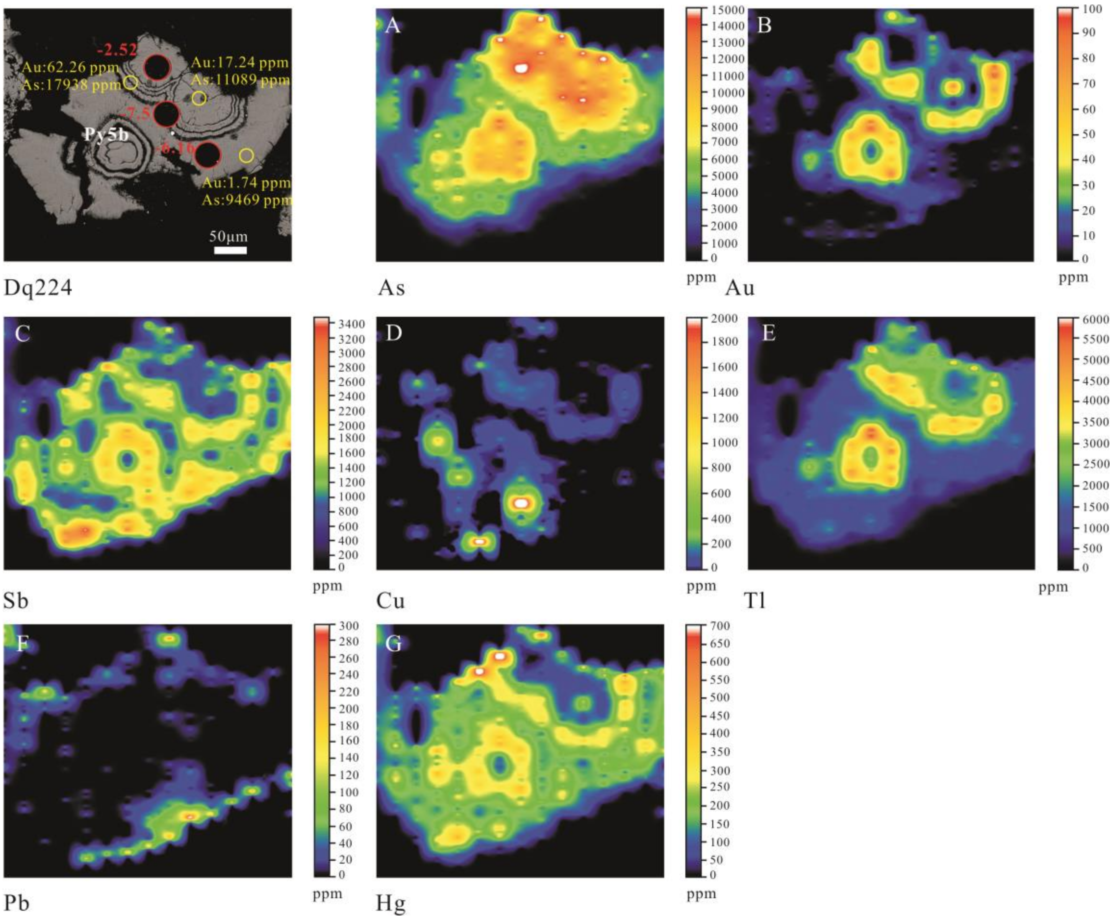
-2.52
Au:62.26 ppm
As:17938 ppm
Au:17.24 ppm
As:11089 ppm
7.5
Py5b
8.16
Au:1.74 ppm
As:9469 ppm
50μm
Dq224
A
As
B
Au
C
Sb
D
Cu
E
Tl
F
Pb
G
Hg
ppm

Fig. 22

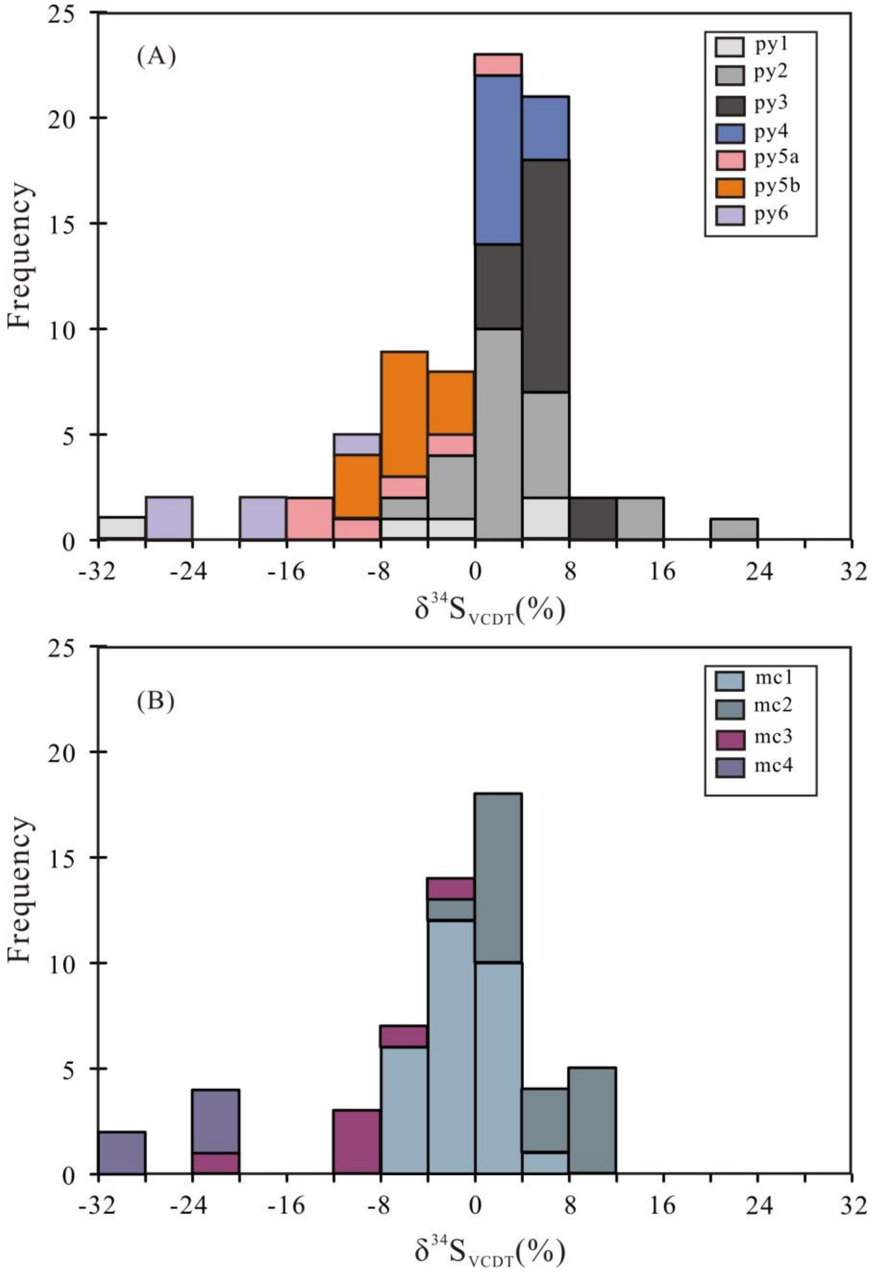
(A)
Frequency
0
5
10
15
20
25
-32
-24
-16
-8
0
8
16
24
32
δ34SVCDT(%)
py1
py2
py3
py4
py5a
py5b
py6
(B)
Frequency
0
5
10
15
20
25
-32
-24
-16
-8
0
8
16
24
32
δ34SVCDT(%)
mc1
mc2
mc3
mc4

Fig. 23

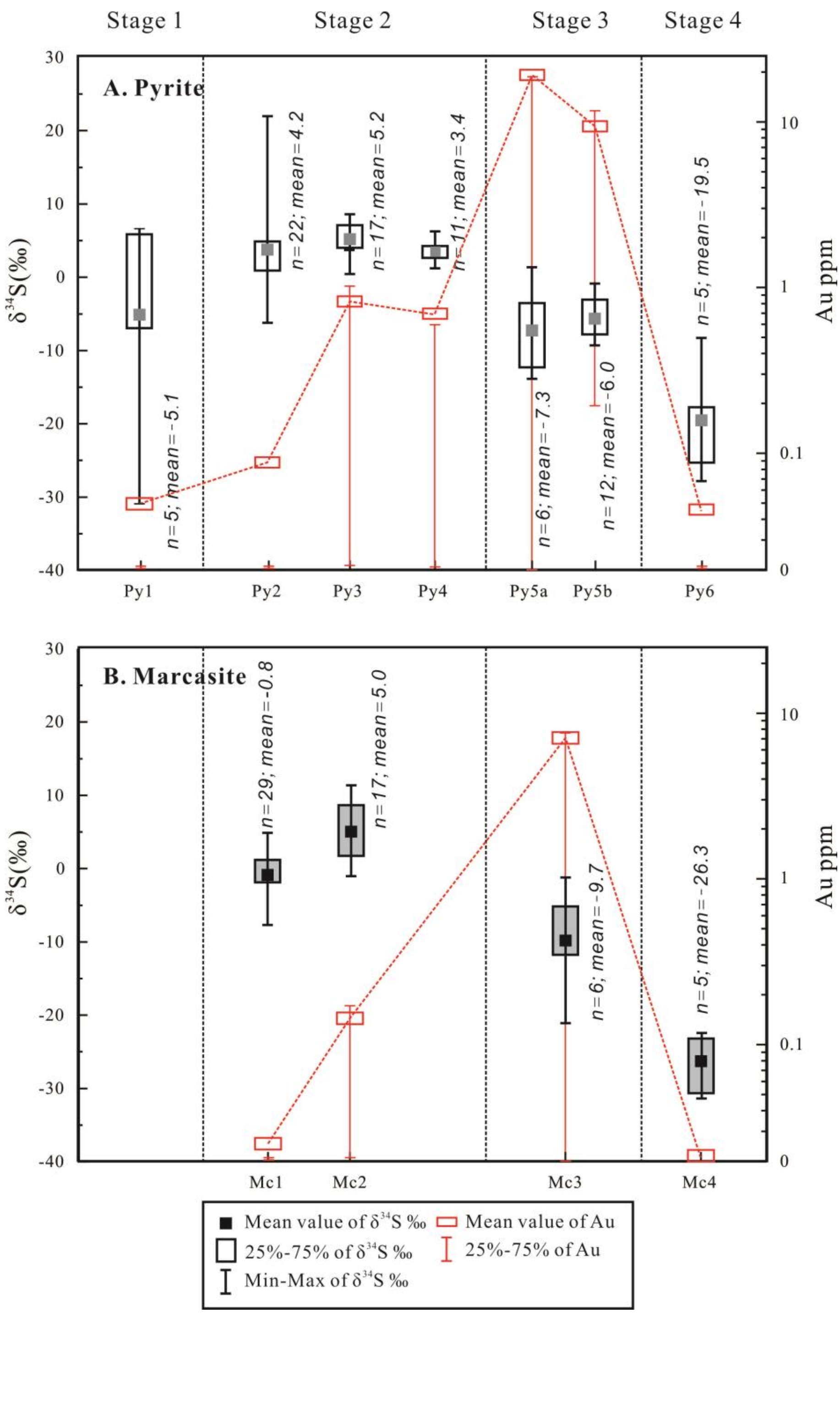
Stage 1
Stage 2
Stage 3
Stage 4
A. Pyrite
B. Marcasite
δ34S(‰)
Au ppm
n=5; mean=-5.1
n=22; mean=4.2
n=17; mean=5.2
n=11; mean=3.4
n=6; mean=-7.3
n=12; mean=-6.0
n=5; mean=-19.5
n=29; mean=-0.8
n=17; mean=5.0
n=6; mean=-9.7
n=5; mean=-26.3
Py1
Py2
Py3
Py4
Py5a
Py5b
Py6
Mc1
Mc2
Mc3
Mc4
Mean value of δ34S ‰
Mean value of Au
25%-75% of δ34S ‰
25%-75% of Au
Min-Max of δ34S ‰

Fig. 24

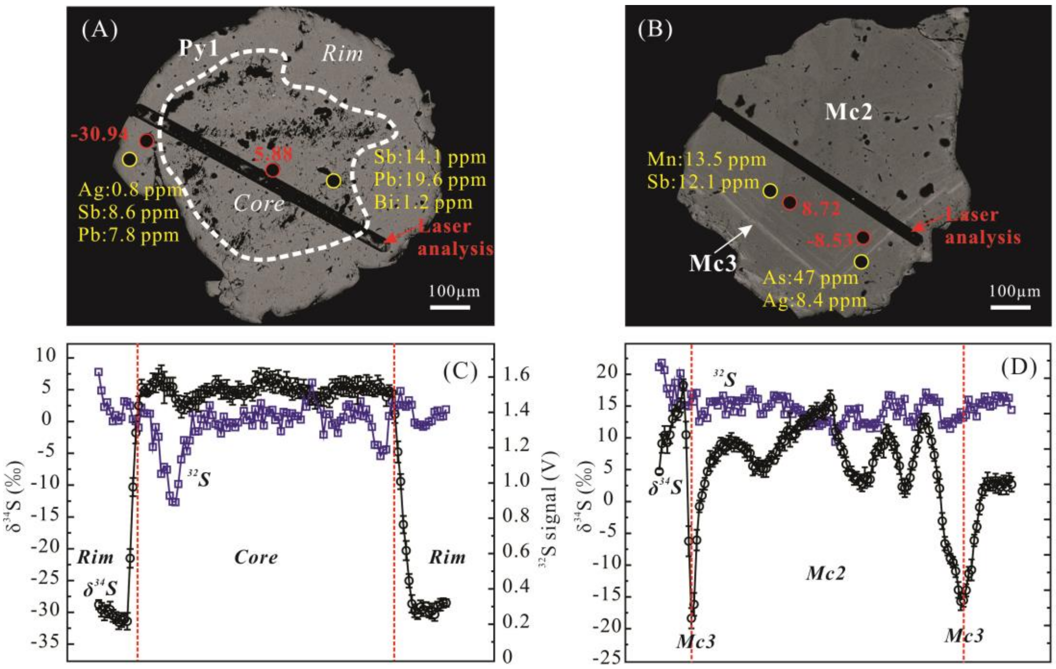
(A)
Py1
Rim
-30.94
5.88
Core
Sb:14.1 ppm
Pb:19.6 ppm
Bi:1.2 ppm
Ag:0.8 ppm
Sb:8.6 ppm
Pb:7.8 ppm
Laser analysis
100μm
(B)
Mc2
Mn:13.5 ppm
Sb:12.1 ppm
8.72
-8.53
Mc3
As:47 ppm
Ag:8.4 ppm
Laser analysis
100μm
(C)
δ^{34}S (‰)
^{32}S signal (V)
^{32}S
Rim
Core
Rim
δ^{34}S
(D)
^{32}S
δ^{34}S
Mc2
Mc3
Mc3

Fig. 25

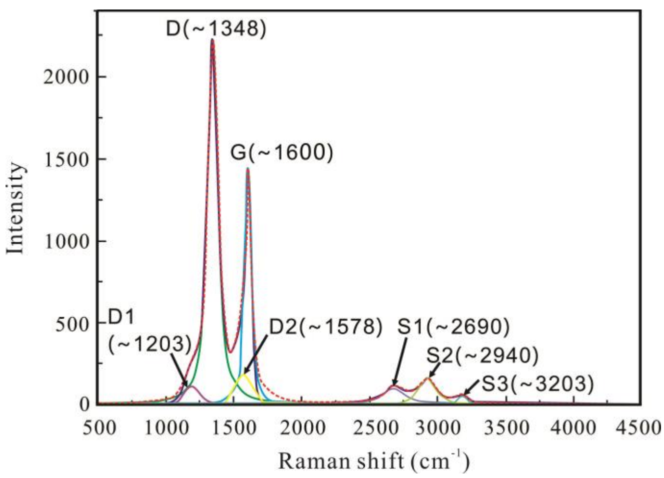
D(~1348)
G(~1600)
D1
(~1203)
D2(~1578)
S1(~2690)
S2(~2940)
S3(~3203)
Intensity
Raman shift (cm^{-1})

Fig. 26

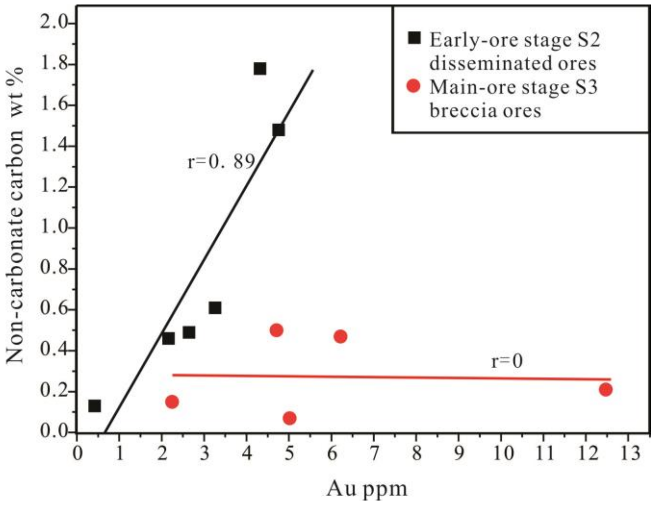
Early-ore stage S2
disseminated ores
Main-ore stage S3
breccia ores
r=0. 89
r=0
Non-carbonate carbon wt %
Au ppm
0.0
0.2
0.4
0.6
0.8
1.0
1.2
1.4
1.6
1.8
2.0
0
1
2
3
4
5
6
7
8
9
10
11
12
13

Fig. 27

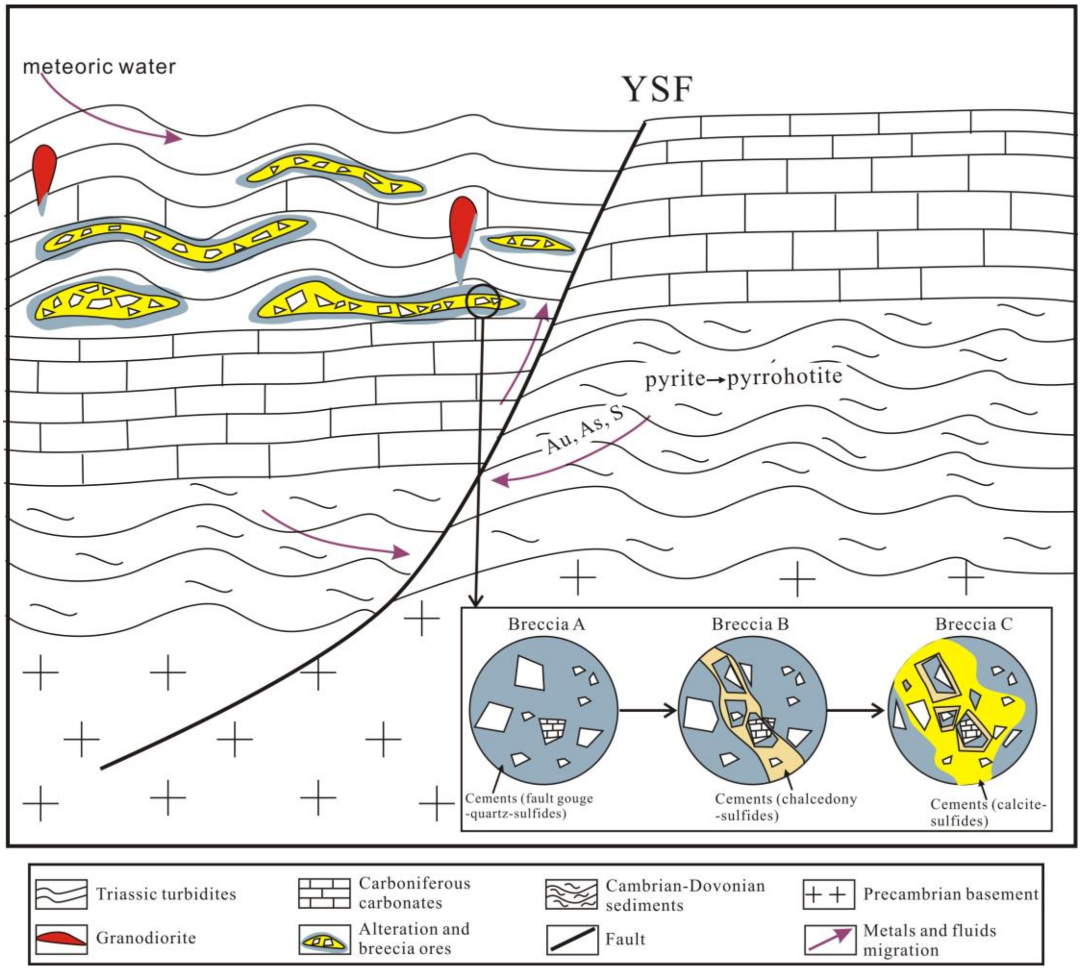
meteoric water
YSF
pyrite→pyrrohotite
Au, As, S
Breccia A
Breccia B
Breccia C
Cements (fault gouge
-quartz-sulfides)
Cements (chalcedony
-sulfides)
Cements (calcite-
sulfides)
Triassic turbidites
Carboniferous
carbonates
Cambrian-Dovonian
sediments
Precambrian basement
Granodiorite
Alteration and
breccia ores
Fault
Metals and fluids
migration

Table 1

TABLE 1. Summary of Common Textures, Timing, Gold Contents and Sulfur Isotopes for Sulfide Types at the Daqiao Gold Deposit

Sulfide type	Textures	Timing	Evidences for timing	Gold contents (ppm)	$\delta^{34}S$ (‰)
Py1	Framboidal and sooty, fine-grained stratiform or microeuhedra	Pre-ore stage S1	Overgrown by all later pyrite and marcasite types, stratiform texture similar to syn-diagenetic pyrite	b.d.l.–0.41; mean: 0.05	-30.9–+6.7; mean: -5.1
Py2	Clear or porous euhedra with sooty py1 core	Early-ore stage S2	Disseminations in the breccia A; overgrows py1 and is surrounded by mc1	b.d.l.–1.11; mean: 0.10	-6.2–+22.0; mean: +4.2
Mc1	Fine-grained euhedra	Early-ore stage S2	Intergrows py2	b.d.l.–0.24; mean: 0.03	-7.7–+4.9; mean: -0.8
Py3	Zoned euhedra and inclusion-free	Early-ore stage S2	Disseminations in the breccia A; overgrows py2 and is surrounded by porous py4	b.d.l.–4.46; mean: 0.80	+0.4–+8.7; mean: +5.2
Py4	Corroded porous py4 aggregates with micro inclusions	Early-ore stage S2	Overgrow and surround relics of py3 in the breccia A; overgrown by mc2 and mc3	b.d.l.–5.67; mean: 0.70	+1.2–+6.3; mean: +3.4
Mc2	Coarse-grained enhedra aggregates and inclusion-free	Early-ore stage S2	Aggregates in the calcite-quartz-sulfide cements of the breccias A; overgrows porous py4	b.d.l.–1.33; mean: 0.10	-1.2–+11.4; mean: +5.0
Mc3	Narrow high As bands in the outer rim of mc2	Main-ore stage S3	Overgrows mc2 and surrounds py4	b.d.l.–43.12; mean: 5.94	-21.1–-1.2; mean: -9.7
Py5a	Fine-grained framboids and zoned euhedra	Main-ore stage S3	Disseminations in the breccia A and aggregates in the cements of breccia B	b.d.l.–142.95; mean: 27.35	-13.9–+1.4; mean: -7.3
Py5b	Colloform aggregates with fine-grained uranium oxides	Main-ore stage S3	Aggregates in the cements of the breccia B and C; crosscut by py4, mc2 and mc3	b.d.l.–62.26; mean: 9.70	-9.9–-0.7; mean: -6.0
Py6	Coarse-grained euhedra	Late-ore stage S4	Occur in the latest coarse-grained calcite veins	b.d.l.–0.23; mean:0.05	-27.8–-8.3; mean: -19.5

Mc4	Coarse-grained euhedra	Late-ore stage S4	Occur in the latest coarse-grained calcite veins	b.d.l.	-31.3—22.6; mean: -26.3

b.d.l. = below detection limit

Table 2

TABLE 2. Summarized LA-ICP-MS Analyses of Pyrite and Marcsite Hosted by Sediments from Within and Outside the Ore Zone of the Daqiao Gold Deposit

	V	Cr	Mn	Co	Ni	Cu	Zn	As	Se	Mo	Ag	Cd	Sn	Sb	Te	W	Au	Hg	Tl	Pb	Bi
Py1 (n = 22)																					
Avg	b.d.l	11.2	32.9	330.4	458.9	19.7	14.7	566.0	1.9	31.1	1.4	b.d.l	0.4	119.3	b.d.l	0.3	0.1	0.5	1.8	250.3	11.4
Min		b.d.l	b.d.l	b.d.l	12.9	b.d.l	b.d.l	b.d.l	b.d.l	b.d.l	b.d.l		b.d.l	2.3		b.d.l	b.d.l	b.d.l	b.d.l	2.9	b.d.l
Max		57.8	240.1	1490.6	1559.4	72.8	126.1	1819.3	41.8	90.8	9.1		5.8	391.4		2.5	0.4	2.7	17.1	914.7	56.9
S.D.		17.9	49.1	412.1	486.5	20.2	33.2	438.5	8.7	28.6	2.4		1.3	114.9		0.7	0.1	1.0	4.0	235.2	15.2
Py2 (n = 30)																					
Avg	0.8	4.6	9.8	100.2	239.6	39.3	21.6	439.3	b.d.l	0.1	0.2	1.9	0.3	15.8	0.3	0.1	0.1	b.d.l	0.3	16.8	1.1
Min	b.d.l	b.d.l	b.d.l	b.d.l	b.d.l	b.d.l	b.d.l	b.d.l		b.d.l	b.d.l	b.d.l	b.d.l	b.d.l	b.d.l	b.d.l	b.d.l		b.d.l	b.d.l	b.d.l
Max	7.8	58.8	44.4	761.7	1748.7	951.6	416.8	1346.6		4.3	2.0	33.2	2.9	270.1	6.1	2.0	1.1		3.2	150.5	11.2
S.D.	1.9	13.0	8.5	161.3	395.9	170.5	84.3	364.8		0.8	0.5	7.2	0.8	49.0	1.2	0.4	0.3		0.7	34.2	2.7
Py3 (n = 26)																					
Avg	0.7	6.1	12.6	213.4	243.0	23.5	19.7	7294.0	17.2	1.4	0.6	14.8	0.6	16.0	1.4	0.7	0.8	2.2	0.2	20.2	1.0
Min	b.d.l	b.d.l	b.d.l	b.d.l	b.d.l	b.d.l	b.d.l	b.d.l	b.d.l	b.d.l	b.d.l	b.d.l	b.d.l	b.d.l	b.d.l	b.d.l	b.d.l	b.d.l	b.d.l	b.d.l	b.d.l
Max	9.9	63.1	52.4	1805.7	1679.2	259.3	511.6	87444.0	377.7	24.0	4.5	317.4	6.7	120.0	18.5	15.4	4.6	57.5	3.3	176.3	17.3
S.D.	2.2	15.8	12.5	426.0	362.6	60.6	98.4	17082.5	73.4	4.7	1.1	61.2	1.7	28.7	4.0	3.0	1.2	11.0	0.7	39.1	3.3
Py4 (n = 17)																					
Avg	3.9	8.9	17.0	24.2	58.3	90.1	146.7	789.9	7.3	1.0	7.1	6.5	1.2	116.1	0.6	0.5	0.7	6.6	8.5	42.2	0.9

Min	b.d.l	b.d.l	b.d.l	b.d.l	b.d.l	b.d.l	b.d.l	b.d.l	b.d.l	b.d.l	b.d.l	b.d.l	b.d.l	b.d.l	b.d.l	b.d.l	b.d.l	b.d.l	b.d.l	b.d.l	b.d.l
Max	19.7	36.5	73.1	190.2	428.4	385.7	1246.8	8031.4	124.4	3.6	78.0	40.2	9.9	660.0	6.2	7.4	5.7	61.2	62.9	246.4	7.6
S.D.	5.7	14.0	17.1	51.1	100.3	120.7	315.5	1921.0	29.3	1.8	18.5	14.2	2.7	165.0	1.6	1.8	1.4	15.2	16.1	65.4	1.8
Py5a (n = 14)																					
Avg	2.82	55.58	107.07	3.83	57.70	112.73	53.39	6131.0	b.d.l	9.51	93.75	7.69	1.13	1852.38	0.94	6.51	27.35	982.02	865.74	27.68	0.01
Min	b.d.l	b.d.l	b.d.l	b.d.l	b.d.l	b.d.l	b.d.l	b.d.l		b.d.l	b.d.l	b.d.l	b.d.l	b.d.l	b.d.l	b.d.l	b.d.l	b.d.l	b.d.l	b.d.l	b.d.l
Max	20.5	134.1	246.4	29.9	550.7	608.7	336.9	15399.1		36.3	400.2	39.2	6.9	10623.2	7.8	32.9	142.95	3475.0	3442.4	86.2	0.1
S.D.	5.4	37.9	61.2	8.1	145.2	188.5	105.8	4844.3		20.4	133.1	13.0	2.2	2651.7	2.4	10.6	46.7	1127.0	1083.0	33.6	0.0
Py5b (n = 13)																					
Avg	0.3	26.7	73.8	0.6	3.8	96.8	b.d.l	13569.2	b.d.l	1.3	0.5	b.d.l	0.6	1132.8	2.6	0.2	9.7	1087.3	1641.5	0.2	0.0
Min	b.d.l	b.d.l	b.d.l	b.d.l	b.d.l	b.d.l		b.d.l		b.d.l	b.d.l		b.d.l	b.d.l	b.d.l	b.d.l	b.d.l	b.d.l	b.d.l	b.d.l	b.d.l
Max	3.5	121.3	140.2	7.5	48.8	657.3		38583.7		10.5	2.7		5.4	2732.3	12.2	1.7	62.3	3161.4	>5000	0.9	0.3
S.D.	0.9	34.5	29.5	2.0	13.0	208.3		9346.6		2.9	0.9		1.6	822.2	4.2	0.5	16.8	976.7	1067.5	0.2	0.1
Py6 (n = 5)																					
Avg	4.2	b.d.l	76.5	127.7	444.1	306.4	131.2	241.5	b.d.l	b.d.l	0.2	b.d.l	b.d.l	16.6	5.1	0.3	0.0	b.d.l	b.d.l	15.8	7.7
Min	b.d.l		b.d.l	b.d.l	b.d.l	b.d.l	b.d.l	17.4			b.d.l			b.d.l	b.d.l	b.d.l	b.d.l			b.d.l	b.d.l
Max	11.5		270.4	382.5	787.5	1320.6	655.9	884.1			0.8			61.0	19.8	1.4	0.2			57.9	24.8
S.D.	5.2		99.8	131.9	243.0	511.0	262.4	324.5			0.3			23.6	7.7	0.6	0.1			22.1	9.9
Mc1 (n = 27)																					
Avg	2.1	10.2	45.9	4.4	67.8	10.4	7.1	26.2	b.d.l	0.2	0.1	0.6	0.5	29.9	0.6	10.1	0.0	3.7	3.7	10.1	0.0
Min	b.d.l	b.d.l	b.d.l	b.d.l	b.d.l	b.d.l	b.d.l	b.d.l		b.d.l	b.d.l	b.d.l	b.d.l	b.d.l	b.d.l	b.d.l	b.d.l	b.d.l	b.d.l	b.d.l	b.d.l
Max	22.0	129.6	894.0	81.0	658.7	62.1	191.5	223.4		4.7	1.6	15.9	7.9	126.2	5.0	131.8	0.2	39.8	22.2	59.6	0.3
S.D.	5.6	26.5	166.9	15.3	143.1	21.9	36.2	48.7		0.9	0.4	3.0	1.6	42.1	1.4	26.0	0.1	8.9	5.5	17.9	0.0
Mc2 (n = 30)																					
Avg	2.4	6.1	57.1	1.8	32.1	29.3	41.4	29.4	b.d.l	0.3	1.2	3.8	0.8	43.9	0.8	10.6	0.1	10.1	10.6	9.6	0.1
Min	b.d.l	b.d.l	b.d.l	b.d.l	b.d.l	b.d.l	b.d.l	b.d.l		b.d.l	b.d.l	b.d.l	b.d.l	b.d.l	b.d.l	b.d.l	b.d.l	b.d.l	b.d.l	b.d.l	b.d.l

Max	44.4	45.2	718.1	17.0	222.1	250.9	856.7	200.3		2.6	11.4	93.5	6.0	322.0	6.6	105.4	1.3	213.7	167.3	150.0	1.4
S.D.	8.1	14.0	161.4	3.8	52.2	69.4	159.5	45.0		0.7	2.2	17.0	1.8	78.9	1.9	26.5	0.3	39.0	33.3	27.6	0.3
Mc3 (n = 21)																					
Avg	7.8	54.1	72.2	3.3	22.9	43.0	46.0	1112.1	b.d.l	0.9	22.2	1.9	1.7	724.0	0.8	14.9	5.9	194.8	242.1	64.2	0.1
Min	b.d.l	b.d.l	b.d.l	b.d.l	b.d.l	b.d.l	b.d.l	b.d.l		b.d.l	b.d.l	b.d.l	b.d.l	b.d.l	b.d.l	b.d.l	b.d.l	b.d.l	b.d.l	b.d.l	b.d.l
Max	69.3	617.6	764.7	38.7	144.6	195.93	519.4	4769.34		5.0	219.5	40.1	9.8	3990.1	9.2	80.2	43.12	1629.2	865.3	720.7	1.7
S.D.	16.7	136.5	160.9	8.7	39.0	58.1	126.3	1296.6		1.6	48.1	8.5	2.6	971.9	2.3	23.4	12.3	359.3	281.6	159.4	0.4
Mc4 (n = 12)																					
Avg	b.d.l	1.4	7.7	0.2	b.d.l	8.1	b.d.l	30.8	b.d.l	b.d.l	0.3	b.d.l	b.d.l	0.4	0.4	0.6	b.d.l	b.d.l	1.0	0.1	0.0
Min		b.d.l	b.d.l	b.d.l		b.d.l		b.d.l			b.d.l			b.d.l	b.d.l	b.d.l			b.d.l	b.d.l	b.d.l
Max		17.0	17.0	2.3		55.2		95.9			2.7			1.1	5.3	3.7			9.5	0.7	0.2
S.D.		4.7	5.5	0.6		18.4		32.8			0.8			0.4	1.5	1.2			2.6	0.2	0.0

b.d.l = below detection limit; S.D. = standard deviation

Table 3

TABLE 3. LA-MC-ICPMS In Situ Sulfur Isotope Composition of Different Sulfide Types from the Daqiao Gold Deposit

Sample no.	Sulfide	^{32}S (V)	δ^{34}S‰ CDT	2σ	Sample no.	Sulfide	^{32}S (V)	δ^{34}S‰ CDT	2σ	Sample no.	Sulfide	^{32}S (V)	δ^{34}S‰ CDT	2σ
DQ200-3	Py1	0.84	-0.1	0.2	DQ164-4	py4	0.93	4.7	0.2	DQ211-11	Mc1	0.98	1.2	0.2
DQ168-2		1.01	-30.9	0.2	DQ108-3		0.89	2.1	0.3	DQ211-5		0.96	3.2	0.3
DQ168-2		0.93	5.9	0.2	DQ108-3		0.73	4.1	0.3	DQ211-5		0.88	-0.1	0.3
DQ164-6		0.85	-6.9	0.3	DQ164-4		0.90	6.2	0.3	DQ185-4		1.03	-5.8	0.3

DQ168-7		0.64	6.7	0.4	DQ208-6		1.10	3.2	0.4	DQ185-4		1.05	3.5	0.2
DQ200-3		1.05	-1.0	0.3	DQ113-11		0.71	3.6	0.3	DQ185-4		0.90	-2.5	0.2
DQ200-11		1.05	0.9	0.2	DQ113-11		0.92	3.0	0.3	DQ185-10		1.01	-0.1	0.7
DQ113-8		0.80	15.7	0.2	DQ108-6		1.05	1.2	0.3	DQ219-5		1.01	-1.2	0.2
DQ113-8		0.90	22.0	0.2	DQ108-6		0.51	2.7	0.5	DQ219-5		1.03	-1.2	0.2
DQ168-5		0.94	2.6	0.2	DQ97-1		0.93	1.4	0.3	DQ222-2		0.99	0.5	0.3
DQ164-4		0.98	3.8	0.2	DQ97-1		0.72	-3.5	0.3	DQ216-3		0.82	-6.2	0.5
DQ164-4		1.05	3.2	0.3	DQ97-1	Py5a	0.98	-13.9	0.2	DQ200-13		0.94	2.2	0.2
DQ218-12		1.04	6.6	0.2	DQ97-2		0.87	-5.5	0.3	DQ191-7		1.03	-4.1	0.3
DQ185-5		0.96	-6.2	0.2	DQ97-2		1.00	-12.3	0.4	DQ194-6		1.03	-1.6	0.2
DQ185-8		0.98	2.6	0.3	DQ97-5		1.04	-9.8	0.3	DQ194-6		0.99	-1.7	0.2
DQ168-2	Py2	0.99	4.9	0.2	DQ224-4		1.05	-2.2	0.3	DQ107-9		0.89	1.7	0.2
DQ168-5		0.82	4.5	0.3	DQ224-4		0.97	-7.5	0.3	DQ107-9		0.97	0.8	0.2
DQ168-7		0.80	5.9	0.3	DQ224-4		1.02	-6.2	0.3	DQ107-1		0.89	2.2	0.3
DQ107-1		0.96	13.1	0.3	DQ224-6		1.06	-0.7	0.2	DQ107-2		0.96	8.6	0.2
DQ185-1		1.01	-1.4	0.3	DQ224-6		1.00	-5.8	0.2	DQ107-2		1.00	1.2	0.2
DQ185-6		0.97	3.6	0.3	DQ224-8	Py5b	1.04	-5.2	0.3	DQ107-5		0.88	2.0	0.4
DQ185-6		0.88	3.0	0.3	DQ224-8		1.07	-4.8	0.3	DQ107-5	Mc2	0.87	-1.1	0.3
DQ185-10		1.05	4.2	0.2	DQ93-1		1.10	-9.1	0.2	DQ208-4		0.88	9.7	0.3
DQ51-1		0.72	2.0	0.3	DQ93-1		1.05	-3.1	0.2	DQ208-12		0.89	8.7	0.4
DQ51-2		0.81	3.1	0.3	DQ93-3		1.16	-9.3	0.2	DQ208-15		0.89	11.4	0.4
DQ51-3		0.87	2.4	0.2	DQ93-7		1.10	-9.9	0.2	DQ209-15		0.99	0.8	0.6
DQ51-4		0.96	-2.8	0.7	DQ220-1		0.92	-7.9	0.2	DQ164-12		0.69	6.2	0.3
DQ219-7	Py3	0.94	2.3	0.3	DQ228-2	Py6	1.03	-18.3	0.2	DQ164-12		1.09	3.7	0.2
DQ219-7		1.06	5.7	0.4	DQ228-6		1.14	-17.9	0.2	DQ194-3		0.88	7.8	0.3

DQ219-12		0.99	5.1	0.3	DQ228-6		0.98	-25.3	0.2	DQ220-1		1.06	7.4	0.3
DQ219-14		0.80	3.8	0.5	DQ228-8		0.98	-8.3	0.2	DQ220-1		1.04	11.1	0.3
DQ219-14		0.99	4.0	0.3	DQ228-8		0.88	-27.8	0.2	DQ51-5		0.95	2.6	0.3
DQ220-1		1.15	8.3	0.4	DQ200-11		0.77	3.2	0.3	DQ107-2		1.07	-1.2	0.2
DQ168-2		0.85	4.6	0.2	DQ200-3		0.86	2.1	0.2	DQ208-4		0.91	-11.7	0.3
DQ216-1		0.59	7.9	0.3	DQ185-5		0.99	4.9	0.2	DQ208-12	Mc3	1.00	-8.5	0.4
DQ216-2		0.52	6.5	0.8	DQ185-8		0.97	3.8	0.3	DQ194-3		0.84	-10.2	0.2
DQ216-3		0.78	8.7	0.3	DQ191-7		0.99	-1.9	0.3	DQ209-8		1.00	-21.1	0.9
DQ216-4		0.71	6.6	0.3	DQ194-3		0.98	0.1	0.3	DQ220-1		0.79	-5.2	0.3
DQ216-6		0.58	7.0	0.3	DQ194-3	Mc1	0.98	-0.7	0.3	DQ107-5		1.01	-30.6	0.7
DQ216-7		0.70	7.9	0.3	DQ194-6		0.88	-1.6	0.3	DQ107-5		0.94	-22.6	0.3
DQ208-6		0.69	4.5	0.3	DQ194-6		0.95	-0.5	0.5	DQ107-5	Mc4	0.98	-31.3	0.6
DQ200-1		1.00	0.4	0.2	DQ218-13		0.92	-7.7	0.5	DQ110-3		0.94	-23.7	0.3
DQ200-1		0.94	0.5	0.2	DQ218-8		1.01	-7.5	0.2	DQ110-3		1.01	-23.3	0.3
DQ200-13		1.05	4.4	0.4	DQ218-8		0.96	-5.1	0.2					
DQ113-12	Py4	0.77	3.3	0.3	DQ218-12		1.07	-0.4	0.2					
DQ113-12		0.93	3.3	0.2	DQ211-11		0.96	1.0	0.2					

Table 4

TABLE 4. Relevant Parameters of Raman Spectra and Estimated Temperatures of Samples Investigated at the Daqiao Gold Deposit

Sample no.	Analysis no.	D position (cm^{-1})	D width (HWHM) (cm^{-1})	G position (cm^{-1})	G width (HWHM) (cm^{-1})	ID	IG	AD	AD1	AD2	AG	AS1	AS2	AS3	R1	R2	R3	R4	T_R(℃)
DQ222	222-1	1348.4	34.7	1598.2	27.3	5506.7	2790.7	600447.9	37526.0	54690.4	238984.7	68127.1	58656.2	8854.4	1.97	1.27	0.68	0.50	326
DQ222	222-2	1346.7	35.0	1600.9	24.9	4985.6	2712.6	547861.2	40712.6	73925.9	211849.6	78275.1	62807.0	6963.6	1.84	1.41	0.67	0.53	336
DQ222	222-3	1344.8	36.6	1603.2	30.3	4386.5	2348.8	503742.3	35072.1	48429.3	223234.1	68069.2	64343.7	7119.1	1.87	1.21	0.66	0.49	346
DQ222	222-4	1348.7	32.1	1601.2	23.6	6271.0	2828.9	632357.9	45631.2	72152.4	209448.7	114132.1	57712.6	10841.8	2.22	1.36	0.71	0.62	299
DQ222	222-5	1345.2	30.3	1603.6	20.8	6675.9	3273.1	634479.9	60987.5	114693.5	213860.7	107752.4	79021.8	10500.6	2.04	1.46	0.68	0.55	332
DQ222	222-8	1349.1	38.1	1601.2	32.5	6191.0	3347.2	740938.5	24764.9	42751.9	341685.9	58099.6	64306.9	7321.2	1.85	1.17	0.67	0.45	345
DQ222	222-11	1351.5	40.1	1609.2	26.9	2192.9	1228.4	281738.8	16565.0	30452.2	103771.4	30214.4	33674.8	5918.5	1.79	1.49	0.69	0.43	317
DQ222	222-12	1349.7	30.3	1604.5	30.3	7502.6	3382.5	713049.6	78361.6	95644.4	321470.0	126010.7	88047.6	15984.6	2.22	1.00	0.65	0.55	354
DQ222	222-13	1345.6	36.6	1600.8	27.1	6503.1	3223.3	746816.7	30144.6	38770.2	274430.5	101598.4	78555.7	19639.6	2.02	1.35	0.71	0.51	296
DQ222	222-14	1351.9	33.4	1604.0	27.1	4100.3	2061.8	430286.7	30331.9	40718.2	175541.1	72560.6	52792.5	8536.5	1.99	1.23	0.68	0.54	330
DQ222	222-15	1348.7	36.6	1600.8	27.1	6604.6	3244.5	758470.7	25235.8	45798.5	276237.4	88471.6	77891.8	12873.7	2.04	1.35	0.71	0.49	300
DQ222	222-16	1351.9	30.3	1600.8	23.9	8309.3	3797	789709.9	62486.5	80649.5	285688.6	127522.0	102591.1	21442.0	2.19	1.27	0.70	0.51	307
DQ224	224-1	1348.7	30.3	1597.7	27.1	6376.5	3182.3	606020.5	87476.5	90978.7	270938.0	108759.9	74672.3	19241.7	2.00	1.12	0.66	0.54	355
DQ224	224-2	1351.9	39.7	1600.8	23.9	5985.0	3563	746569.5	35674.9	40180.9	286083.0	92268.8	80267.7	9917.3	1.68	1.66	0.71	0.51	296
DQ224	224-3	1346.4	42.9	1597.7	27.1	4557.0	2400.3	613556.3	24423.1	42216.4	204357.3	63107.7	62763.4	10209.0	1.90	1.58	0.72	0.46	286
DQ224	224-4	1348.7	36.6	1599.1	26.0	6704.5	3589.2	769940.3	30998.2	42481.8	293254.6	107338.9	77548.3	13548.2	1.87	1.41	0.70	0.54	304
DQ224	224-5	1351.9	42.9	1600.8	23.9	4194.8	2305.2	564792.7	23434.6	78612.8	173446.1	53245.3	57339.9	4823.4	1.82	1.79	0.70	0.46	307
DQ224	224-6	1345.6	30.3	1602.0	23.5	8407.3	3806	799032.5	47554.1	94806.6	280660.2	95422.6	86170.6	15368.2	2.21	1.29	0.69	0.48	314

DQ224	224-7	1346.7	36.6	1595.9	28.4	5621.1	2717.5	645530.6	39329.7	74183.1	242629.8	74394.4	56893.4	9220.9	2.07	1.29	0.68	0.53	327
DQ224	224-8	1351.4	33.4	1599.9	30.3	6390.6	2855.4	670626.2	33324.2	37671.8	271378.3	89061.1	68267.6	8017.8	2.24	1.10	0.69	0.54	310
DQ224	224-10	1346.3	36.6	1598.4	25.0	5219.8	2598.1	599443.2	48346.2	101608.3	204305.3	77934.6	66444.1	11199.8	2.01	1.46	0.68	0.50	332
DQ224	224-11	1348.7	30.3	1597.4	27.0	5595.5	2894.2	531795.6	34091.7	30893.2	245575.2	90323.6	63286.6	8651.9	1.93	1.12	0.67	0.56	339
DQ224	224-12	1348.7	30.3	1604.0	27.1	6297.1	3388.3	598477.7	56605.4	37196.7	288476.2	87210.3	80229.2	8875.5	1.86	1.12	0.67	0.49	342
DQ224	224-13	1351.5	42.9	1603.6	23.9	4060.2	2174.2	546663.1	22648.5	53963.5	163583.2	52029.7	53592.0	5296.4	1.87	1.79	0.72	0.47	283
DQ224	224-14	1346.6	42.9	1605.0	27.1	3795.3	2246.4	511004.1	27332.8	56822.6	191257.1	49153.5	63264.5	4977.0	1.69	1.58	0.68	0.42	319
DQ224	224-15	1349.8	30.4	1600.8	25.1	5861.7	3044.2	560190.7	74546.1	71359.4	239935.8	83208.8	80396.2	7924.9	1.93	1.21	0.67	0.49	340

HWHM = half width at half maximum

Table A1

TABLE A1. LA-ICP-MS Analyses of Pyrite and Marcasite Hosted by Sediments from Within and Outside the Ore Zone of the Daqiao Gold Deposit

Sample no.	Analysis no.	Sulfide	V	Cr	Mn	Co	Ni	Cu	Zn	As	Se	Mo	Ag	Cd	Sn	Sb	Te	W	Au	Hg	Tl	Pb	Bi
AZS-1-1	02-24-15 01 104		0.00	0.00	93.49	2.95	12.86	0.00	0.00	136.90	0.00	21.59	0.00	0.00	0.00	2.71	0.00	0.65	0.00	0.00	2.07	4.62	0.00
AZS-1-2	02-24-15 01 105		0.00	18.45	17.36	4.74	18.24	39.30	0.00	225.85	0.00	21.84	0.00	0.00	0.00	2.33	0.00	0.00	0.00	0.00	0.58	5.99	0.00
AZS-1-3	02-24-15 01 106		0.00	0.00	38.06	0.00	16.56	55.01	0.00	172.66	0.00	12.21	0.00	0.00	0.00	21.57	0.00	0.00	0.00	0.00	1.36	10.29	0.00
AZS-1-3	02-24-15 01 107		0.00	0.00	240.13	4.57	55.00	0.00	0.00	241.54	0.00	76.11	0.00	0.00	0.00	7.54	0.00	0.00	0.00	0.00	3.55	2.94	0.00
DQ-28	12-15-15 01 26		0.00	45.95	23.08	72.92	131.78	38.57	0.00	626.40	0.00	84.97	0.00	0.00	0.00	322.89	0.00	0.00	0.00	0.00	0.97	380.40	1.60
DQ-28	12-15-15 01 27		0.00	23.13	20.38	46.63	103.95	39.33	0.00	516.56	0.00	23.15	0.00	0.00	0.00	391.44	0.00	0.00	0.00	0.00	0.00	466.54	2.98
DQ-28	12-15-15 01 28		0.00	38.49	53.62	87.62	102.88	20.67	126.06	320.53	0.00	0.00	0.00	0.00	0.00	177.35	0.00	0.00	0.34	0.00	0.00	243.33	1.92
DQ-28	12-15-15 01 29		0.00	29.41	17.46	19.31	146.58	21.98	96.70	361.74	0.00	13.12	0.00	0.00	0.00	268.09	0.00	0.00	0.00	1.94	0.38	309.90	2.06
DQ-347	12-15-15 01 16		0.00	0.00	12.89	721.12	1024.95	72.83	0.00	859.67	0.00	68.34	0.00	0.00	0.00	184.59	0.00	2.38	0.00	0.00	0.00	363.15	24.71
DQ-347	12-15-15 01 17		0.00	57.84	25.13	708.92	928.27	10.33	0.00	912.01	0.00	56.13	7.11	0.00	0.00	133.97	0.00	0.00	0.00	0.00	0.00	283.86	21.25
DQ-347	12-15-15 01 18	Py1	0.00	0.00	23.87	759.62	783.38	9.07	0.00	774.07	0.00	37.27	3.59	0.00	0.00	138.35	0.00	0.00	0.00	2.62	0.53	204.33	18.81
DQ-347	12-15-15 01 19		0.00	0.00	19.50	707.96	801.59	11.96	22.60	776.91	0.00	90.77	2.77	0.00	0.00	127.93	0.00	2.48	0.37	0.00	0.70	228.79	18.95
DQ-347	12-15-15 01 20		0.00	0.00	26.61	601.17	812.30	11.79	0.00	937.92	41.82	62.04	0.00	0.00	0.00	116.55	0.00	0.00	0.00	0.00	0.98	914.70	14.36
DQ-360	12-15-15 01 21		0.00	0.00	0.00	1490.59	1090.63	45.27	27.95	1819.31	0.00	32.59	9.14	0.00	0.00	272.22	0.00	0.00	0.41	0.00	0.83	591.61	56.94
DQ-360	12-15-15 01 22		0.00	0.00	16.72	829.19	1174.51	27.57	49.10	1131.15	0.00	17.33	3.57	0.00	0.00	199.20	0.00	0.00	0.00	1.55	0.93	442.89	37.57
DQ-360	12-15-15 01 23		0.00	0.00	11.81	197.83	185.53	5.71	0.00	357.49	0.00	10.78	0.00	0.00	0.00	49.20	0.00	0.00	0.00	2.45	10.59	371.45	10.01
DQ-360	12-15-15 01 24		0.00	0.00	21.45	102.24	1559.41	5.81	0.00	306.98	0.00	20.98	0.00	0.00	5.79	20.78	0.00	0.00	0.00	2.73	17.10	88.78	2.56
DQ-360	12-15-15 01 25		0.00	0.00	27.26	834.44	946.76	17.23	0.00	1200.58	0.00	35.90	2.50	0.00	0.00	154.27	0.00	0.00	0.00	0.00	0.00	486.57	34.69
DQ200-3	02-25-15 01 28		0.00	0.00	12.18	66.04	47.55	0.00	0.00	490.40	0.00	0.00	0.82	0.00	0.00	5.05	0.00	1.02	0.00	0.00	0.00	8.35	1.21
DQ168-2	02-25-15 01 15		0.00	0.00	11.46	5.17	118.68	0.00	0.00	0.00	0.00	0.00	0.82	0.00	0.00	8.59	0.00	0.00	0.00	0.00	0.00	7.78	0.00
DQ168-2	02-25-15 01 16		0.00	0.00	11.72	6.71	22.05	0.00	0.00	0.00	0.00	0.00	0.00	0.00	3.02	4.05	0.00	0.00	0.00	0.00	0.00	19.55	1.22

DQ164-6	02-24-15 01 74		0.00	33.69	0.00	0.00	13.20	0.00	0.00	282.93	0.00	0.00	1.28	0.00	0.00	15.46	0.00	0.00	0.00	0.00	0.00	71.23	0.49
DQ200-3	02-25-15 01 29		0.00	0.00	9.74	6.17	50.18	0.00	0.00	554.33	0.00	0.00	0.00	0.00	2.49	0.61	0.00	0.00	0.00	0.00	0.00	0.67	0.27
DQ200-11	02-25-15 01 31		0.00	0.00	6.79	0.00	0.00	0.00	0.00	1006.88	0.00	0.00	0.00	0.00	0.00	0.00	0.00	0.00	0.00	0.00	0.00	0.00	0.00
DQ113-8	02-25-15 01 11		0.00	0.00	11.51	9.47	0.00	0.00	0.00	884.94	0.00	0.00	0.00	0.00	2.70	6.02	3.29	0.00	0.41	0.00	0.19	17.95	6.70
DQ113-8	02-25-15 01 12		0.00	0.00	8.55	3.93	11.40	0.00	0.00	325.06	0.00	0.00	0.00	0.00	0.00	0.00	0.00	0.00	0.00	0.00	0.00	0.26	0.15
DQ168-5	02-25-15 01 17		0.00	0.00	9.59	38.82	131.25	0.00	0.00	0.00	0.00	0.00	0.00	0.00	0.00	0.98	0.00	0.00	0.00	0.00	0.00	11.68	0.14
DQ164-6	02-24-15 01 75		0.00	0.00	44.38	37.98	138.20	55.60	0.00	92.92	0.00	0.00	0.00	0.00	0.00	270.11	0.00	0.00	0.00	0.00	0.73	113.28	0.39
DQ164-4	02-24-15 01 50		0.00	22.50	8.92	0.00	55.02	70.96	0.00	45.91	0.00	0.00	0.00	0.00	2.94	44.83	0.00	0.00	0.21	0.00	0.00	24.08	0.00
DQ164-4	02-24-15 01 52		0.00	0.00	15.51	0.00	0.00	0.00	0.00	81.39	0.00	0.00	0.00	0.00	0.00	31.94	0.00	0.00	0.92	0.00	3.16	61.91	0.00
DQ216-4	02-24-15 01 117		3.74	0.00	15.37	161.29	423.21	0.00	0.00	551.79	0.00	0.00	0.00	0.00	0.00	8.81	0.00	0.00	0.00	0.00	0.00	10.42	0.28
DQ218-12	02-24-15 01 65		0.00	0.00	8.97	23.70	117.91	0.00	0.00	347.47	0.00	0.00	0.00	0.00	0.00	1.79	0.00	0.00	0.00	0.00	0.00	0.79	0.00
DQ218-2	02-24-15 01 99		4.25	0.00	14.05	57.61	394.79	54.57	0.00	516.62	0.00	0.00	0.00	0.00	0.00	0.55	0.00	0.00	0.00	0.00	0.14	0.68	0.00
DQ117-1	02-25-15 01 156	Py2	0.00	0.00	0.00	286.43	821.66	0.00	0.00	888.45	0.00	0.00	0.85	0.00	0.00	17.89	0.00	0.00	0.00	0.00	0.28	27.97	2.50
DQ30-1	02-25-15 01 188		0.00	0.00	0.00	153.64	24.54	0.00	0.00	54.04	0.00	0.00	0.84	0.00	0.00	1.90	0.00	0.00	0.00	0.00	0.00	4.22	0.00
DQ185-5	02-24-15 01 82		0.00	0.00	8.23	0.00	0.00	0.00	0.00	49.26	0.00	0.00	0.00	0.00	0.00	7.64	0.00	0.00	0.00	0.00	2.27	14.88	0.00
DQ185-8	02-24-15 01 83		7.80	58.83	11.97	35.07	83.52	0.00	416.76	82.30	0.00	4.28	0.00	24.07	0.00	48.21	6.05	1.44	0.00	0.00	1.15	150.48	8.92
DQ175-1	02-24-15 01 112		0.00	0.00	17.74	761.73	1748.70	0.00	0.00	1346.55	0.00	0.00	0.76	0.00	0.00	0.00	0.00	0.00	0.00	0.00	0.00	0.41	0.00
DQ175-1	02-24-15 01 113		0.00	0.00	10.63	1.97	45.57	0.00	0.00	265.73	0.00	0.00	0.00	0.00	0.00	0.00	0.00	0.00	0.00	0.00	0.11	1.55	0.00
DQ175-2	02-24-15 01 114		0.00	0.00	0.00	24.20	17.03	0.00	0.00	53.65	0.00	0.00	0.00	0.00	0.00	2.86	0.00	0.00	0.00	0.00	0.00	10.32	0.00
DQ124-3	02-25-15 01 149		5.27	0.00	7.28	258.17	251.20	0.00	0.00	392.32	0.00	0.00	0.00	0.00	0.00	0.97	0.00	0.00	0.00	0.00	0.00	2.33	0.95
DQ100-4	02-25-15 01 152		0.00	35.28	0.00	8.56	47.85	45.41	231.71	1261.91	0.00	0.00	2.00	0.00	0.00	25.15	0.00	2.03	1.11	0.00	0.00	45.51	0.59
DQ71-1-1	02-25-15 01 189		0.00	0.00	7.39	135.46	146.67	0.00	0.00	321.22	0.00	0.00	0.00	0.00	0.00	0.00	0.00	0.00	0.00	0.00	0.00	0.00	0.00
DQ71-2-6	02-25-15 01 195		0.00	0.00	12.36	135.18	344.99	0.00	0.00	338.10	0.00	0.00	0.00	0.00	0.00	0.00	0.00	0.00	0.00	0.00	0.00	0.61	0.00
DQ71-2-6	02-25-15 01 196		0.00	0.00	0.00	6.23	16.84	0.00	0.00	662.03	0.00	0.00	0.00	0.00	0.00	0.59	0.00	0.00	0.00	0.00	0.00	1.03	0.15
DQ18-1	02-24-15 01 166		0.00	22.35	18.25	2.91	104.63	0.00	0.00	157.80	0.00	0.00	0.00	0.00	0.00	0.00	0.00	0.00	0.00	0.00	0.00	0.51	0.00

DQ209-4	02-26-15 01 208		0.00	0.00	6.82	0.00	26.21	0.00	0.00	0.00	0.00	0.00	0.49	0.00	0.00	0.00	0.00	0.00	0.00	0.00	0.08	0.00	0.00
DQ75-3	02-24-15 01 121		0.00	0.00	11.14	15.61	137.62	0.00	0.00	462.01	0.00	0.00	0.00	0.00	0.00	0.00	0.00	0.00	0.00	0.00	0.00	0.00	0.00
DQ75-3	02-24-15 01 122		0.00	0.00	14.57	43.30	67.73	951.58	0.00	512.36	0.00	0.00	2.01	33.23	0.00	1.23	0.00	0.00	0.00	0.00	0.00	3.37	11.21
DQ75-3	02-24-15 01 123		3.60	0.00	12.81	97.29	102.89	0.00	0.00	648.69	0.00	0.00	0.00	0.00	0.00	0.61	0.00	0.00	0.00	0.00	0.00	0.00	0.67
DQ72-1	02-25-15 01 145		0.00	0.00	0.00	357.73	569.75	0.00	0.00	502.56	0.00	0.00	0.00	0.00	0.00	0.49	0.00	0.00	0.00	0.00	0.00	0.22	0.00
DQ72-4	02-25-15 01 147		0.00	0.00	0.00	342.98	1309.75	0.00	0.00	772.78	0.00	0.00	0.00	0.00	0.00	0.85	0.00	0.00	0.00	0.00	0.22	0.20	0.00
DQ216-3	02-24-15 01 115		5.06	0.00	42.33	4.71	0.00	0.00	0.00	1918.63	0.00	0.00	2.72	0.00	0.00	7.41	0.00	1.04	0.54	0.00	0.37	6.71	0.00
DQ216-3	02-24-15 01 116		0.00	0.00	5.86	158.26	732.95	0.00	0.00	1427.41	0.00	0.00	0.00	0.00	0.00	3.39	0.00	0.00	0.37	0.00	0.00	6.22	0.00
DQ218-1	02-24-15 01 98		0.00	0.00	7.76	759.63	694.71	0.00	0.00	1548.99	0.00	2.22	0.00	0.00	0.00	1.99	0.00	0.00	0.00	0.00	0.00	1.22	0.00
DQ218-3	02-24-15 01 100		3.69	63.07	6.71	33.88	85.21	0.00	0.00	5024.02	0.00	0.00	0.00	0.00	0.00	3.11	0.00	0.00	0.00	0.00	0.00	12.79	0.17
DQ218-3	02-24-15 01 101		0.00	18.02	16.25	166.28	312.72	0.00	0.00	461.65	0.00	0.00	0.00	0.00	0.00	0.00	0.00	0.00	0.00	0.00	0.00	0.85	0.00
DQ219-7	02-24-15 01 86		9.90	0.00	43.05	31.38	89.17	139.35	0.00	0.00	0.00	5.76	0.00	42.36	6.68	65.01	9.74	1.66	0.32	0.00	0.00	6.05	0.00
DQ219-7	02-24-15 01 87		0.00	33.75	5.78	1805.65	1679.19	0.00	0.00	3115.07	0.00	0.00	0.00	0.00	0.00	1.67	0.00	0.00	0.00	0.00	0.00	2.40	0.45
DQ220-1	02-24-15 01 45		0.00	0.00	11.73	882.64	789.16	0.00	0.00	2357.33	0.00	0.00	0.00	0.00	0.00	1.11	0.00	0.00	0.00	0.00	0.00	0.96	0.00
DQ198-1	02-24-15 01 131		0.00	0.00	6.56	0.00	0.00	0.00	0.00	1308.73	0.00	0.00	0.00	0.00	0.00	19.64	0.00	0.00	0.00	0.00	0.00	6.23	0.00
DQ65-1	02-25-15 01 153	Py3	0.00	0.00	9.03	232.14	21.57	0.00	0.00	732.71	0.00	0.00	0.00	0.00	0.00	3.72	0.00	0.00	2.19	0.00	0.00	0.93	1.22
DQ211-1	02-24-15 01 109		0.00	0.00	52.36	0.00	89.42	0.00	0.00	945.48	377.68	23.98	1.89	317.37	0.00	119.96	0.00	15.41	4.64	57.45	3.33	85.82	0.00
DQ117-1	02-25-15 01 157		0.00	0.00	6.13	70.22	283.77	0.00	0.00	1203.09	0.00	0.00	2.29	24.49	0.00	74.84	4.87	0.00	1.28	0.00	0.88	85.56	2.69
DQ71-2-6	02-25-15 01 197		0.00	0.00	7.86	0.00	24.28	0.00	0.00	28385.32	0.00	0.00	0.00	0.00	0.00	4.02	0.00	0.00	0.60	0.00	0.00	3.75	0.00
DQ168-5	02-25-15 01 18		0.00	0.00	13.50	0.00	35.92	0.00	0.00	14235.71	70.74	0.00	0.90	0.00	0.00	9.98	0.00	0.00	1.43	0.00	0.00	19.91	0.00
DQ72-1	02-25-15 01 144		0.00	0.00	13.47	46.24	120.11	0.00	0.00	1939.02	0.00	0.00	0.00	0.00	0.00	0.45	0.00	0.00	0.00	0.00	0.00	1.15	0.00
DQ72-4	02-25-15 01 146		0.00	0.00	5.99	2.20	40.26	0.00	0.00	2209.37	0.00	0.00	0.00	0.00	0.00	1.35	0.00	0.91	0.19	0.00	0.00	5.63	0.00
DQ124-3	02-25-15 01 148		0.00	0.00	12.99	1074.61	130.14	0.00	0.00	947.22	0.00	3.74	1.19	0.00	0.00	19.03	0.00	0.00	0.29	0.00	0.00	54.43	17.28
DQ124-3	02-25-15 01 150		0.00	0.00	6.46	22.50	282.97	0.00	0.00	920.04	0.00	0.00	4.46	0.00	3.03	4.64	18.47	0.00	0.28	0.00	0.00	19.47	1.33
DQ100-4	02-25-15 01 151		0.00	44.60	5.99	0.00	20.27	259.25	511.55	87443.95	0.00	1.64	0.00	0.00	5.26	52.41	0.00	0.00	4.39	0.00	0.00	176.28	2.10

DQ71-2-4	02-25-15 01 192		0.00	0.00	6.50	77.53	176.15	0.00	0.00	2295.87	0.00	0.00	0.00	0.00	0.00	0.00	0.00	0.00	0.53	0.00	0.00	0.00	0.00
DQ71-2-4	02-25-15 01 193		0.00	0.00	8.96	67.51	230.03	121.16	0.00	6411.72	0.00	0.00	0.00	0.00	0.00	2.32	3.73	0.00	0.98	0.00	0.00	4.74	0.00
DQ71-2-4	02-25-15 01 194		0.00	0.00	5.89	14.71	91.04	92.12	0.00	12842.61	0.00	0.00	2.33	0.00	0.00	8.19	0.00	0.00	1.60	0.00	0.00	17.70	0.18
DQ181-2	02-25-15 01 181		0.00	0.00	8.40	26.46	79.58	0.00	0.00	2418.03	0.00	0.00	0.00	0.00	0.00	0.48	0.00	0.00	1.04	0.00	0.00	0.00	0.00
DQ181-2	02-25-15 01 182		0.00	0.00	8.07	0.00	37.49	0.00	0.00	2814.54	0.00	0.00	0.00	0.00	0.00	6.64	0.00	0.00	0.24	0.00	0.00	1.90	0.38
DQ181-2	02-25-15 01 183		0.00	0.00	0.00	24.72	271.04	0.00	0.00	4770.97	0.00	0.00	0.00	0.00	0.00	4.70	0.00	0.00	0.29	0.00	0.00	3.85	0.40
DQ123-1	02-25-15 01 177		0.00	0.00	11.00	45.98	0.00	0.00	0.00	1967.34	0.00	0.00	0.00	0.00	0.00	0.00	0.00	0.00	0.52	0.00	0.00	0.00	0.00
DQ65-1	02-25-15 01 154		0.00	33.57	0.00	0.00	17.14	0.00	180.93	347.39	0.00	0.00	4.50	0.00	0.00	127.85	0.00	0.00	0.00	0.00	2.86	6.59	0.00
DQ211-1	02-24-15 01 108		0.00	0.00	6.24	190.23	428.35	115.05	1246.81	130.16	0.00	6.31	0.00	0.00	5.08	167.14	0.00	0.00	0.61	0.00	3.03	172.07	7.60
DQ198-1	02-24-15 01 130		3.82	26.92	16.88	0.00	24.40	52.97	0.00	239.67	0.00	0.00	0.00	0.00	0.00	69.19	0.00	0.00	0.00	0.00	2.18	2.11	0.00
DQ198-1	02-24-15 01 132		3.30	28.12	35.80	22.08	19.56	0.00	0.00	2806.89	0.00	0.00	0.00	40.16	0.00	214.94	0.00	0.00	0.34	0.00	2.17	64.13	0.51
DQ113-12	02-25-15 01 13		19.65	0.00	25.34	15.47	98.80	154.22	0.00	228.68	0.00	0.00	6.54	39.70	0.00	48.04	0.00	0.00	1.58	3.92	3.69	22.90	0.57
DQ113-12	02-25-15 01 14		5.26	0.00	18.97	15.11	79.78	356.36	0.00	568.76	0.00	0.00	78.03	0.00	9.90	660.04	0.00	7.35	5.67	7.66	31.82	246.43	1.03
DQ97-2	02-24-15 01 169		0.00	0.00	73.05	0.00	7.52	0.00	0.00	45.95	0.00	0.00	0.00	0.00	0.00	17.45	0.00	0.00	0.00	61.77	62.89	0.00	0.00
DQ30-1	02-25-15 01 187		6.19	0.00	7.53	0.00	17.94	65.87	183.87	8031.41	0.00	0.00	0.00	0.00	0.00	1.17	0.00	0.00	0.00	2.82	0.00	1.02	0.00
DQ164-4	02-24-15 01 51	Py4	0.00	26.38	8.35	0.00	0.00	39.03	0.00	0.00	0.00	0.00	0.00	0.00	0.00	74.71	0.00	0.00	0.00	0.00	0.46	63.20	0.00
DQ164-4	02-24-15 01 73		15.73	0.00	25.85	129.06	140.61	236.60	595.02	42.13	0.00	2.85	2.16	31.40	0.00	1.91	0.00	0.00	0.00	6.63	0.00	14.44	1.47
DQ228-2	02-24-15 01 97		0.00	36.48	18.06	4.44	46.16	74.61	287.90	516.01	0.00	3.41	2.25	0.00	0.00	194.20	0.00	0.00	0.74	26.47	21.70	40.39	2.44
DQ117-1	02-25-15 01 155		9.12	0.00	10.72	0.00	0.00	51.99	0.00	333.80	0.00	0.00	22.74	0.00	0.00	337.00	0.00	0.00	2.85	2.78	12.65	18.87	0.16
DQ209-8	02-26-15 01 209		3.06	0.00	0.00	6.49	22.80	0.00	0.00	32.20	124.39	0.00	1.57	0.00	0.00	15.00	6.16	1.90	0.12	0.00	0.00	34.36	0.44
DQ180-2	02-24-15 01 168		0.00	0.00	23.16	12.95	69.85	0.00	0.00	85.84	0.00	3.59	2.30	0.00	5.36	37.43	0.00	0.00	0.00	0.00	0.74	20.95	0.28
DQ177-1	02-25-15 01 179		0.00	0.00	0.00	14.99	17.50	385.73	0.00	19.89	0.00	0.00	0.00	0.00	0.00	6.51	3.60	0.00	0.00	0.00	0.26	7.98	0.53
DQ108-3	02-25-15 01 09		0.00	0.00	9.64	0.00	0.00	0.00	0.00	0.00	0.00	0.00	0.00	0.00	0.00	0.00	0.00	0.00	0.00	0.00	0.18	0.35	0.00
DQ108-3	02-25-15 01 10		0.00	0.00	9.66	0.00	0.00	0.00	0.00	0.00	0.00	0.00	0.00	0.00	0.00	0.71	0.00	0.00	0.00	0.00	0.18	1.43	0.00
DQ198-1	02-24-15 01 133	Py5a	0.00	61.23	8.85	0.00	0.00	311.23	0.00	5391.42	0.00	3.40	5.54	0.00	4.47	838.57	0.00	0.00	142.95	21.91	76.81	8.75	0.13

DQ97-1	02-24-15 01 58		0.00	48.54	111.25	0.00	0.00	42.74	0.00	1953.69	0.00	0.00	2.14	15.46	0.00	1047.93	0.00	0.00	0.00	757.34	762.19	0.00	0.00
DQ97-1	02-24-15 01 59		0.00	53.48	109.34	0.00	0.00	0.00	0.00	2045.64	0.00	0.00	4.68	0.00	0.00	1668.80	0.00	1.58	0.62	1188.36	837.22	0.00	0.00
DQ97-1	02-24-15 01 60		3.76	56.74	123.26	4.84	180.14	0.00	0.00	1454.35	0.00	36.28	25.40	0.00	0.00	1428.54	0.00	0.00	27.18	594.33	675.21	0.90	0.00
DQ97-2	02-24-15 01 61		4.90	61.28	211.76	0.00	0.00	0.00	0.00	3016.43	0.00	0.00	36.81	0.00	0.00	2837.51	0.00	0.00	0.56	2329.07	1101.69	0.29	0.00
DQ97-2	02-24-15 01 62		20.48	0.00	102.91	29.88	550.65	149.69	0.00	11745.30	0.00	74.13	177.45	0.00	6.91	10623.20	7.80	12.49	136.74	3474.98	3442.38	9.79	0.00
DQ97-4	02-24-15 01 170		0.00	61.63	64.36	0.00	0.00	0.00	336.92	15399.12	0.00	16.59	21.51	24.87	0.00	4056.47	5.39	0.00	18.58	3030.38	3285.38	0.00	0.00
DQ97-5	02-24-15 01 171		0.00	32.52	103.73	0.00	0.00	0.00	0.00	4338.05	0.00	0.00	3.48	0.00	0.00	1215.27	0.00	0.00	0.47	1356.48	1031.94	0.00	0.00
DQ33-1	02-24-15 01 173		6.53	80.00	91.60	0.00	0.00	608.73	276.78	12565.29	0.00	0.00	400.23	28.10	0.00	284.71	0.00	0.00	11.59	332.88	261.79	40.23	0.00
DQ33-3	02-24-15 01 174		3.76	126.88	109.21	0.00	0.00	428.23	0.00	11237.34	0.00	2.80	381.06	39.18	0.00	419.89	0.00	1.04	13.80	552.76	389.65	50.31	0.00
DQ-314	12-15-15 01 44		0.00	0.00	18.25	12.67	76.95	8.09	27.06	878.35	0.00	0.00	0.00	0.00	0.00	50.97	0.00	0.00	0.41	0.00	1.83	84.39	0.00
DQ-314	12-15-15 01 45		0.00	20.27	67.32	0.00	0.00	5.98	0.00	1108.86	0.00	0.00	18.78	0.00	0.00	350.75	0.00	20.70	0.35	16.90	28.26	84.71	0.00
DQ-314	12-15-15 01 46		0.00	134.08	246.43	0.00	0.00	11.02	43.77	10382.18	0.00	0.00	159.21	0.00	0.00	460.23	0.00	22.42	17.44	55.62	124.42	21.96	0.00
DQ-314	12-15-15 01 47		0.00	41.49	130.74	6.25	0.00	12.55	62.95	4317.92	0.00	0.00	76.24	0.00	4.39	650.45	0.00	32.90	12.23	37.26	101.54	86.18	0.00
DQ220-11	02-24-15 01 48		0.00	25.62	53.95	0.00	0.00	109.68	0.00	9248.21	0.00	0.00	0.85	0.00	0.00	156.52	0.00	0.65	0.00	272.39	2303.89	0.21	0.27
DQ93-1	02-24-15 01 70		0.00	0.00	39.48	0.00	0.00	0.00	0.00	12796.39	0.00	0.00	2.71	0.00	0.00	1459.95	0.00	0.00	22.88	2321.82	>5000	0.00	0.00
DQ93-1	02-24-15 01 71		0.00	0.00	84.02	0.00	0.00	0.00	0.00	7500.19	0.00	2.72	0.00	0.00	3.06	1243.69	0.00	0.00	0.50	1136.15	1465.94	0.00	0.00
DQ93-3	02-24-15 01 72		0.00	0.00	39.77	0.00	0.00	0.00	0.00	12710.91	0.00	3.25	0.00	0.00	0.00	2195.29	0.00	0.90	0.36	3161.39	3122.00	0.00	0.20
DQ224-4	02-24-15 01 88		0.00	121.30	80.74	0.00	48.79	657.34	0.00	17937.83	0.00	10.51	0.00	0.00	5.38	2732.28	8.57	0.00	62.26	1495.80	3884.53	0.87	0.00
DQ224-4	02-24-15 01 89	Py5b	0.00	0.00	75.63	0.00	0.00	0.00	0.00	11088.56	0.00	0.00	0.00	0.00	0.00	931.64	0.00	0.00	17.24	227.67	1388.40	0.23	0.00
DQ224-4	02-24-15 01 90		0.00	30.52	66.02	7.51	0.00	0.00	0.00	9469.23	0.00	0.00	1.90	0.00	0.00	1739.91	8.59	0.00	1.74	819.80	1134.07	0.00	0.00
DQ224-6	02-24-15 01 91		3.50	0.00	50.92	0.00	0.00	0.00	0.00	10613.82	0.00	0.00	0.93	0.00	0.00	7.20	0.00	1.69	0.20	108.14	1176.71	0.35	0.00
DQ224-6	02-24-15 01 92		0.00	40.32	79.48	0.00	0.00	0.00	0.00	38583.66	0.00	0.00	0.00	0.00	0.00	925.07	0.00	0.00	12.08	1118.62	>5000	0.00	0.00
DQ224-8	02-24-15 01 93		0.00	28.22	61.09	0.00	0.00	0.00	0.00	12304.51	0.00	0.00	0.00	0.00	0.00	1697.92	0.00	0.00	8.31	2527.07	>5000	0.22	0.00
DQ224-8	02-24-15 01 94		0.00	0.00	129.08	0.00	0.00	0.00	0.00	27422.73	0.00	0.00	0.00	0.00	0.00	13.99	3.96	0.00	0.00	211.37	331.98	0.00	0.00
DQ102-2	02-24-15 01 142		0.00	71.79	59.37	0.00	0.00	491.80	0.00	2903.22	0.00	0.00	0.00	0.00	0.00	1327.61	12.22	0.00	0.63	584.97	650.99	0.36	0.00

DQ102-3	02-24-15 01 143		0.00	29.77	140.24	0.00	0.00	0.00	0.00	3819.88	0.00	0.00	0.00	0.00	0.00	295.72	0.00	0.00	0.00	149.46	956.05	0.00	0.13
DQ228-6	02-24-15 01 54		9.38	0.00	270.36	47.27	212.61	1320.64	655.94	106.97	0.00	0.00	0.00	0.00	0.00	20.90	19.82	0.00	0.00	0.00	0.00	18.35	0.55
DQ228-8	02-24-15 01 56		11.55	0.00	73.92	95.71	486.70	170.60	0.00	149.30	0.00	0.00	0.75	0.00	0.00	61.04	5.88	1.39	0.23	0.00	0.00	57.92	0.00
DQ228-8	02-24-15 01 55	Py6	0.00	0.00	11.84	103.80	787.53	40.92	0.00	884.11	0.00	0.00	0.00	0.00	0.00	1.01	0.00	0.00	0.00	0.00	0.00	2.51	24.77
DQ228-6	02-24-15 01 53		0.00	0.00	15.74	382.49	601.43	0.00	0.00	17.43	0.00	0.00	0.00	0.00	0.00	0.00	0.00	0.00	0.00	0.00	0.00	0.21	13.31
DQ228-8	02-24-15 01 57		0.00	0.00	10.66	9.18	132.37	0.00	0.00	49.76	0.00	0.00	0.00	0.00	0.00	0.00	0.00	0.00	0.00	0.00	0.00	0.00	0.00
DQ200-3	02-25-15 01 30		0.00	0.00	0.00	0.00	30.78	0.00	0.00	30.09	0.00	0.00	0.00	0.00	0.00	12.00	4.51	23.35	0.00	0.00	1.03	5.98	0.00
DQ200-11	02-25-15 01 32		0.00	0.00	12.47	0.00	42.98	58.81	0.00	42.04	0.00	0.00	1.13	0.00	0.00	71.35	0.00	6.38	0.00	6.25	12.15	32.38	0.00
DQ185-5	02-24-15 01 81		0.00	0.00	7.84	0.00	14.61	62.06	0.00	52.23	0.00	0.00	0.00	0.00	0.00	121.33	0.00	0.00	0.00	0.00	6.71	41.28	0.26
DQ185-8	02-24-15 01 84		0.00	0.00	16.33	0.00	0.00	0.00	0.00	0.00	0.00	4.68	0.00	0.00	7.86	42.01	0.00	0.00	0.00	0.00	2.55	8.36	0.00
DQ191-7	02-25-15 01 19		0.00	0.00	6.84	80.99	658.67	0.00	0.00	0.00	0.00	0.00	0.00	0.00	0.00	0.00	0.00	0.00	0.00	0.00	0.92	51.02	0.00
DQ206-1	02-24-15 01 160		0.00	129.57	14.52	0.00	0.00	0.00	0.00	110.11	0.00	0.00	0.00	0.00	0.00	126.21	0.00	6.67	0.00	39.75	22.16	0.00	0.00
DQ194-6	02-25-15 01 27		4.10	0.00	0.00	0.00	0.00	0.00	0.00	0.00	0.00	0.00	0.00	0.00	0.00	0.00	0.00	9.47	0.00	6.69	5.62	0.00	0.00
DQ194-6	02-25-15 01 26		0.00	0.00	8.30	0.00	0.00	0.00	0.00	0.00	0.00	0.00	0.00	0.00	0.00	0.00	0.00	8.41	0.00	2.49	1.66	0.00	0.00
DQ194-3	02-25-15 01 21		0.00	0.00	7.07	0.00	0.00	0.00	0.00	67.68	0.00	0.00	0.00	0.00	0.00	0.46	3.16	1.74	0.00	4.08	4.88	0.00	0.00
DQ194-3	02-25-15 01 22	Mc1	5.96	0.00	19.97	0.00	0.00	0.00	0.00	223.36	0.00	0.00	0.00	0.00	3.23	4.87	0.00	131.84	0.00	27.51	14.85	0.00	0.00
DQ218-8	02-24-15 01 63		0.00	33.31	12.37	2.72	56.34	0.00	0.00	9.44	0.00	0.00	0.00	0.00	0.00	0.00	0.00	0.00	0.00	0.00	0.13	0.26	0.00
DQ218-8	02-24-15 01 64		0.00	50.63	11.98	4.20	115.30	0.00	0.00	11.69	0.00	0.00	0.00	0.00	2.80	0.00	0.00	3.93	0.22	0.00	0.00	9.50	0.00
DQ218-12	02-24-15 01 66		19.82	21.68	894.04	0.00	148.39	0.00	0.00	0.00	0.00	0.00	1.60	0.00	0.00	95.48	0.00	50.65	0.00	0.00	0.00	47.25	0.00
DQ218-13	02-24-15 01 67		22.03	0.00	70.78	6.66	379.01	45.85	0.00	0.00	0.00	0.00	0.00	15.91	0.00	1.23	0.00	10.82	0.00	0.00	0.00	1.46	0.00
DQ211-11	02-24-15 01 68		0.00	0.00	10.40	0.00	0.00	58.30	191.46	0.00	0.00	0.00	0.00	0.00	0.00	0.76	0.00	0.00	0.00	0.00	0.00	0.00	0.00
DQ211-11	02-24-15 01 69		0.00	20.49	9.12	0.00	0.00	0.00	0.00	0.00	0.00	0.00	0.00	0.00	0.00	0.00	5.03	0.00	0.20	0.00	0.11	0.00	0.00
DQ185-4	02-24-15 01 78		0.00	0.00	8.96	1.96	0.00	0.00	0.00	0.00	0.00	0.00	0.97	0.00	0.00	1.30	0.00	0.00	0.00	0.00	1.47	1.39	0.00
DQ185-4	02-24-15 01 79		0.00	0.00	8.99	0.00	0.00	0.00	0.00	16.99	0.00	0.00	0.00	0.00	0.00	19.87	0.00	0.00	0.00	0.00	1.70	6.62	0.00
DQ185-4	02-24-15 01 80		0.00	0.00	14.45	0.00	0.00	0.00	0.00	11.14	0.00	0.00	0.00	0.00	0.00	1.76	0.00	0.00	0.00	7.64	11.05	2.19	0.00

DQ219-5	02-24-15 01 85		0.00	0.00	11.90	2.63	0.00	0.00	0.00	0.00	0.00	0.00	0.00	0.00	0.00	10.65	0.00	3.89	0.00	0.00	0.18	0.31	0.00
DQ224-1	02-24-15 01 102		0.00	0.00	15.69	14.48	73.91	0.00	0.00	0.00	0.00	0.00	0.00	0.00	0.00	0.00	0.00	6.44	0.24	0.00	0.00	0.00	0.00
DQ212-2	02-24-15 01 103		5.45	19.05	20.87	0.00	33.99	0.00	0.00	16.44	0.00	0.00	0.00	0.00	0.00	74.69	0.00	3.35	0.00	0.00	0.40	2.95	0.00
DQ51-1	02-25-15 01 159		0.00	0.00	6.86	0.00	16.47	55.19	0.00	10.89	0.00	0.00	0.00	0.00	0.00	106.96	0.00	0.00	0.00	0.00	0.18	0.93	0.00
DQ82-1	02-24-15 01 176		0.00	0.00	33.56	2.98	10.97	0.00	0.00	97.59	0.00	0.00	0.00	0.00	0.00	78.73	0.00	0.00	0.00	0.00	10.11	59.58	0.00
DQ71-2-3	02-25-15 01 191		0.00	0.00	7.45	2.38	223.73	0.00	0.00	7.87	0.00	0.00	0.00	0.00	0.00	38.93	0.00	0.00	0.00	0.00	1.13	0.48	0.00
DQ70-1-1	02-25-15 01 198		0.00	0.00	0.00	0.00	25.36	0.00	0.00	0.00	0.00	0.00	0.00	0.00	0.00	0.00	0.00	4.83	0.00	0.00	0.74	0.40	0.00
DQ70-2-2	02-25-15 01 199		0.00	0.00	7.39	0.00	0.00	0.00	0.00	0.00	0.00	0.00	0.00	0.00	0.00	0.00	3.16	0.00	0.00	4.15	1.48	0.00	0.00
DQ107-2	02-25-15 01 03		0.00	0.00	0.00	0.00	23.65	0.00	0.00	71.38	0.00	0.00	0.00	0.00	0.00	38.28	0.00	0.00	0.00	0.00	0.00	13.86	0.10
DQ107-2	02-25-15 01 04		0.00	0.00	13.21	0.00	99.95	0.00	0.00	22.70	0.00	0.00	1.71	0.00	0.00	10.48	0.00	0.00	0.00	0.00	0.00	1.74	0.00
DQ107-1	02-24-15 01 163		0.00	0.00	0.00	0.00	0.00	0.00	0.00	0.00	0.00	2.36	0.00	0.00	0.00	0.00	6.60	0.00	0.18	0.00	0.18	0.00	0.00
DQ208-4	02-25-15 01 34		0.00	0.00	18.52	0.00	0.00	0.00	0.00	0.00	0.00	0.00	1.36	0.00	0.00	0.00	0.00	0.00	0.00	0.00	0.00	0.00	0.00
DQ208-4	02-25-15 01 35		8.51	0.00	20.10	0.00	0.00	0.00	0.00	11.82	0.00	0.00	2.38	0.00	0.00	29.92	0.00	0.00	0.00	0.00	0.13	0.00	0.00
DQ208-12	02-25-15 01 37		0.00	0.00	13.52	0.00	0.00	0.00	0.00	0.00	0.00	0.00	0.00	0.00	0.00	2.09	0.00	0.00	0.00	0.00	0.00	0.00	0.00
DQ208-12	02-25-15 01 38		0.00	0.00	11.11	0.00	0.00	0.00	0.00	0.00	0.00	0.00	4.91	0.00	0.00	0.00	0.00	0.00	0.00	0.00	0.00	0.00	0.00
DQ208-15	02-25-15 01 40		0.00	0.00	10.40	0.00	0.00	0.00	0.00	0.00	0.00	0.00	0.00	0.00	0.00	1.15	0.00	0.00	0.00	0.00	0.00	0.00	0.00
DQ209-15	02-24-15 01 44	Mc2	4.82	0.00	596.06	0.00	0.00	0.00	0.00	12.43	0.00	0.00	0.00	0.00	0.00	27.17	0.00	2.83	0.33	0.00	9.14	0.00	0.00
DQ208-5	02-25-15 01 205		0.00	0.00	6.54	0.00	0.00	0.00	0.00	0.00	0.00	0.00	11.40	0.00	0.00	281.32	6.16	105.36	0.39	213.72	167.30	0.32	0.00
DQ209-12	02-26-15 01 211		0.00	0.00	27.84	0.00	4.07	0.00	133.28	13.21	0.00	1.45	0.00	0.00	0.00	9.75	2.33	0.00	0.13	0.00	0.23	0.31	0.00
DQ220-1	02-24-15 01 47		4.93	37.74	22.96	0.00	123.50	0.00	0.00	0.00	0.00	0.00	0.00	0.00	0.00	33.04	0.00	2.22	0.00	0.00	0.00	150.01	0.00
DQ192-3	02-24-15 01 136		0.00	0.00	11.91	3.92	13.54	250.86	0.00	63.25	0.00	0.00	2.27	0.00	6.60	0.00	0.00	0.77	0.70	0.00	4.24	2.20	0.16
DQ192-3	02-24-15 01 137		0.00	0.00	22.26	16.98	222.14	0.00	0.00	91.43	0.00	0.00	0.00	0.00	4.14	98.26	0.00	0.00	0.38	7.65	2.47	12.18	0.00
DQ192-3	02-24-15 01 138		0.00	0.00	10.44	3.50	59.44	85.90	0.00	200.27	0.00	0.00	0.00	0.00	0.00	116.59	0.00	0.00	0.27	0.00	5.27	17.55	0.83
DQ164-12	02-24-15 01 77		0.00	0.00	6.64	1.49	81.59	0.00	0.00	110.38	0.00	0.00	1.04	0.00	0.00	10.70	0.00	0.88	1.33	0.00	0.91	16.68	0.59
DQ164-12	02-24-15 01 76		4.90	0.00	14.84	0.00	0.00	208.42	856.72	16.61	0.00	0.00	0.00	93.48	0.00	10.38	0.00	7.63	0.00	8.75	1.38	44.01	1.42

DQ194-4	02-25-15 01 23		0.00	0.00	6.21	5.69	103.84	0.00	0.00	0.00	0.00	0.00	0.00	0.00	0.00	8.02	3.78	0.00	0.00	0.00	0.00	1.45	0.21
DQ71-2-3	02-25-15 01 190		0.00	0.00	8.04	0.00	12.64	0.00	0.00	0.00	0.00	0.00	1.84	0.00	0.00	1.50	0.00	0.00	0.00	0.00	1.27	0.73	0.00
DQ70-2-2	02-25-15 01 200		0.00	41.63	12.30	0.00	17.54	146.02	0.00	0.00	0.00	0.00	0.00	0.00	0.00	1.33	0.00	1.01	0.00	2.50	7.10	1.05	0.00
DQ208-2	02-25-15 01 201		0.00	0.00	12.40	0.00	0.00	0.00	0.00	12.67	0.00	1.74	2.96	0.00	6.01	6.35	0.00	0.00	0.00	0.00	0.00	0.00	0.00
DQ208-2	02-25-15 01 202		0.00	0.00	13.79	2.06	0.00	0.00	251.02	106.02	0.00	0.00	1.86	0.00	0.00	321.97	0.00	0.00	0.20	9.69	14.29	0.00	0.00
DQ208-4	02-25-15 01 203		0.00	0.00	25.71	0.00	0.00	0.00	0.00	0.00	0.00	0.00	0.00	0.00	0.00	17.62	0.00	1.11	0.18	0.00	0.83	0.26	0.00
DQ51-1	02-25-15 01 158		0.00	0.00	9.74	11.44	114.82	0.00	0.00	20.06	0.00	0.00	0.00	0.00	0.00	29.61	0.00	0.00	0.18	0.00	2.70	5.08	0.00
DQ118-2	02-24-15 01 164		0.00	0.00	21.52	2.95	0.00	0.00	0.00	13.68	0.00	0.00	1.38	0.00	0.00	0.00	0.00	75.91	0.00	0.00	1.09	0.65	0.00
DQ118-2	02-24-15 01 165		0.00	45.19	52.69	0.00	6.50	187.44	0.00	29.82	0.00	2.60	0.00	0.00	2.84	0.63	4.61	80.20	0.00	7.93	2.09	0.00	0.52
DQ180-2	02-24-15 01 167		0.00	0.00	0.00	6.44	13.20	0.00	0.00	0.00	0.00	0.00	0.00	0.00	3.83	17.08	0.00	0.00	0.00	0.00	1.00	7.51	0.37
DQ201-2	02-24-15 01 140		44.43	0.00	718.10	0.00	21.47	0.00	0.00	28.69	0.00	0.00	1.28	0.00	0.00	170.47	0.00	7.81	0.00	0.00	0.00	7.78	0.00
DQ204-1	02-24-15 01 124		5.83	29.84	14.12	0.00	0.00	0.00	0.00	41.15	0.00	0.00	0.00	0.00	0.00	54.75	0.00	33.15	0.00	52.82	91.02	0.89	0.00
DQ78-1	02-24-15 01 135		0.00	29.77	11.23	0.00	45.72	0.00	0.00	16.79	0.00	0.00	1.21	19.83	0.00	19.13	0.00	0.00	0.00	0.00	5.45	2.77	0.00
DQ208-5	02-25-15 01 204		0.00	0.00	69.76	0.00	0.00	195.93	0.00	970.89	0.00	1.70	219.52	0.00	0.00	2007.55	0.00	80.24	5.54	414.10	588.70	18.51	0.00
DQ209-12	02-26-15 01 210		0.00	15.02	13.60	0.00	0.00	0.00	0.00	3435.29	0.00	0.00	21.50	0.00	2.65	735.33	0.00	0.00	12.30	138.43	264.97	8.53	0.00
DQ209-3	02-26-15 01 206		0.00	11.00	4.73	0.97	0.00	0.00	0.00	1054.40	0.00	0.00	34.12	0.00	1.65	864.75	0.00	5.64	4.26	222.87	226.13	8.66	0.00
DQ107-2	02-25-15 01 05		0.00	43.24	0.00	0.00	64.17	43.67	0.00	443.39	0.00	0.00	10.02	0.00	0.00	215.40	0.00	0.00	2.01	0.00	5.89	65.44	0.52
DQ194-4	02-25-15 01 25		0.00	0.00	0.00	0.00	0.00	106.60	0.00	1657.50	0.00	0.00	0.00	0.00	5.34	33.98	0.00	10.44	0.00	39.32	44.63	0.00	0.00
DQ191-7	02-25-15 01 20		0.00	35.10	0.00	8.69	0.00	0.00	519.39	1321.05	0.00	2.11	2.15	0.00	0.00	97.99	0.00	0.00	3.61	4.84	23.70	2.96	0.00
DQ209-3	02-26-15 01 207	Mc3	0.00	0.00	8.96	38.75	144.62	32.86	0.00	531.70	0.00	5.04	22.70	0.00	0.00	349.29	0.00	3.99	2.81	7.00	13.68	290.32	1.73
DQ194-4	02-25-15 01 24		16.71	0.00	161.14	0.00	9.81	0.00	0.00	19.43	0.00	0.00	0.00	0.00	0.00	7.03	0.00	1.29	0.22	0.00	0.48	4.99	0.00
DQ208-4	02-25-15 01 33		5.58	0.00	55.83	0.00	0.00	70.08	0.00	396.36	0.00	0.00	37.21	0.00	0.00	796.19	4.27	12.07	0.29	26.16	75.63	2.51	0.00
DQ208-12	02-25-15 01 36		0.00	0.00	0.00	0.00	0.00	0.00	0.00	47.49	0.00	0.00	8.36	0.00	0.00	60.03	0.00	1.63	0.00	14.11	13.90	1.34	0.00
DQ208-15	02-25-15 01 39		0.00	0.00	20.24	0.00	0.00	0.00	0.00	435.77	0.00	0.00	82.15	0.00	0.00	2224.44	0.00	78.07	6.53	619.04	801.54	40.77	0.13
DQ209-8	02-24-15 01 42		0.00	0.00	49.69	0.00	0.00	62.61	0.00	393.74	0.00	0.00	0.00	0.00	0.00	1143.20	0.00	44.99	0.00	50.36	127.65	2.00	0.00

DQ194-3	02-24-15 01 139		34.26	101.61	764.70	13.75	60.42	68.25	153.39	862.83	0.00	0.00	1.84	0.00	0.00	162.54	0.00	9.84	0.57	64.22	49.21	67.48	0.00
DQ82-1	02-24-15 01 175		4.84	29.85	11.45	0.00	0.00	0.00	0.00	356.09	0.00	4.62	0.00	0.00	0.00	51.84	4.40	1.24	0.00	0.00	3.10	20.41	0.00
DQ220-1	02-24-15 01 46		28.80	233.53	146.31	7.45	109.20	169.68	0.00	114.57	0.00	0.00	9.16	0.00	3.13	50.90	0.00	18.58	0.81	26.51	5.14	720.68	0.00
DQ220-11	02-24-15 01 49		0.00	0.00	66.65	0.00	0.00	37.57	0.00	699.19	0.00	0.00	0.00	0.00	3.27	3.18	0.00	1.85	0.00	40.75	780.30	0.00	0.00
DQ201-2	02-24-15 01 141		3.40	0.00	11.04	0.00	19.83	115.76	0.00	1850.29	0.00	2.13	0.00	0.00	4.83	16.44	0.00	27.70	0.00	222.32	120.64	0.35	0.00
DQ209-8	02-24-15 01 41		0.00	617.56	27.65	0.00	0.00	0.00	0.00	4769.34	0.00	0.00	4.22	0.00	0.00	1006.16	0.00	0.00	42.28	366.84	349.68	0.97	0.00
DQ209-15	02-24-15 01 43		0.00	0.00	17.95	0.00	20.59	0.00	293.98	3791.93	0.00	0.00	10.97	40.10	9.79	3990.11	9.17	7.37	43.12	1629.17	865.32	0.84	0.00
DQ206-1	02-24-15 01 161		69.31	50.23	37.73	0.00	17.77	0.00	0.00	134.88	0.00	3.76	2.02	0.00	4.85	181.87	0.00	8.88	0.43	182.75	388.36	22.42	0.00
DQ206-1	02-24-15 01 162		0.00	0.00	49.15	0.00	33.54	0.00	0.00	67.98	0.00	0.00	0.00	0.00	0.00	1206.43	0.00	0.00	0.00	21.23	335.59	69.21	0.00
DQ107-5	02-25-15 01 06		0.00	0.00	9.17	0.00	0.00	0.00	0.00	28.84	0.00	0.00	1.28	0.00	0.00	0.58	0.00	0.00	0.00	0.00	0.00	0.00	0.00
DQ107-5	02-25-15 01 07		0.00	0.00	17.01	0.00	0.00	42.28	0.00	95.87	0.00	0.00	2.75	0.00	0.00	0.65	0.00	0.00	0.00	0.00	0.00	0.00	0.00
DQ107-5	02-25-15 01 08		0.00	0.00	5.53	0.00	0.00	0.00	0.00	26.49	0.00	0.00	0.00	0.00	0.00	0.93	0.00	0.00	0.00	0.00	0.00	0.00	0.00
DQ110-3	02-25-15 01 01		0.00	0.00	0.00	0.00	0.00	0.00	0.00	0.00	0.00	0.00	0.00	0.00	0.00	0.00	0.00	0.00	0.00	0.00	0.00	0.00	0.00
DQ110-3	02-25-15 01 02		0.00	0.00	15.42	0.00	0.00	0.00	0.00	52.74	0.00	0.00	0.00	0.00	0.00	0.00	0.00	0.00	0.00	0.00	0.00	0.00	0.00
DQ189-1	02-24-15 01 125		0.00	0.00	0.00	0.00	0.00	55.24	0.00	0.00	0.00	0.00	0.00	0.00	0.00	0.00	0.00	0.72	0.00	0.00	0.64	0.00	0.00
DQ189-1	02-24-15 01 126	Mc4	0.00	0.00	0.00	2.27	0.00	0.00	0.00	0.00	0.00	0.00	0.00	0.00	0.00	0.55	0.00	3.71	0.00	0.00	9.49	0.00	0.00
DQ189-1	02-24-15 01 127		0.00	0.00	6.15	0.00	0.00	0.00	0.00	8.14	0.00	0.00	0.00	0.00	0.00	0.77	0.00	0.00	0.00	0.00	0.92	0.69	0.00
DQ189-2	02-24-15 01 128		0.00	0.00	11.99	0.00	0.00	0.00	0.00	84.45	0.00	0.00	0.00	0.00	0.00	0.52	0.00	0.00	0.00	0.00	0.23	0.00	0.00
DQ189-2	02-24-15 01 129		0.00	17.04	10.23	0.00	0.00	0.00	0.00	58.22	0.00	0.00	0.00	0.00	0.00	1.06	0.00	2.46	0.00	0.00	0.36	0.00	0.18
DQ78-1	02-24-15 01 134		0.00	0.00	9.69	0.00	0.00	0.00	0.00	14.74	0.00	0.00	0.00	0.00	0.00	0.00	5.31	0.00	0.00	0.00	0.50	0.00	0.00
DQ10-1	02-25-15 01 180		0.00	0.00	7.42	0.00	0.00	0.00	0.00	0.00	0.00	0.00	0.00	0.00	0.00	0.00	0.00	0.00	0.00	0.00	0.00	0.00	0.00

1919